PETROLEUM RESEARCH JOURNAL

TECHNICAL PAPERS

EXPLORATION

A Qualitative Structural Evaluation of Jaba Az Zalmah Area, Al-Kufrah Basin: Integration of Structural and Aeromagnatic Mapping .....
Amin A. Sherif 1

Late Cretaceous Stratigraphy and Palaegeography of Zaltan Platform (Concession 59), South Central Sirt Basin, Libya .....
Miloud M. Abougares and Mahmud. T. El-Bakai 23

Petrography of the Uppermost Bahi Formation in the West Az Zahrah (B) Field, Az Zahrah – Al Hufrah Platform, NW Sirt Basin, Libya .....
Muftah Ahmid 33

Controls on Porosity and Permeability of the Lower Cretaceous Nubian Formation Reservoir, Abu Attiffel Oil Field, Eastern Sirt Basin, Libya .....
Milad M. Ben Rahuma 49

Three New Ostracode Species of Buntonia and Protobuntonia from the Upper Cretaceous of Iraq .....
Jenan M. Taha Al-Bashir 57

CHEMISTRY

FTIR Infra-red Observations of the Adsorption of Ethene, Ethyne and Carbon Monoxide on Supported Platinum Catalysts .....
Ezziddin A. Arafa 65

Evaluation Study for a number of Libyan Crude Oils and its Products by Using Chemical Composition (^{13}C n.m.r. Spectroscopy Technique) and some Physical Properties .....
M.A. Abdulaziz and Abeer Abdul Kader 73

VOLUME 15 – (2003)

Petroleum Research Centre
P.O.Box 6431, Tripoli
Great Socialist People's Libyan Arab Jamahiriya

Petroleum Res. J. Vol. 15 (2003): P. 1–22, 19 Figs.

A Qualitative Structural Evaluation of Jabal Az Zalmah Area, Al-Kufrah Basin: Integration of Structural and Aeromagnetic Mapping

Amin A. Sherif*

التقييم النوعي للتراكيب الجيولوجية لجبل الظلمة، حوض الكفرة: التكامل بين التخريط التركيبي والمغناطيسي

الأمين عبد الله الشريف

من خلال الدراسة الحقلية و تحليل الصور الجوية للمنطقة الشمالية–الشرقية من حوض الكفرة في جنوب شرقي ليبيا، تم تجميع خريطة تكتونية وإعداد دراسة تحليلية لحركية مجموعة من التراكيب المتوازية الأضلاع. أظهرت هذه الدراسات فئات الصدوع الرئيسية التالية:

صدوع انزلاق – مضرب يمينية ذات اتجاه شمالي – غربي.

صدوع انزلاق – مضرب يسارية ذات اتجاه شمالي شرقي.

صدوع شرق– غرب كفئة فرعية من الفئتين السابقتين.

أما الصدوع الواقعة في إتجاه شمال–جنوب فهي في الأساس صدوع عادية ممثلة بفئة مخسفات واضحة المعالم في نظام تدريجي يميني. هذه الفئات من الصدوع أظهرت نظام انحراف يساري في اتجاه شمال شرق، وبعرض 30 كم، مكون من أربع نطاقات متساوية تقريباً في العرض، كل نطاق منها يحصر أو يتحكم في توزيع الصدوع الشمالية–الغربية. المنخسفات الشمالية–الجنوبية، ذات ترسبات من العصر الأوردفيشي العلوي، تحدد بداية نظام الانحراف عند العصر الكمبري الأخير أو الأوردوفيشي الأول، لأن هذه المنخسفات توقف أو تحصر أو تتحكم في إنتشار جميع فئات الصدوع في المنطقة.

إن صخور القاعدة التي تم دراسة هيئتها من خلال خريطة مغناطيسية جوية، أكدت تواجد نظام الإنحراف، حيث أن وسط نظام الانحراف المقترح، كما يظهر على السطح، يتوافق مع وادي سحيق في إتجاه شمال–شرق على الخريطة المغناطيسية. كما تم دراسة مجموعة من الشاذات المغناطيسية مقابل النموذج الحركي للمنطقة، وتبين أن هذه الشاذات تتوافق مع نظام الإنحراف المقترح، وذلك من خلال تراكيب متكشفة على السطح.

Abstract: *The compilation of a fault map from field work and photo interpretation for part of the north-eastern flank of Al Kufrah Basin in south-east Libya, together with the kinematic analyses of several rhomboid structures, showed the following major fault sets: dextral NW strike-slip faults; sinistral NE strike-slip faults; and EW faults as subsidiary sets of either the NW or NE trends. The NS trend, mainly as normal faults, is represented by a north-south, right-stepping set of well-defined en echelon grabens. These fault sets revealed a NE sinistral wrench system, about 30 km-wide, made up of four belts of almost equal width, each delimiting or controlling the distribution of the NW faults. The NS grabens, which are filled with Upper Ordovician sediments,*

* Department of Geology, Faculty of Science, Al Fatah University, Tripoli-Libya.

mark the initiation of the wrench system as early as Late Cambrian or Early Ordovician, because they control, restrict, or confine the distribution of all the other fault sets in the area.

The basement configuration as interpreted from a total intensity aeromagnetic map for the area confirmed the existence of this wrench system, where the median of the proposed wrench system at the surface coincides with a NE-trending deep valley on the magnetic map. Several magnetic anomalies were tested against the kinematic model for the area and were found to comply with the proposed wrench system, with identical structural manifestations on the surface.

INTRODUCTION

A preliminary geological map is presented here as part of the geological mapping project for Jabal Al Qardabah Sheet (Fig. 1), one of the mapping projects carried out by the Industrial Research Centre (IRC). It is part of Jabal Az Zalmah area, on the north-eastern flanks of Al Kufrah Basin, SE Libya. The geologic map (Fig. 2) represents an area of about 5000 Km^2, and comprises eight 15-minute sheets.

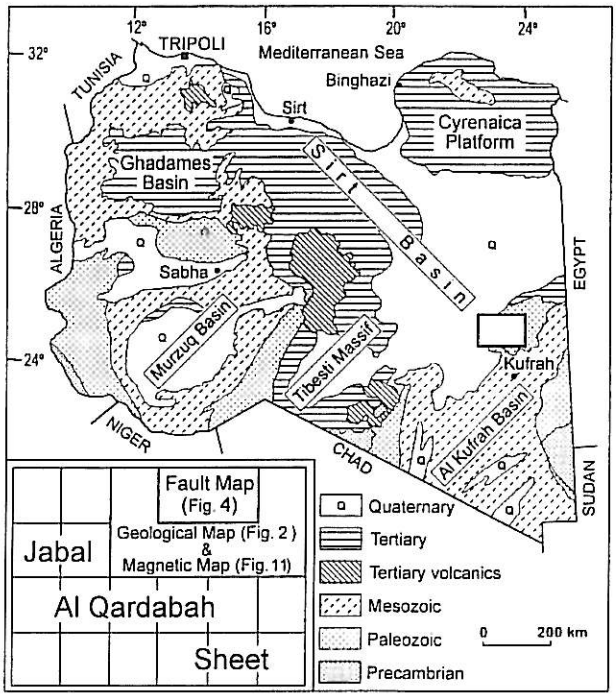


Fig. 1. Index map to the geology of Libya showing the location of Jabal Al Qardabah Sheet on the NE flanks of Al Kufrah Basin. Inset shows the location of the geological map (Fig. 2) fault map (Fig. 4) and magnetic map (Fig.. 11) with respect to Jabal Al Qardabah Sheet.

Structural photo interpretation was carried out using eight strips of stereo-pairs having 60% overlap and 30% sidelap at a scale of 1: 40,000. Each 15-minute sheet is covered by three to four north-south-running strips of aerial photographs, seven to ten overlapping photos per strip. A fault map for two of these sheets (Fig. 4) was compiled from the interpretation of aerial photographs and fieldwork. Both of these maps will be studied in relation to each other to investigate any association between the distribution of the stratigraphic units and the tectonic setting of the area.

A third map, a residual total intensity aeromagnetic map (Fig. 11), will be qualitatively analysed, and later interpreted in terms of the structural and stratigraphic observations derived from the fault map and the geological map, respectively. The magnetic map covers exactly the same area as that covered by the geological map (see Fig. 1). This should help in making a three-dimensional correlation between the surface geology and the basement "topography". Based on such correlation, a tectonic model for the study area will be proposed.

STRATIGRAPHY

The author was directly involved in the mapping of Jabal Al Qardabah Sheet through the structural analyses of the area, while Mr. Yousif A. Shagroni of the Industrial Research Centre established the stratigraphy for the area. The participation of the present author in the capacity described allowed access to the stratigraphy of the area. A synopsis of the stratigraphy is presented here as personal communication from Mr. Shagrouni (Fig. 3).

The north-eastern outcrops (Az Zalmah area) of Al Kufrah Basin is represented mainly by Palaeozoic and Cretaceous rocks. The Cretaceous rocks are not shown on figure 2 because of their restricted outcrops and the scale limitations of the map. The whole sequence is made up of clastic rocks (Fig. 3). Unlike the south-eastern and south-western outcrops of Al Kufrah Basin, this poriotn of the basin is almost barren of any igneous or metamorphic exposires, save for a basaltic ring structure within the central west of Jabal Al Qardabah Sheet, at 25°37'00" N, 22°47'00" E (beyond the western limits of figure 2).

Within the area of figure 2, the Lower Palaeozoic sequenes (Cambrian to Lower Devonian) almost follows the same lithostratigraphic subdivisions found in Murzuq Basin. The deviations are: 1) the missing of Hawaz Formation (Middle Ordovician), and 2) the

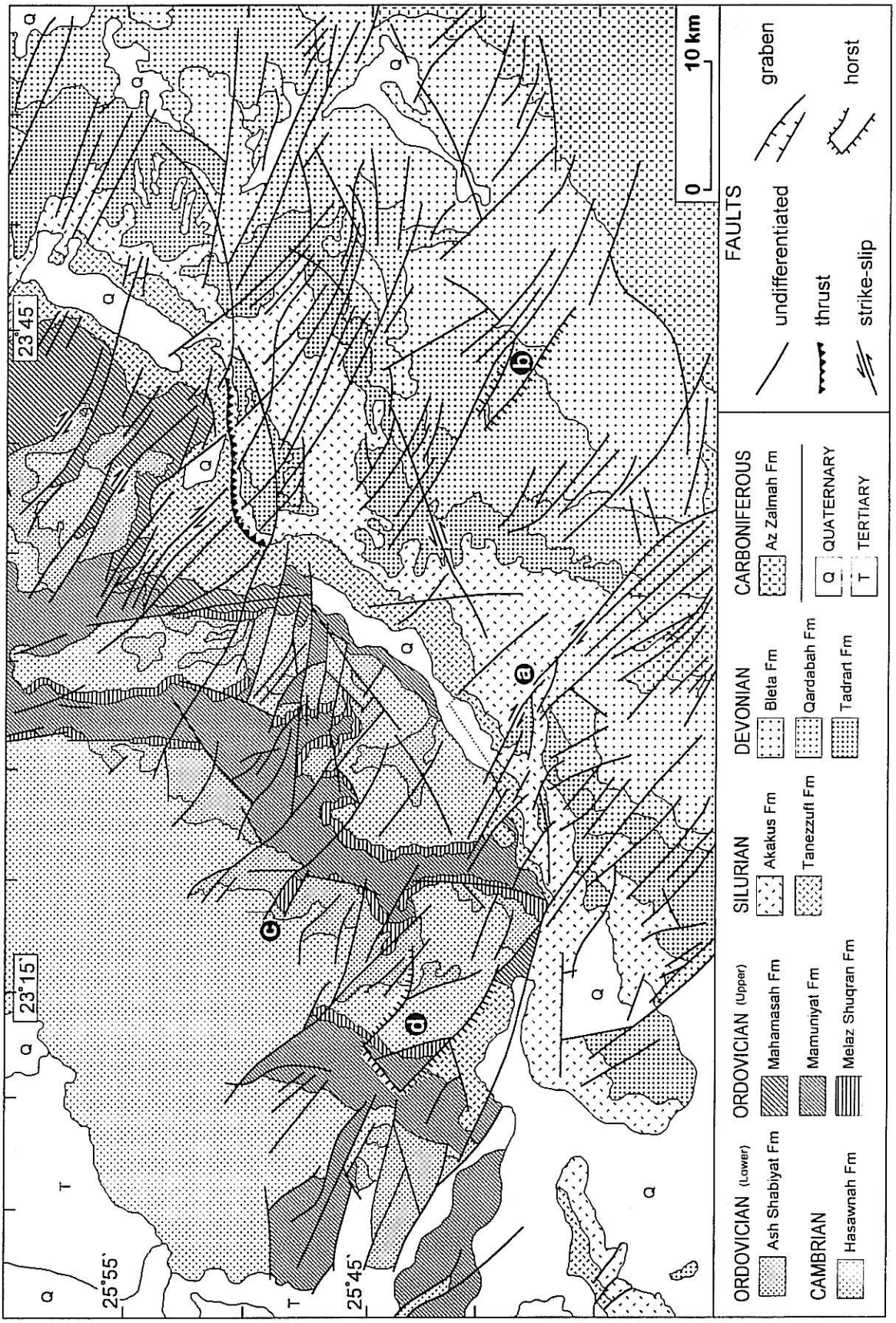


Fig. 2. Geological map for part of Jabal Al Qardabah Sheet (Yousif A. Shagroni, personal comunication). The magnetic map (Fig. 11) covers the same area to facilitate correlation between surface geology and basement (see index map Fig. 1). Circled labels a-d refer to structures on Fig. 8.

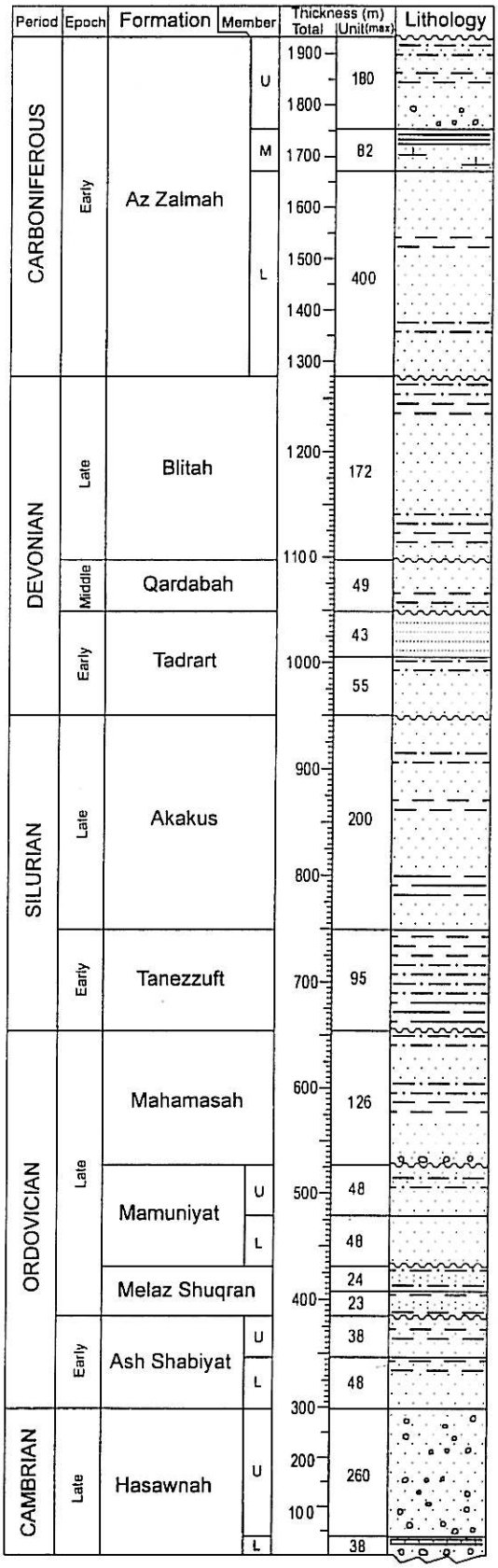


Fig. 3. Stratigraphy of Az Zalmah area (Yousif A. Shagroni, personal comunication). Thickness for individual units represent maximum of composite sections. Note variation of thickness scale.

addition of Mahamasah Formation (Upper Ordovician).

For the Upper Palaeozoic (Middle Devonian to Carboniferous), Al Kufrah Basin was separated from Murzuq Basin by the Tibesti-Sirt Uplift beginning in Middle Devonian, or post Tadrart Formation (Klitzsch, 1966, Bellini and Massa, 1980). This isolation created a different style of deposition unique to Al Kufrah Basin, which has a lithology different from that found in Murzuq Basin.

Cambrian

Hasawnah Formation (Late Cambrian)

Lower Member (38 meters): Made up of several fining-upward cycles. The lower part is generally coarse- to medium-grained sandstone, well rounded and cross-bedded, conglomeratic at lowermost levels (base is not exposed in the area). The cycles in the middle part start with thickly-bedded, coarse-grained sandstone, and terminate with thinly-bedded, fine- to medium-grained sandstone with intercalations of silt and very fine-grained sandstone. The upper part is represented by four fining-upward cycles that grade from coarse-to medium- to fine-grained sandstone, and terminate with micaceous shale interbeds.

Upper Member (260 meters): Represented by fining- and thinning-upward cycles of coarse- to medium-grained, cross-bedded sandstones. The cycles within the lower part of this member are mostly conglomeratic at their lower levels, becoming lenses of imbricated conglomerate upwards, while these same cycles are terminated by ferruginous, very fine-grained sandstone and siltstone. The uppermost 15 meters of the lower part are rich in *Arthrophycus* and *Crusiana*. The cycles within the upper part are sharp-based and terminate with medium- to fine-grained sandstone. The uppermost 40 meters of the Upper Member are rich in *Tigillites*.

Ordovician

Ash Shabiyat Formation (Early Ordovician)

Lower Member (10-48 meters): Fining- and thinning-upward cycles of coarse- to medium-grained, *Tigillite*-bearing, kaolinitic sandstone. At different levels, this lithology is sometimes intercalated with cross-bedded sandstone. The cycles are often terminated by about 20 cm of bluish-green clay.

Upper Member (38 meters): Fine-grained, thinly-bedded sandstone containing *Arthrophycus*, with silt intercalations occasionally alternating with interbeds of fine- to medium-grained, cross-bedded sandstone.

Melaz Shuqran Formation (Late Ordovician)

Lower Part (23 meters): Olive-green claystone, gypsiferous in the lower 6 meters, intercalated in intervals by fine-grained sandstone and micaceous siltstone, as laminated and/or rippled bedding or as flakes.

Upper Part (0-24 meters): Very fine-grained sandstone and siltstone, in the form of rippled bedding, with intercalations of claystone.

Mamuniyat Formation (Late Ordovician)

Lower Member (48 meters): Sandstones with a wide spectrum of grain size ranging from fine to medium to cobble, as well as varying textures from immature to mature within a very close distance, sometimes as few as tens of meters. Bedding thickness is also in the range of 0.4 to 2 meters. Furthermore, primary sedimentary structures within individual beds are extremely deformed: laminated beds are highly convoluted; cross-bedded sets develop overturned structures; and slump-like structure, as well as massive and poorly defined internal structures are observed.

Upper Member (48 meters): In contrast with the lower Member, the upper Member is thinly to medium, evenly bedded, mostly micaceous, well sorted, medium to coarse-grained sandstone. As for the sedimentary structures, the Upper Member has horizontal or gently dipping lamina and/or rippled bedding. Furthermore, the upper part is found to be intercalated with micaceous, silty, very fine-grained sandstone containing few poorly preserved moulds of brachiopods.

Mahamasah Formation (Late Ordovician)

Made up of coarsening-upward cycles–either thinning-upward or thickening-upward–distributed among four levels. Each of these levels seem to be deposited in a distinctive structurally controlled setting.

Level 1 (36 meters): The oldest level, made up of four coarsening-upward, thinning-upward cycles, each starting with claystone, followed by fine- to medium- to coarse-grained sandstone, and ending with medium- to coarse-grained, conglomeratic sandstone.

Level 2 (5.5-12.5 meters): Made up of three coarsening-upward, thinning-upward cycles of claystone, followed by fine- to medium-grained, or fine-grained, subangular sandstone..

Level 3 (50 meters): Represented by one coarsening-upward cycle. This level has two distinctive thickening-upward cycles with an intervening thinning-upward cycle. From bottom, it is made up of: claystone; intercalations of clay, silt, and fine-grained sandstone; fine- to medium-grained sandstone; and fine- to medium-grained, subangular sandstone that starts with cross-bedding and ends with lamination.

Level 4 (22 meters): The youngest level, with two coarsening-upward, thinning-upward cycles. In sequence, these cycles are represented by: claystone; siltstone; fine-grained sandstone; fine- to medium-grained sandstone; and medium- to coarse-grained sandstone.

Silurian

Tanezzuft Formation (Early Silurian)

Mostly represented by coarsening-upward cycles of variable thickness, with an overall thickness ranging between 20 and 95 meters (more than ten cycles at maximum thickness). These cycles start with argillites having variable shades of blue and green, and terminates with cross-rippled, micaceous siltstone. They range in thickness between 1.5 and 5.5 meters, with no preferential thickness trend. Within the last few meters of Tanezzuft Formation, the cycles become fining-upward, mostly made up of brownish green gypsiferous argillites, with flakes and very thin lenticular beds of siltstone. It is worth mentioning that the older levels of this unit are found to fill, progressively, the deepest palaeosites.

Akakus Formation (Late Silurian)

Represented by more than 30 coarsening-upward cycles, ranging in thickness between 1.5 and 10.5 meters, while the recorded thickness for the whole

unit is between 80 and 200 meters. The lower ½ of the formation is mostly made up of argillites, followed by silt, and ending with fine- to very fine-grained, cross-laminated and micaceous sandstone. The cycles within the upper ½ of the formation are mostly terminated by large lenses (more than 30 meters long) of thinly to medium-bedded and flaced, fine-grained sandstone. Among the sedimentary structures found within the upper half of Akakus Formation: convoluted bedding, wrinkled ripples, mud cracks, wavy bedding, and double-crested ripples. The upper ¾ of Akakus Formation become progressively rich in trace fossils: *Crusiana*, *Arthrophycus*, and *Tigillites*.

Within the study area, the Devonian is represented by Tadrart Formation, Qardabah Formation, and Blitah Formation (Fig. 3). The Qardabah Formation is a new unit introduced here, having no equivalent in Murzuq Basin, nor has it been identified in Al Kufrah Basin. These three formations represent different depositional systems, separated by clear and sharp erosional surfaces.

Devonian

Tadrart Formation (Early Devonian)

Lower Part (28-55 meters): Coarsening-upward, fining-upward cycles of fine- to medium-grained, subangular, cross-bedded sandstone, with interlevels of fine-grained, micaceous, cross-bedded sandstone. This lithology is found to be interfingering–within the upper half of this interval–with fine-grained sandstone and siltstone, having clay intercalations and containing *Arthrophycus*.

Upper Part (0-43 meters): Sandstone: fine- to medium-grained, subangular, cross-bedded or laminated, Tigillite-bearing. This interval represents one thinning-upward sequence.

The maximum recorded thickness for Tadrart Formation was 83 meters.

Qardabah Formation (Middle Devonian)

The main constituency of this formation is either cross-bedded sandstone or *Tigillite*-bearing sandstone, the latter being more dominant. The texture for these sandstones is coarse- to very coarse-grained within the lower and upper levels of this formation, while it is fine- to medium-grained in the middle levels, with a well rounded texture throughout the sequence. The cross-bedded sandstones sometimes start with conglomerates, while in others they terminate with lamination sets. On the other hand, the fine- to medium-grained sandstones sometimes terminate with siltstones and claystones. The uppermost levels of this formation contain *Zoophycus*. The recorded thickness for Qardabah Formation is between 38 and 49 meters.

Blitah Formation (Late Devonian)

Generally representing coarsening- and thickening-upward cycles. Each cycle starts with claystone, followed by claystone with intercalations of lenticular siltstone and very fine-grained micaceous sandstone, and terminating with fine- to very fine-grained sandstone with clay parting. The sandstones of some of these cycles are cross-bedded, while some other cycles bare mud cracks at their topmost levels. The base of this formation starts everywhere with light bluish-green muds, while it is terminated by bluish-green claystones found as intercalations and/or lenticulations with very fine-grained sandstone. The formation is abound with *Zoophycus*, with minor *Tigillites* and *Chondrites*, while *Brachiopod* moulds are found at the topmost levels. The recorded thickness for Blitah Formation is between 163 and 172 meters.

Carboniferous

Az Zalmah Formation (Early Carboniferous)

Lower Member (400 meters): Fine- to medium- to coarse-grained sandstone. Often as cross-bedded and in fining-upward cycles. At different levels the fine sandstones are intercalated with siltstone and claystone. Rootlets and *Lepidodendrons* are also found at different levels, mostly associated with mud cracks. *Zoophycus* and *Tigillites* are the main trace fossils.

Middle Member (82 meters): Mostly very fine-grained sandstone as lenticular bedding. Burrows and rootlets are found as intervals at different levels, as well as intervals of argillites and claystone. Upper part has intercalations of siltstones, argillites, and shale. Topmost levels are represented by fine- to medium- to coarse-grained sandstone with shale intercalations.

Upper Member (180 meters): Sandstones with grain size ranging between very fine to very coarse,

being microconglomeratic at lower most levels. Lower part found as cross-bedded, while the middle part is calcareous or micaceous. The upper part is found as fining- or coarsening-upward cycles, the latter being more dominant. Throughout this part, the fine- to very fine-grained levels of either of these cycles is most often associated with clays as flakes, partings, or intercalations.

STRUCTURAL FRAMEWORK

Two 15-minute sheets, bounded by longitudes 23°15'00"-23°45'00" E and latitudes 25°45'00"-26°00'00"N were selected for structural interpretation. This area was found to include most of the Palaeozoic sequence, from Cambrian in the north-west to Devonian in the south-east (Fig.2).

The structural interpretation involved folds, faults and joints, but emphasis was on all linear or semi-linear structural features of any length, that appear to represent faults or joints. These fractures were either explicit or inferred from features such as a break in topography or an offset in drainage, a change in tone, or from the alignment of hills along a semi-linear trend.

Throughout the area covering Jabal Al Qardabah Sheet, most of the fault planes which were visited in the field show a very clear horizontal component of displacement, as expressed by either horizontal grooves or slickensides. These strike-slip faults are also very clearly seen on topographic planes, with offsets ranging between few meters to tens of meters. Strike-slip faults were most often found in *en echelon* sets having either NW or NE orientation, while NS and EW faults were most often confined within well defined, fault-bounded structures. In the field, NS and EW faults generally show negligible vertical displacement, much less horizontal displacement, despite the fact that these fault sets represent very long fault lines or lineaments, sometimes exceeding 20km.

The data gathered from the structural photo-interpretation and supported by field checks was transferred onto controlled mosaics at a scale of 1:50,000, thus resulting in a controlled *fault map* (Fig. 4, see Fig. 1 for location). The fault map was then filtered manually through a template to obtain separate *trend maps* for every major trend, namely, NS, EW, NE, and NW (Fig. 6). The devised template (centre of figure 6) allowed the picking of any fault within a specified azimuth range for any particular

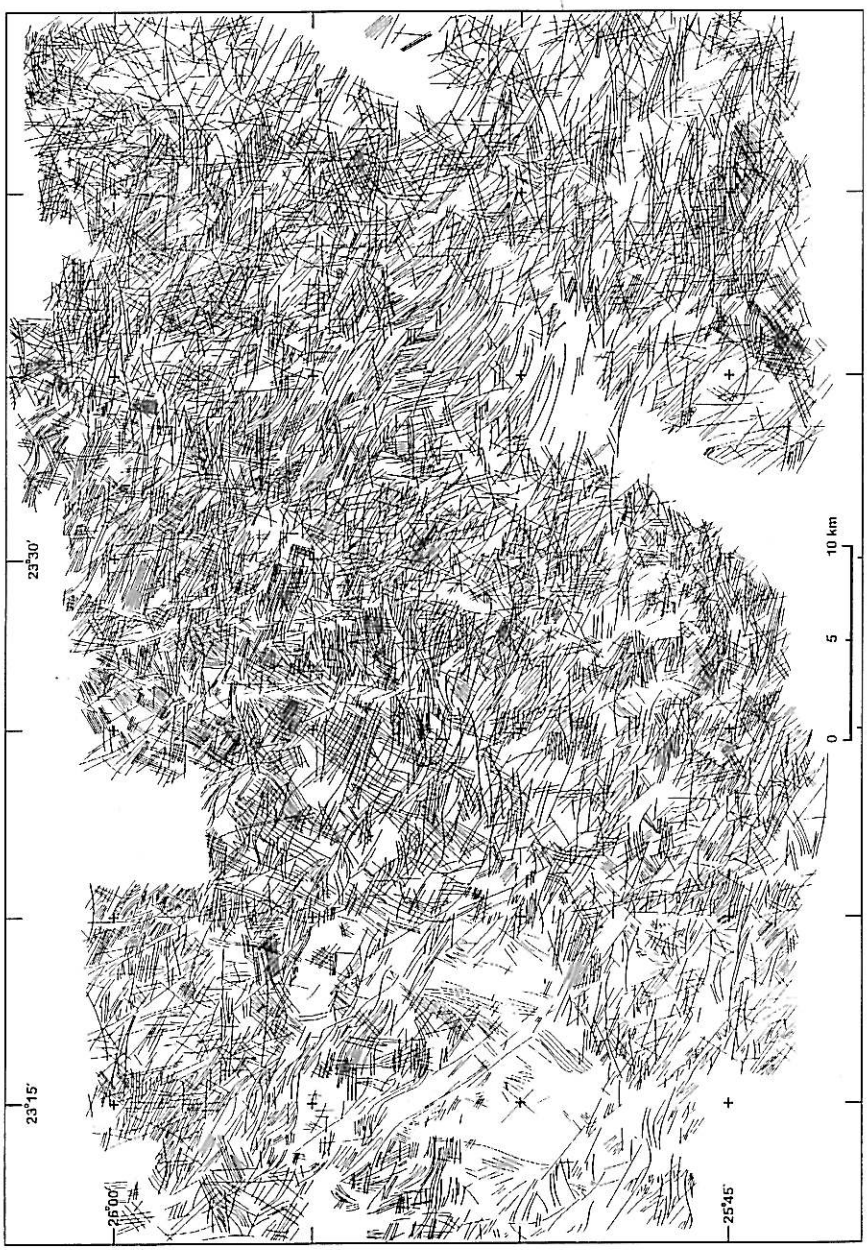


Fig. 4. Fault map of part of Jabal Al Qardabah Sheet, NE Al Kufrah Basin, compiled from photinterpretation of stereoscopic aerial photographs. See Fig. 1 for location.

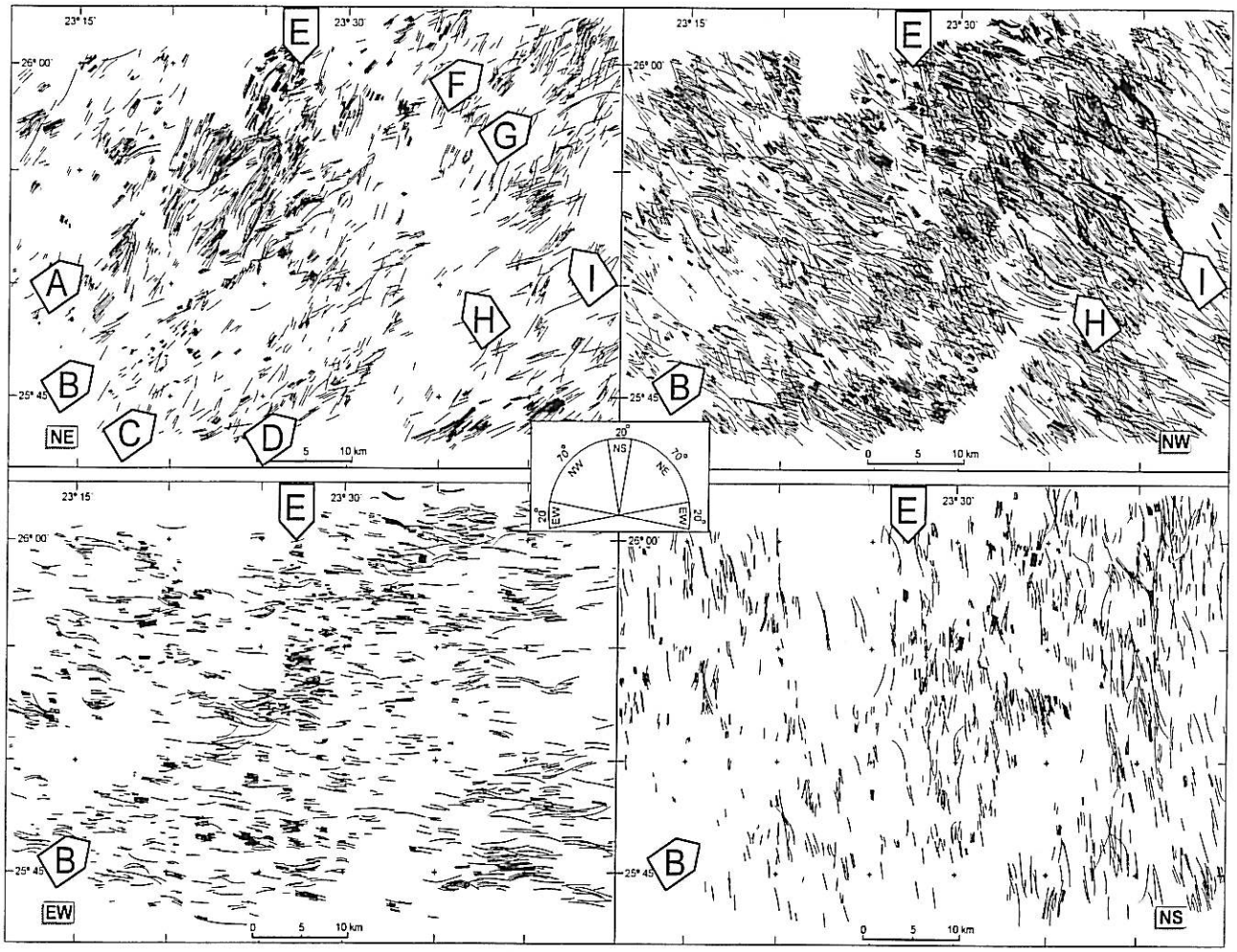


Fig. 5. Major trend maps filtered from fault map (Fig. 4) through the template shown in centre. Labels A to I represent major fault sets (see text for description).

trend. Thus, the NS and EW trends were both given an azimuth range of 20°, while the NW and NE trends were given a 70° azimuth range. The NW and NE trends, having a wide angle range, were further separated into NNW, WNW, and NNE, ENE, respectively (Fig. 6).

The majority of faults in the area are not clear straight faults, rather they are curved or bent. For that the manual approach for filtering the eight trend maps (Figs. 5 and 6) was favoured because it allowed, for example, the picking of a bent northwest-trending fault to be included in both the NW and NS trend maps. Similarly, and for the same fault, it could also be included in both the NNW and WNW trend maps.

Fault Sets

Several fault sets can be traced at once on all eight trend maps of figures 5 and 6. These are either found as linear fault sets or as clusters of faults. The description of these fault sets follows.

Fault Sets A, B, C, and D

All four of these sets are NE linear sets, therefore they are all explicitly seen on the NE trend map in figure 5 and on the ENE trend map in figure 6. However, the NNE trend, and while it is a subset of the NE trend, shows no trace of these fault sets, except for *fault set A* where it is manifested as a separator between the two main clusters of faults seen on the NNE trend on figure 6. This indicates that all four of these fault sets belong to the ENE trend.

While *fault set B* is barely seen on the NNE trend map, its manifestation and control on all the other trend maps, without exception, is very conspicuous. In all of these maps, the fault population is much higher east of *fault set B*. This is particularly seen

on the EW trend map (Fig. 5) and the NNW trend map (Fig. 6), where the faults stop abruptly along the trace of *fault set B* and to the east of it. This same effect is also found on the NW and WNW trend maps, even though these two trends have the highest and evenly distributed fault population in the area.

With its impact on all the trends in the area, *fault set B* is not just made up of a single throughgoing set of faults, rather it is made up of conjugate sets of faults (see NE trend, Fig. 5). This feature is not found along the other fault sets described so for, which suggests that *fault set B* could represent the median of a wide fault zone (about 30 km wide) encompassing all the NE fault sets described above.

Fault Set E

The control of this north-south fault set is also seen in all the trend maps, yet it is only partially seen on the NS trend map (Fig. 5). The EW trend map shows a cluster of east-west faults confined within a narrow zone running north-south and in the path of *fault set E* (Fig. 5). A direct comparison between the EW and NS trend maps reveals that *fault set E* is not just one fault set but in fact it is made up of two NS parallel fault sets, with an intervening distance of about 4 km. Therefore, the confinement of EW faults is directly related to *fault set E*, which makes the latter more like a graben defined by two NS fault sets.

The effect of *fault set E* is also seen on the NW trend map, where the anomalous fault population of this trend is almost non-existent within this fault set. This is also observed on the subsidiary trend map WNW. The effect of this fault set on the NE trend map is however represented by the sundering of the two NNE clusters of faults.

Among the fault sets discussed so far, it was shown that the NE *fault set B* and the NS *fault set E* both have controlled the distribution of all the other trends in the area (compare with fault map, Fig. 4).

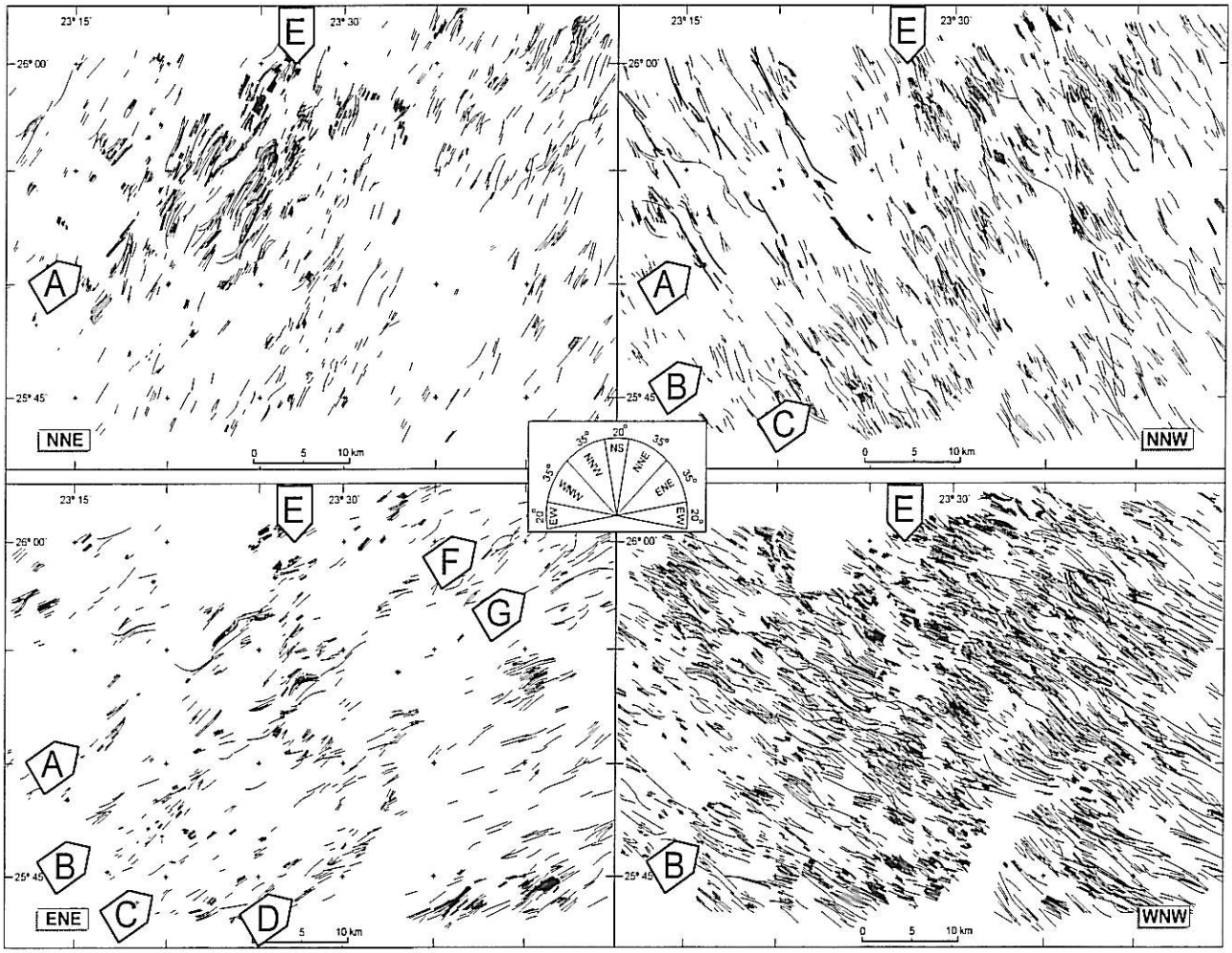


Fig. 6. Subset trend maps filtered from NW and NE trend maps (Fig. 5) through the template shown in centre.

The fault population in most of the trend maps is higher east of *fault set E*, as was described for the *fault set B*. This control indicates that both of these fault sets are among the first structural trends to have developed and should help in explaining the structural framework of the area.

Fault Sets F and G

These two northeast-trending fault sets are very important because they enclose between them a very peculiar cluster of curved faults displaying a crude "S" shape which have the same NE trend (Fig. 5). Both of these fault sets are not visible on the NNE trend map of fig. 6 because they belong to the ENE trend, therefore they would belong structurally to *fault sets* A to D.

Fault Sets H and I

These two northwest-trending fault sets define the limits of a large sigmoidal structure (highlighted on NW trend map, Fig. 5), which does not show on both the NNW and WNW trend maps. This indicates that it was formed from the combination of both of these two trends, where the smaller lozenge structures within the large sigmoidal structure are defined by two NNW and two WNW faults. The controlling effect of fault sets H and I is very prominent over the northeast fault sets, where *fault set H* is found to limit the continuation of fault sets A to D northeastward, while *fault set I* prevents fault sets F and G from extending southwestward (see NE trend, Fig. 5).

Structural Trends

Further enhancement of these fault sets was achieved by producing 22 more trend maps through permutational coupling of the original eight trend maps of figures 5 and 6, which brought the total number of trend maps to 30. These new maps emphasised the fault sets of figures 5 and 6 by bringing out new clusters of faults directly related to these fault sets.

The combination NE+NNW (Fig. 7 a) is presented here as an example. The intervening space between any two adjacent fault sets A to D shows distinctive fault patterns. These spaces are shown on figure 7 b as Belts 1 to 4, with the *NE Line* (or *fault set B*) as the median of these belts. Belt 1 and Belt 2 are represented by long and widely spaced NNW faults (highlighted on Figure 6, NNW trend) that either terminate or offset across *fault set A*. These same belts are also accentuated by the two NNE clusters of faults. Fault sets B and C mark the boundaries of Belt 3, where the NNW trend has closely spaced faults with their lengths defining the width of this belt. While Belt 4 has the least distinctive pattern of faults, the scattered orientation of the faults in this belt gives a contrast against Belt 3, which further help define the limits of both belts. All four of these belts stop abruptly at *fault set H* (Line 1, Fig. 7 b).

Graben1 and Graben 2 (*fault set E*) represent a north-south, right-stepping *en echelon* set of grabens (stippled on Fig. 7 c) with the southern segment extending farther south beyond the area of figure 7 a. As was discussed earlier, this *en echelon* set was found to affect most of the structures described thus far.

Kinematic Settings

The four belts are believed to represent the width of a northeast-trending wrench system –about 30 km wide– with the *NE line* as the median of this system (Fig. 7, b) especially that most of the faults in the area are strike-slip faults having fault planes with clear horizontal grooves or slickensides.

A structural system of this nature and width must cover a much larger area than is defined by the limits of Jabal Al Qardabah Sheet. According to Aydin and Nur (1982), the length of a strike-slip system is three times its width. This would put the length of the assumed NE wrench system around 100 km, not to exclude the possibility that the wrench system at hand is part of a much wider system, which would put the length of such a wrench system in the order of hundreds or even thousands of kilometres.

Geographically, Az Zalmah area represents the northeastern flanks of Al Kufrah Basin, a basin which covers territory in four neighbouring countries with an aerial extent of more than 400,000 km^2. This makes Az Zalmah area a representative sample for a regional model regarding the structure of this wrench system as part of NE Africa. Such a model has to take into account the plate tectonic settings of Africa throughout its geologic history.

The stress regime associated with strike-slip systems assumes horizontal maximum ($ó_1$) and minimum ($ó_3$) principal stress axes and a vertical intermediate principal stress axis ($ó_2$). These strike-slip systems usually occur in conjugate sets having opposite sense of displacements (Wilcox *et al,* 1973;

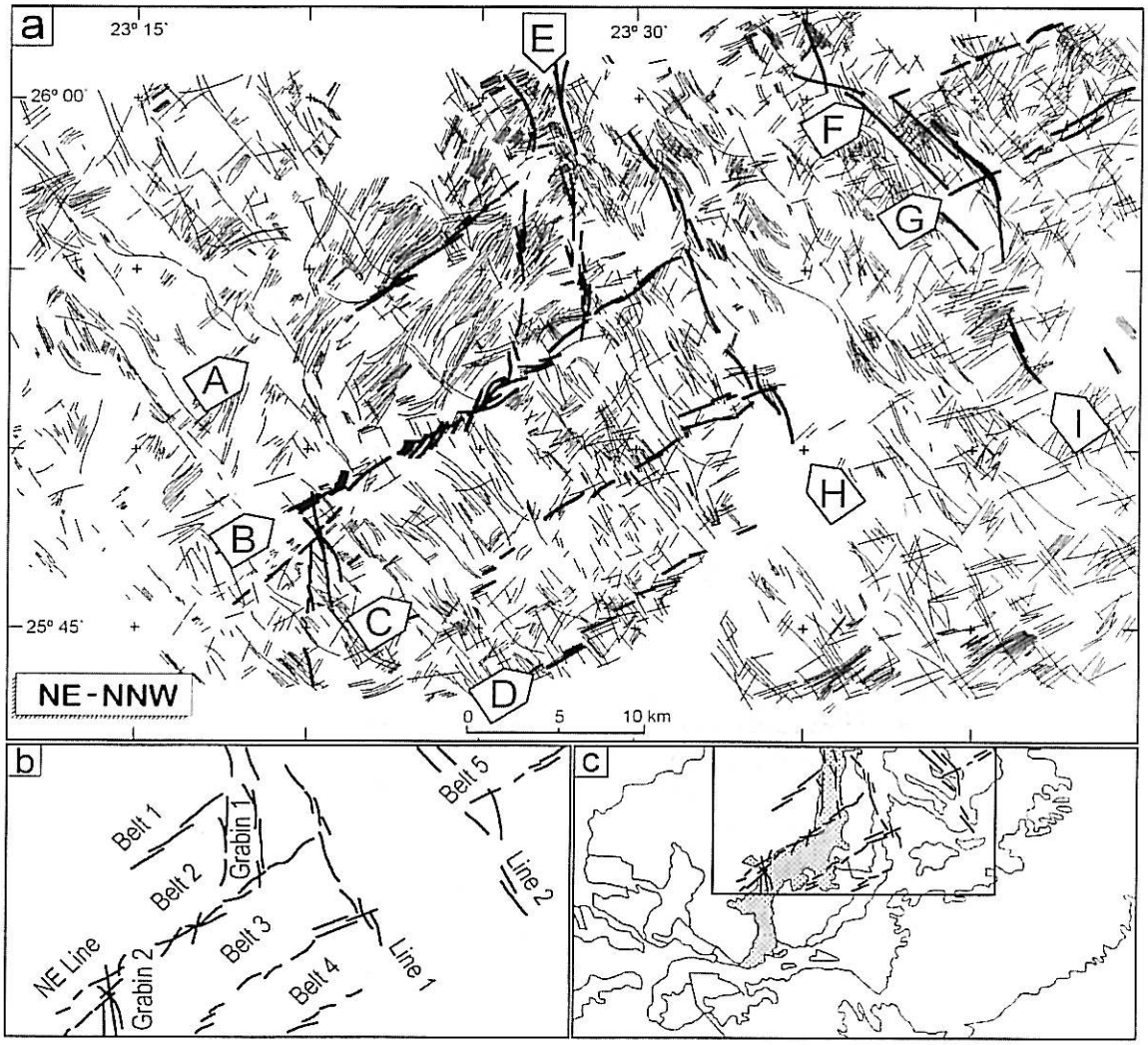


Fig. 7. (a). The combination of two trend maps bring out clear NE belts (b) marking wide shear zone. (c) Major belts relative to geological map (Fig. 2) and NS *En echelon* graben (slipped).

Ramsay, 1980). In Az Zalmah area, the maximum stress axis ($ó_1$) would assume a north-south orientation, representing the northward drift of Africa throughout the Phanerozoic, as postulated from several *Apparent Polar Wandering Paths (APWP)* for Gondwanaland (*e.g.* Morel and Irving, 1978; Scotese *et al*, 1979; Condie, 1982; Bachtadse and Briden, 1991). The conjugate set associated with this orientation would then assume a NE sinistral shear and a NW dextral shear. The tension fractures accompanying this setting would assume a north-south orientation, parallel to $ó_1$ (Fig. 9 d-1).

Rhomboidal fault-block structures are typical of *en echelon* faults within a strike-slip system. Depending on the *en echelon* sense (left- or right-stepping) and the sense of movement along the pair of strike-slip faults, pressure ridges and basins would develop in the area between the *en echelon* set in response to compression or extension, respectively (Wilcox *et al*, 1973; Aydin and Nur, 1982; Ramsay and Huber, 1987). Several of the fault-block structures which were visited in the field have a NW orientation (Fig. 8; see location of each structure on Fig. 2) ranging in size between 1 km ^{2} (Fig. 8 a) and more than 40 km ^{2} (Fig. 8 d), and depending on their size, large structures are bounded by relatively wide fault zones, while small structures are bounded by a single fault on each side.

Figure 8 a shows a NW left-stepping *en echelon* set of faults developing a pressure ridge, which could only develop from dextral strike-slip faults as shown kinematically. Fig. 8 b represents a horst with a left-stepping *en echelon* set, while fig. 8 c shows a small basin with a right-stepping *en echelon* set. Both of these structures are compatible with dextral strike-slip faults. Because wrench or shear zones usually occur in conjugate sets having opposite sense of displacements (Wilcox *et al,* 1973; Ramsay, 1980), it

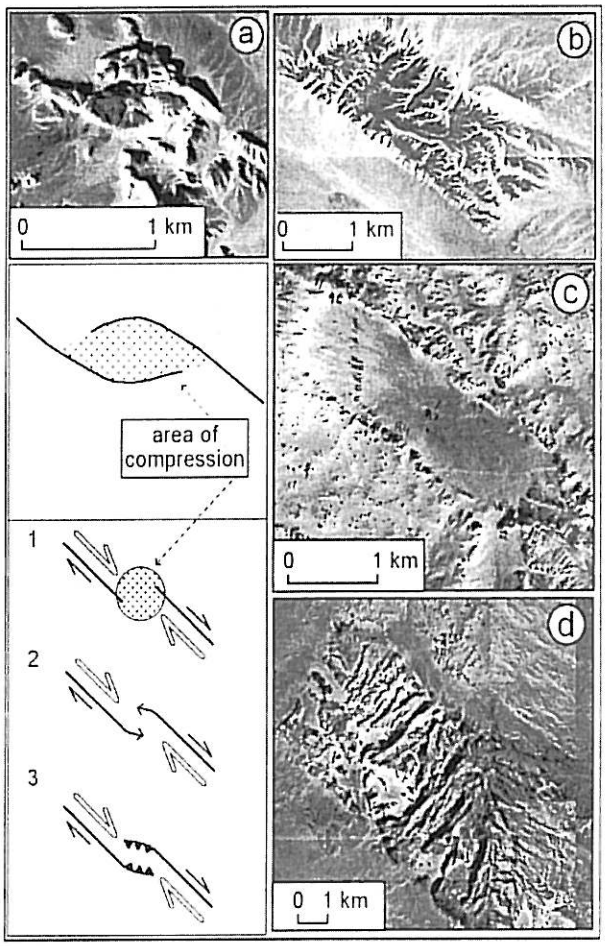


Fig. 8. Aerial photograph samples of structures found in the area. (a) pressure ridge caused by a left-stepping set of NW *en echelon* strike-slip faults. b, c and d: rhomboidal fault block structures, typical of a wrench system. See Fig. 2 for location of these structures.

is safe to assume that the NW trend represents the dextral antithetic component of the assumed wrench system (R_2 and X shears, see Fig. 9 d-1), whereas the NE fault sets and their associated belts–the throughgoing wrench system–would belong to the sinistral synthetic components, R_1 and P shears (Fig. 9 d-1).

If the proposed NE-trending wrench system were capable to move freely, the NE trend would have the highest fault population, and the fault-block structures (Fig. 8) would follow the same NE-trend. However, the NW trend, especially the WNW trend, is found to have the highest fault population, and the fault-block structures all have a northwestern orientation. Furthermore, while the NE-trending wrench zone with its four belts is wide enough to cause considerable lateral displacements, the NE faults show no such displacements as observed on the geological map of figure 2, nor have any of the faults visited in the field shown any appreciable displacement proportional to the width of the wrench zone.

This raises the possibility that the proposed wrench system might be inherently blocked. In clay model experiments (Tchalenko and Ambraseys, 1970; Wilcox *et al*, 1973) faults related to synthetic sinistral shear P (ENE faults in this case) start to develop only at an advanced stage of a wrench system, when the major fault is curved (Freund, 1974), which suggests that these faults, together with their complimentary set, the antithetic dextral shear X (WNW faults), emerge from the resistance of the main wrench system to any further movement. Freund (1974) considers interconnecting *en echelon* segments as one of the explanations for the curvature of a wrench system which causes the resistance of the main wrench system to any further movement.

The *en echelon* arrangement of tension fractures accompanying a shear zone is a good criterion in deciding whether the displacement along the shear zone is dextral or sinistral (Badgley, 1965; Billings, 1972; Wilcox *et al*, 1973). In our case, the north-south, right-stepping *en echelon* set of grabens (stippled on Fig. 9 b) are compatible with a sinistral NE-trending wrench system, whereas a dextral system would produce EW left-stepping *en echelon* grabens (Fig. 9 a).

Wilcox *et al* (1973), conducting clay model experiments simulating shear zones, state that: "*En echelon* tension fractures may form along a wrench zone in the initial stage of deformation, but they easily are destroyed as wrench displacement increases and compressive structures (folds and conjugate faults) become more prominent" (Wilcox *et al*, 1973, page 87). Two points in this statement are of great importance. Firstly, that tension fractures mark the initiation of a shear zone. We have shown that the different fault trends were either truncated or confined by *fault set E* (Figs. 5, 6, and 7). Such controlling effect of *fault set E* indicates that it was among the first structures to develop in the area, and the Upper Ordovician stratigraphic sequence filling this *en echelon* set of grabens give an estimated timing for their opening around Early to Middle Ordovician. Secondly, that tension fractures are destroyed after conjugate shears develop. Figure 9 **c** shows that the *en echelon* grabens filled by Melaz Shuqran and Mamuniyat formations must have been subjected to intense compression to develop the syncline-like structure it displays and to cause the alignment of Melaz Shuqran Formation along the margins of both segments of the *en echelon* set of

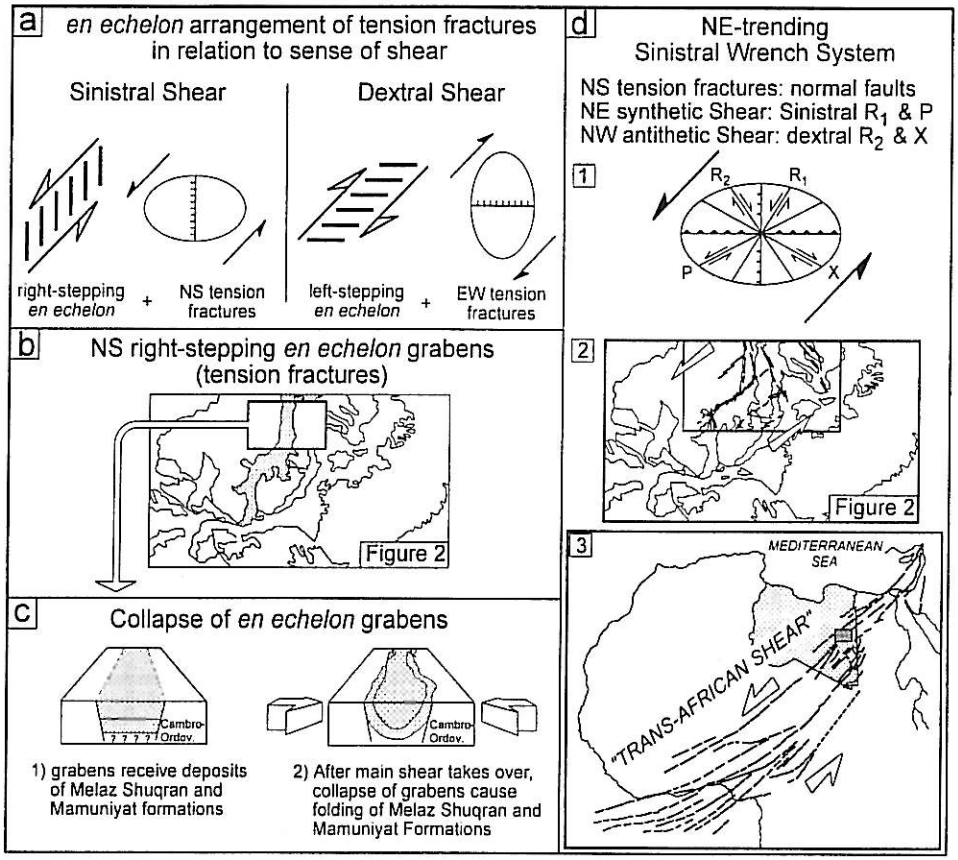


Fig. 9. A synopsis of the kinermatic interpretations for fault trends and the tectonic print over the stratigraphy in the area, See text for discussion e3 after Neev *et al* (1982).

grabens. Similar "folding" is nowhere found near these grabens, which indicates that this is a structural feature related only to these grabens. Furthermore, the axes of any regional folding associated with the northeast-trending shear zone at hand would assume an east-west trend, parallel to thrusts and reverse faults (see Fig. 9 d-1).

This NE configuration of the proposed wrench system could be part of the Trans-African Lineament (Nagy *et al*, 1977; Neev *et al*, 1982; Schandelmeier *et al*, 1997) which is a sinistral megashear system extending from the Benue trough of Nigeria via the Chad Basin and Al Kufrah Basin, into Egypt and the Levant, and terminating at the Anatolian fault in Turkey (Fig. 9 d-3).

MAGNETIC MAP

The existence of a northeast-trending wrench system in Az Zalmah area as was established earlier through the kinematic analyses of the structural trends and their relevant fault sets, as well as through the kinematic analyses of selected sample structures (Fig. 8) give a general picture for the tectonics in the area as it affected the geology on the surface, with no indication as to how the Precambrian basement was affected by the stress regime causing this wrench system.

A residual total intensity aeromagnetic map for Jabal Dalma area was published in 1980 by the Industrial Research Centre, Tripoli (see reference list). The magnetic map presented here (Fig. 11) is part of the surveyed area (see Index Map, Fig. 10). Both the geological map (Fig. 2) and the magnetic map cover exactly the same area, which would allow a three-dimensional correlation between the surface geology and the basement "topography".

Properties of a Magnetic Map

The magnetic contours, in gammas, represent the residual total intensity geomagnetic field relative to the theoretically calculated international geomagnetic reference field of 1975. The survey was carried at 122 ± 24 meters of ground clearance, with flight-line spacing of 1 km and tie line spacing of 5 km. This process of obtaining the residual field produced a contour map with an anomalous magnetic field. In

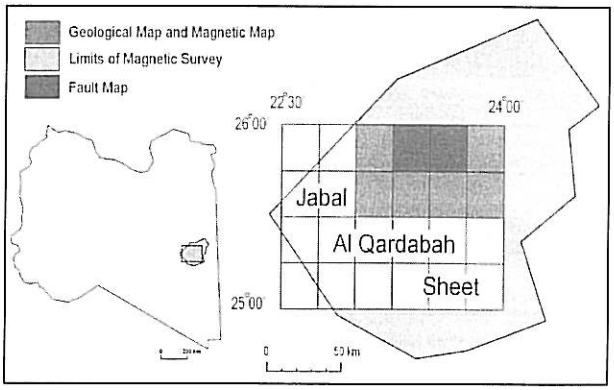


Fig. 10. Index map showing the area covered by the magnetic survey. Note that the area covered by magnetic map (Fig. 11) is the same as that covered by the geologic map (Fig. 2).

that sense it should be possible to interpret the magnetic map (Fig. 11) in terms of the structural and geological features causing the anomalous field, which should help in obtaining information about the subsurface geology of the area.

Particular properties regarding the magnetic survey operations and the magnetic map itself is important in enhancing the quality of the magnetic map and thus in utilising it as a qualitative tool in interpreting the configuration of the granitic basement. The first of these properties is the very low altitude of 98 to 146 meters at which the aeromagnetic survey was conducted. This should help in showing more sharply defined and better-resolved magnetic anomalies. Secondly, the clarity of the aeromagnetic survey and the sharpness of the anomalies are best achieved when the flight-line direction is normal to the trend of the geologic strike (Dobrin, 1976), as opposed to complicated anomalies arising from flight paths which make an oblique angle with the geologic strike. This criterion is fulfilled in the magnetic map presented here as the geologic map of figure 2 shows that the stratigraphic strike has a general northeast trend, while the direction for the flight-lines run along a N 35° W direction. And finally, the relatively small flight-line spacing of 1 km would also help in producing sharp and well-defined anomalies.

The magnetic map could be divided into three distinct zones: a North-western zone, a central zone, and a south-eastern zone (Fig. 11, insert).

North-Western Zone

Shows localised anomalies with high amplitudes and narrow wavelengths. These anomalies could represent shallow Precambrian intrusions or ferruginous Palaeozoic rocks. Within this zone, anomalies X1 and X2 (Fig. 11, insert) are the most prominent anomalies. These are the only two anomalies showing a northwestern trend. Structurally, anomaly X1 has a magnetic low and a clear right-stepping structural form, while X2 represents a magnetic high and a left-stepping structural form.

Central Zone

Sub-zone A is marked by a clear north-eastern alignment of closely-spaced contours, with its north-western and south-eastern limits taken at -200 gammas. The contours in the central "valley" of this sub-zone become less dense and reach -400 gammas,

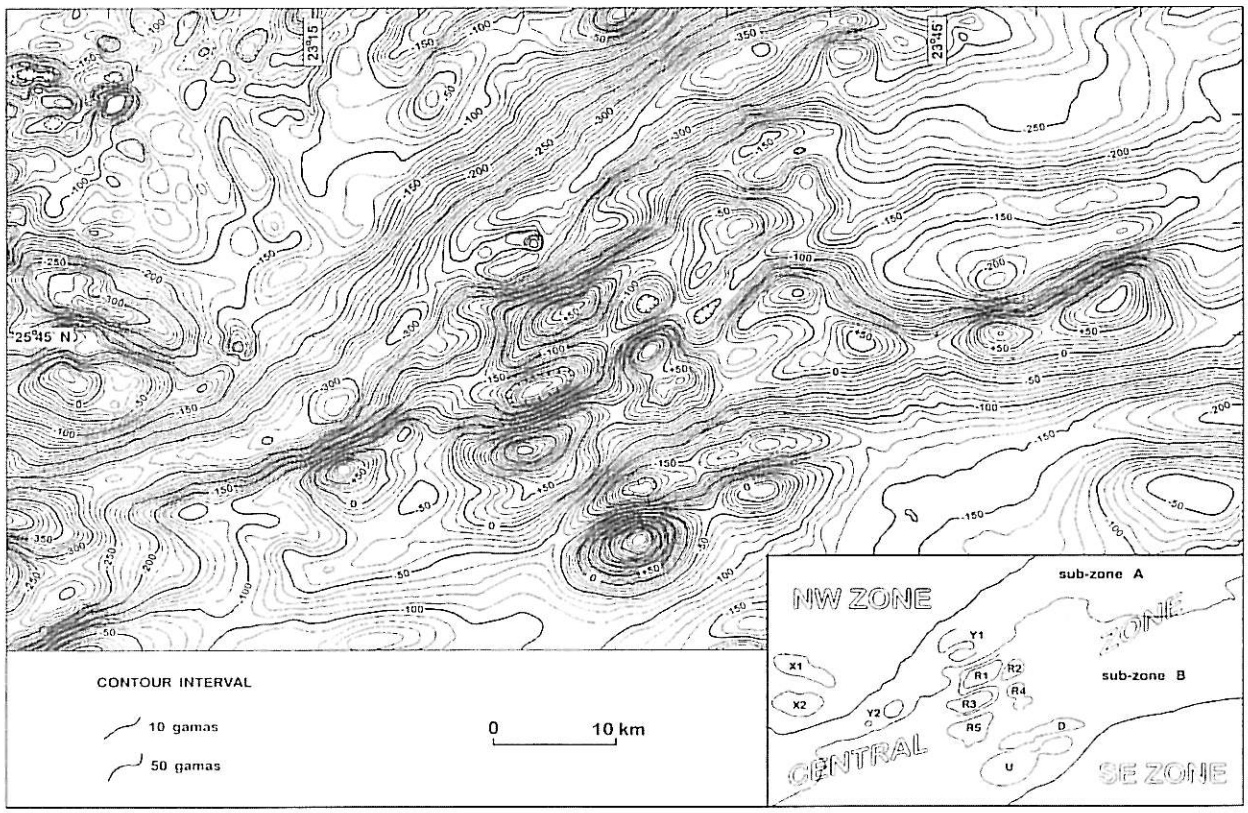


Fig. 11. A residual total intensity aeromagnetic map for part of Jabal Dalma area (Jabal Al Qardabah Sheet). Anomalous zones are given in inset, as well as individual anomalies discussed in text. See Fig. 10 for location of map with respect to mgnetic survey area.

the lowest in the area. Along the length of sub-zone A, the contours alternate in their linear trend between ENE and NNE directions. The two points at which this change in direction takes place are marked by Y1 and Y2. At Y1, the contours follow clear east-west closures, while at Y2 the contours form adjacent circular depressions that are offset along an east-west trend. East of longitude 23°40'00", the contours of sub-zone A are widely spaced and no longer have their distinct north-eastern alignment, probably reflecting increased thickness of sediments.

Within sub-zone B, the anomalies labelled R1 to R5 are bounded by conspicuous trends orientated ENE and NNE. Combined together, these trends form well defined rhomb-shaped "blocks" (especially anomaly R1) with values alternating between highs and lows, probably reflecting corresponding basement topography. Towards the southern limits of the central zone, anomalies U and D show a left-stepping form along an ENE trend, with anomaly D representing a magnetic low, while anomaly U a magnetic high of more than +250 gammas, the highest in the area.

South-Eastern Zone

The limits of this zone with the central zone is taken along an arbitrary line across which the contour spacing becomes markedly open. As this zone is closer to the centre of Al Kufrah Basin, the widely spaced contours and subdued anomalies could be due to the increased thickness of the sediments. Despite the subdued anomalies, the contours still retain their overall north-eastern trend.

Magnetic Anomalies

The three zones described above have been delineated according to the distribution of the individual magnetic anomalies marked in the insert of figure 11. These anomalies are believed to reflect the structural manifestation of the wrench system on the magnetic "basement". Figure 12 shows the relationship between the magnetic map and the structural trends deduced from the fault map (Fig. 4) and its filtered trend maps (Figs. 5 and 6). Among other correlative features between the structural trends and the magnetic map, the NE Line marking the median of the shear zone is the most striking of these features, where it coincides exactly with the central valley of sub-zone A (Fig. 12). This indicates that there is a direct correlation between the structure as it is seen on the surface, and the granitic basement as reflected by the magnetic map. As such, the magnetic anomalies could be interpreted within the context of the proposed structural model of the northeast-trending wrench system.

Anomalies X1 and X2

Within the area of figure 11, these are the only two anomalies which have a NW trend. When these two anomalies are viewed within the geological framework in the area, it can be seen that anomaly X1 corresponds structurally to a graben represented by Upper Ordovician units, while anomaly X2 lies beneath a horst represented by Cambrian–Lower Ordovician units (Fig. 13, a). Corresponding 'grabens' and 'horsts' are also seen on the magnetic map, where anomaly X1 represents a magnetic low, and X2 represents a magnetic high.

By applying the proposed mechanical model (Fig. 9, e-1) anomaly X1 could be resulting from the interaction between the north-south normal faults and the WNW antithetic X-faults (see Fig. 13, b). Structurally, the northern limits of this anomaly is represented by a right-stepping set of dextral faults

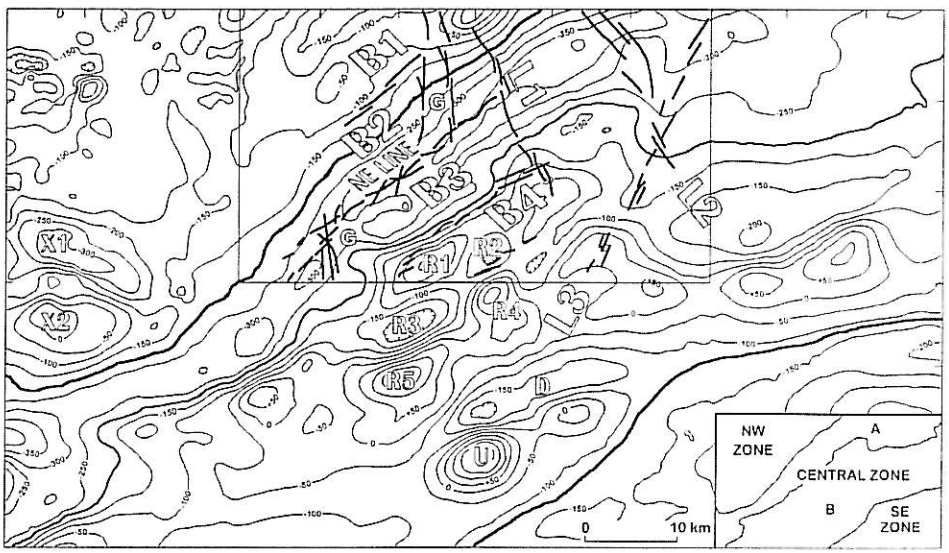


Fig. 12. Relation between structural trends associated with proposed wrench system deduced from fault map (Fig. 4, see also Fig. 7.) and magnetic map (Fig. 11).

joined by a north-south normal fault (Fig. 13, c). Such a configuration would create an extensional stress system, leading to an ideal pull-apart basin.

Anomaly X2 (Fig. 13, d) is interpreted as bounded on its northern limits by a left-stepping set of dextral X-faults joined by a NE sinistral fault which could belong to either R_1 or P-faults. This fault set develops a compressional state of stress. The other three faults bounding this anomaly would add to this compressional state of stress, where the northern and southern corners of this structure are subjected to compression, while the eastern and western corners are subjected to extension. Combining these kinematic conditions would lead to an overall counterclockwise rotation of the whole block, which would add to the compression exerted on this structure, thus causing it to be uplifted.

The two anomalies X1 and X2, with their corresponding graben and horst on the surface, are well related mechanically to each other in the sense that the extension developing in X1 would induce compression on X2 and *vice versa* . This could of course be related from a geophysical point of view to the dipole effect of magnetic anomalies, but since the magnetic map is a residual one, the anomalies are enhanced by the removal of the regional, therefore these anomalies are representative for fault block structures especially that they are bounded by elongated or linear zones of steep magnetic gradients suggesting faulted and displaced magnetised blocks (Dobrin, 1976).

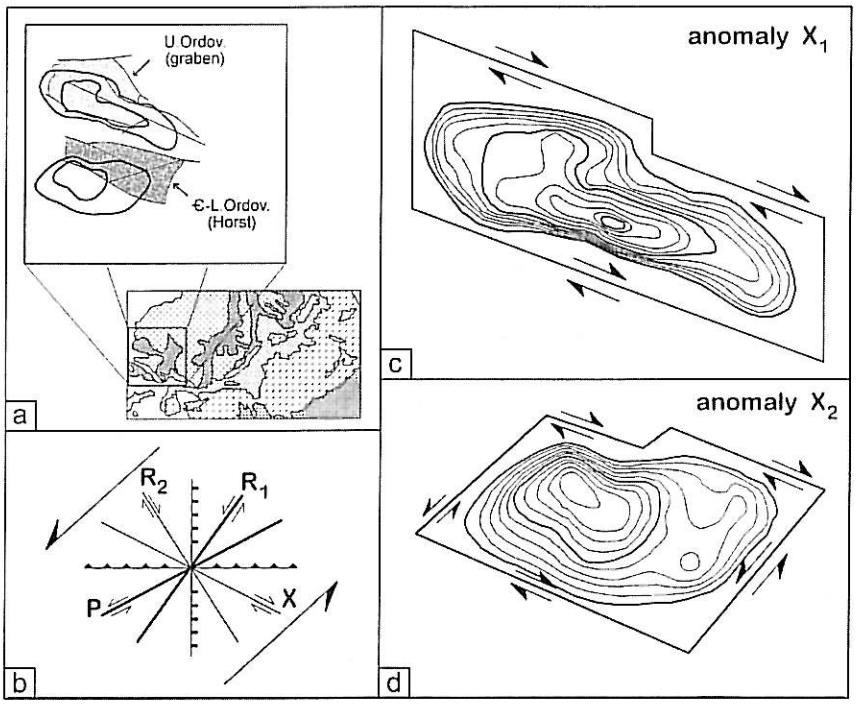


Fig. 13. Applying mechanical model to magnetic anomalies X1 and X2, a: location of anomalies relative to NW-trending structures on geologic map (Fig. 2), b: mechanical model, c: kinematics of anomaly X1, d: kinematics of anomaly X2.

Anomalies R1-R5

These anomalies (for location see Figs. 12 and 14, a) are found beneath the highly displaced outcrops of Melaz Shuqran Formation just to the east of the southern segment of the right-stepping *en echelon* set of grabens. In fact, the whole area above these anomalies is the most fractured part of the geological map of figure 2. These anomalies are believed to be the result of the interaction between the synthetic sinistral shears R_1 and P. Combined together, these faults would create lozenge-shaped structures with an overall east-northeast direction. As figure 14 c shows, these structures start with the development of a series of right-stepping sinistral faults R_1. Due to geometrical restrictions, the P-faults cannot operate simultaneously with the R_1 faults, rather only in sequence since they both belong to the same conjugate set (Freund, 1974). This will create the lozenge-shaped structures (stage 2, Fig. 14 c) which will be subjected to clockwise rotation (stage 3) since they are bounded by sinistral faults on all sides. These duplex structures have a contractional geometry and are imbricated by P shears between pre-existing R shears (Woodcock and Fischer, 1986, Fig. 7 c). Once they start to develop progressively, each unit lozenge would rotate independently, forcing the neighbouring lozenge to absorb part of the stress exerted upon it, and *vice versa*. The progressive development and rotation of these blocks would create volume excess at restraining edges and volume deficit at releasing edges of the lozenge or rhomboid blocks making up this duplex structure. To accommodate for these volume changes, the mechanical system necessitates the discrete uplift and subsidence of the individual blocks in an alternating fashion. This is clearly seen on the magnetic map, where anomalies R1, R4, and R5 are uplifted blocks, while anomalies

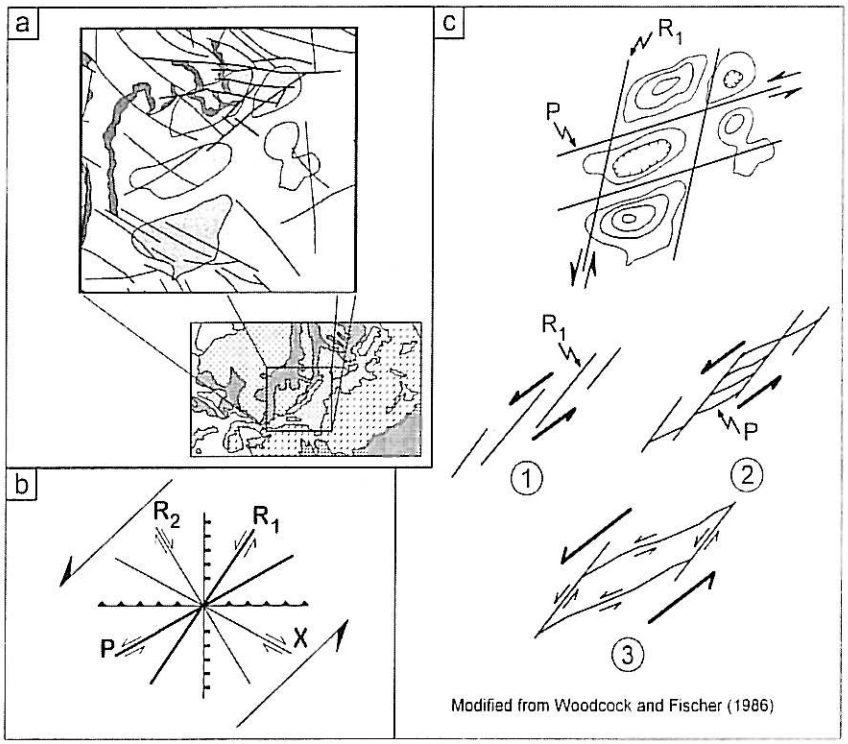


Fig. 14. Applying kinematic model to magnetic anomalies R1 to R5. a: location of anomalies relative to geologic map (Fig. 2.). b: kinematic model. c: interpretation of mechanical development of anomalies.

R2 and R3 are down-thrown blocks. It should be pointed out that while the internal rotation within each block is clockwise, the external rotation (heavy arrows in stages 1-3, Fig. 14 c) is counterclockwise, the latter of which represents the proposed shear system and represented by the outer arrows in figure 14b. This could further explain the limited volume change created by the rotation of the individual blocks, where the outer rotation would counterbalance this volume change and even help the whole duplex system to reach equilibrium by allowing the uplift and subsidence of the individual blocks.

Anomalies D and U

These two anomalies lie beneath Devonian rocks on the geological map (see Fig. 15 a) and are among the anomalies found within sub-zone B on the magnetic map (Fig. 12). They are both bounded by ENE left-stepping sinistral faults and NNE right-stepping sinistral faults (Fig. 15 c). These two structures are created by P-faults (ENE) isolating lozenges already cut by R shears (NNE). In this setting they would have an extensional geometry (Woodcock and Fischer, 1986, Fig. 7b). Anomaly D is cut into three lozenges and has a clear extensional form as seen by the negative magnetic contours. Anomaly U, on the other hand, has positive magnetic contours, the highest within the area of figure 11, which would suggest a contractional geometry. It will be shown later that in spite of the positive magnetic contours of anomaly U, it still represents the extensional geometry associated with the model of figure 15 c.

The locked fault structure (Fig. 8, a) which is also a duplex structure made up of one lozenge, is located above the two anomalies U and D (Fig. 15, d). These two anomalies and the anomalies R1-R5, discussed earlier, seem to be associated with very complex structures on the surface. This is probably resulting from the rotation of individual blocks making up these anomalies, as well as the vertical movements of these blocks in association with this rotation.

Sub-zone A: Central Valley

One of the striking features of the magnetic map (Fig. 11) is the linearity of sub-zone A with contours starting at -150 gammas and reaching -400 gammas, which from a structural point of view represents a very deep valley. This *central valley* (Fig. 16) displays a very peculiar pattern in which the contours deviate from their northeast alignment at points Y1 and Y2 (Fig. 16) to become aligned along an east-west closer, as at Y1, or marked by an east-west offset at Y2. This overall configuration gives the central valley a distinct right-stepping *en echelon* setting. This *en echelon* setting is highlighted by the hatched line along the centre of the valley in Figure 16, but could be viewed just as well on the magnetic map of Fig 11.

The location of the *NE-Line* exactly on this valley (Fig. 12) supports its *en echelon* setting, thus allowing for the line drawn on figure 16 along the central valley to represent a sinistral shear system. Such a configuration will build compressional force at the joining segments of the right-stepping *en echelon* (Fig. 16, a). Within the framework of the proposed shear system, the dominance of the NW trend–especially the WNW trend–was attributed to a locked shear system. A sinistral, left-stepping *en echelon*

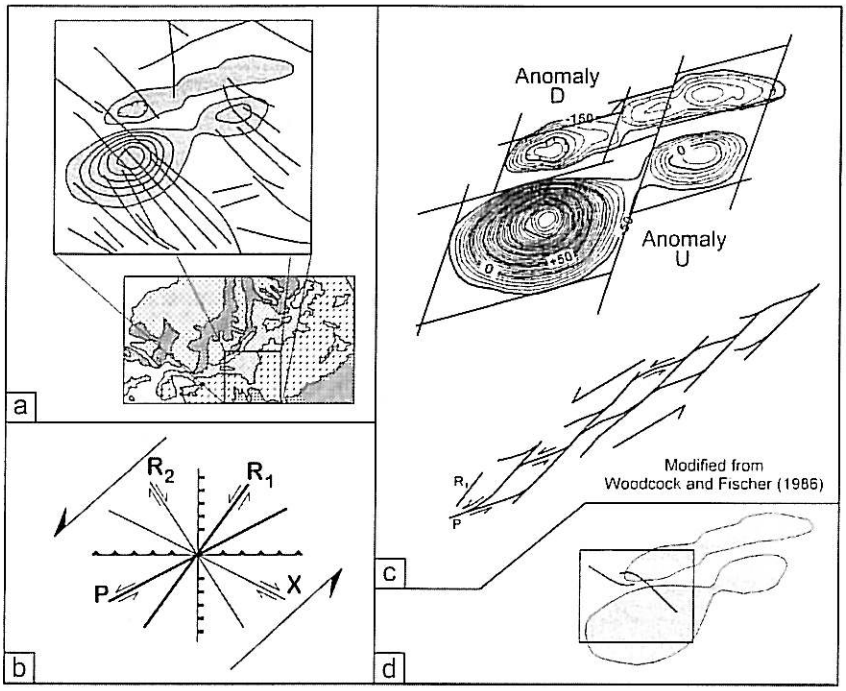


Fig. 15. Applying kinematic model to magnetic anomalies U and D. a: location of anomalies relative to geologic map (Fig. 2). b: kinematic model. c: interpretation of mechanical development of anomalies. d: location of anomalies relative to locked fault (Fig. 8, a).

system (Fig. 16, b) does not follow the contours of the central valley on the magnetic map, nor does it fit with the dominance of the NW trend in the area.

Sub-zone B: En echelon Folds

En echelon folding is cited in the literature as an indication for the existence of a wrench system even if no clear fault system is observed (*e.g.* Campbell, 1958; Wilcox *et al*, 1973; Harding, 1974; Harding and Lowell, 1979; Reading, 1980; Allen and Allen, 1990; Schandelmeier *et al*, 1997). The axes of these *en echelon* folds are found at right-angels to the direction of the maximum principal compressive stress ($\acute{o}_1$) causing the shear system (see Fig. 9,d-1).

The stepping of these *en echelon* folds is an indication for the sense of movement of a northeast-trending shear system causing these folds: left-stepping *en echelon* folds are associated with a left-lateral or sinistral shear system; right-stepping *en echelon* folds are associated with a right-lateral or dextral shear system. Figure 17 shows the possible orientation of such folds in the area, relative to a northeast-trending wrench system, given as either sinistral or dextral (Fig. 17, A and C, respectively). In the case of a sinistral wrench system, the *en echelon* folds have east-west fold axes, while the dextral wrench system will develop north-south fold axes.

Two corresponding world examples are given for comparison. The Dead Sea rift, a north-south sinistral strike-slip fault system (Quennell, 1959), shows left-stepping *en echelon* folds with northeast axes (in

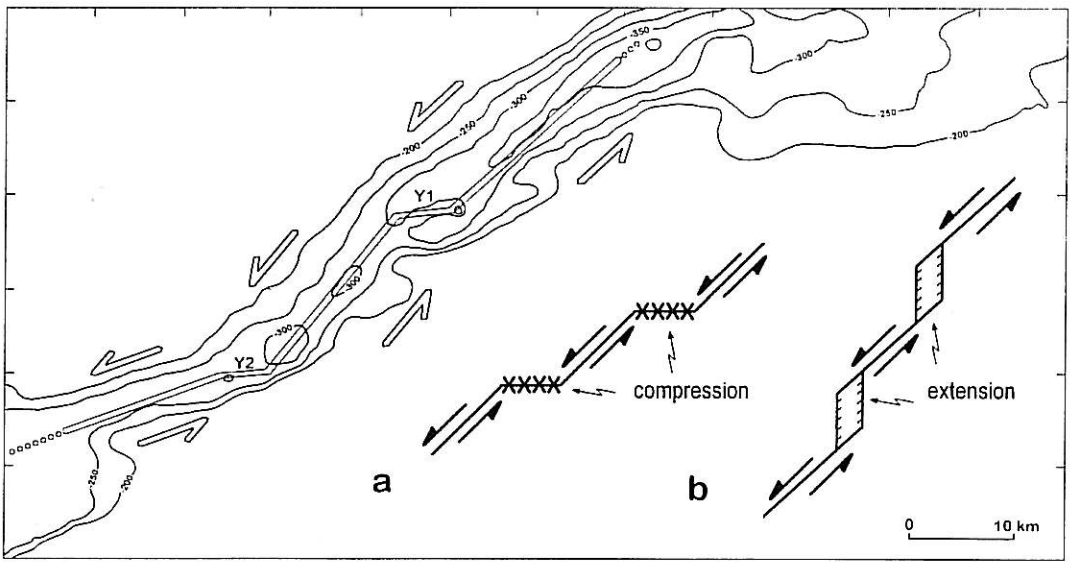


Fig. 16. The central valley within sub-zone A, interpreted as a sinistral shear system with a right-stepping *en echelon* set (a), where the compression (xxx) explains why this system is a "locked" system, dominated by P and X shears (NW faults). A left-stepping configuration (b) does not agree with the magnetic map nor with the dominance of P and X shears.

Fig. 17 B it is orientated to match the case in A, the study area). The San Andreas dextral wrench system, with its north-west trending main strike-slip fault (Fig. 17, D), has right-stepping *en echelon* folds with their axes trending at about west-northwest (Fig. 17 D, this is also orientated to be aligned with the case in C).

Between cases A and C, figure 17, the expected orientation of these folds would be that of case A since this setting, based on the structural information gathered so far, is identical to the structural model proposed (Fig. 9, d-1). Sub-zone B (Fig. 11) could be viewed as representing a set of east-northeast, left-stepping *en echelon* folds. The proposed *en echelon* folds are highlighted on figure 18 A by a 5 gamma contour interval on the background of the magnetic map with a 50 gamma contour interval. These folds are seen as anticlines and synclines with an east-northeast plunge (Fig. 18 b). The plunge of the individual folds is accompanied by a flatter overall plunge. This association between individual and regional plunge is in agreement with one of four possibilities given by Campbell (1958) for *en echelon* folds in the Kalgoorlie district in Western Australia. The four possibilities are based on the direct relationship between the *en echelon* pattern of folds (whether left-stepping or right-stepping) and the *en echelon* pattern of structure contours drawn on such folds (also being either left-stepping or right-stepping). In our case, the conditions are as follows: left-stepping *en echelon* folds in association with left-stepping contours will result in steep individual plunge of folds within a flat overall or regional plunge. These conditions are fulfilled, as seen in figure 18, where the *en echelon* pattern of the folds is clearly left-stepping, and if one is to draw structure contours on top of these folds, they will clearly show a left-stepping pattern (compare between the contours of more than 200 gammas at the western part of anomaly U, figure 15, with those of 0 gamma at the eastern end of the same anomaly). Figure 18 C is the model given by Cambell to show the relation between individual and regional plunge. Although it represents flat individual plunge within a steep regional plunge, whereas the case proposed here is the combination of steep individual plunge with flat overall plunge, nevertheless, this three dimensional model serves the purpose where it is orientated to resemble the configuration of the folds seen on the magnetic map (Fig. 18 a).

It should be pointed out that anomalies R1-R5 (Fig. 14) and anomalies U and D (Fig. 15) described earlier, are part of the *en echelon* folds discussed here. While these anomalies were described in the context of lozenges cut by R and P shears, they can still be part of the *en echelon* folds discussed here. Both structural events (folding and faulting) can be

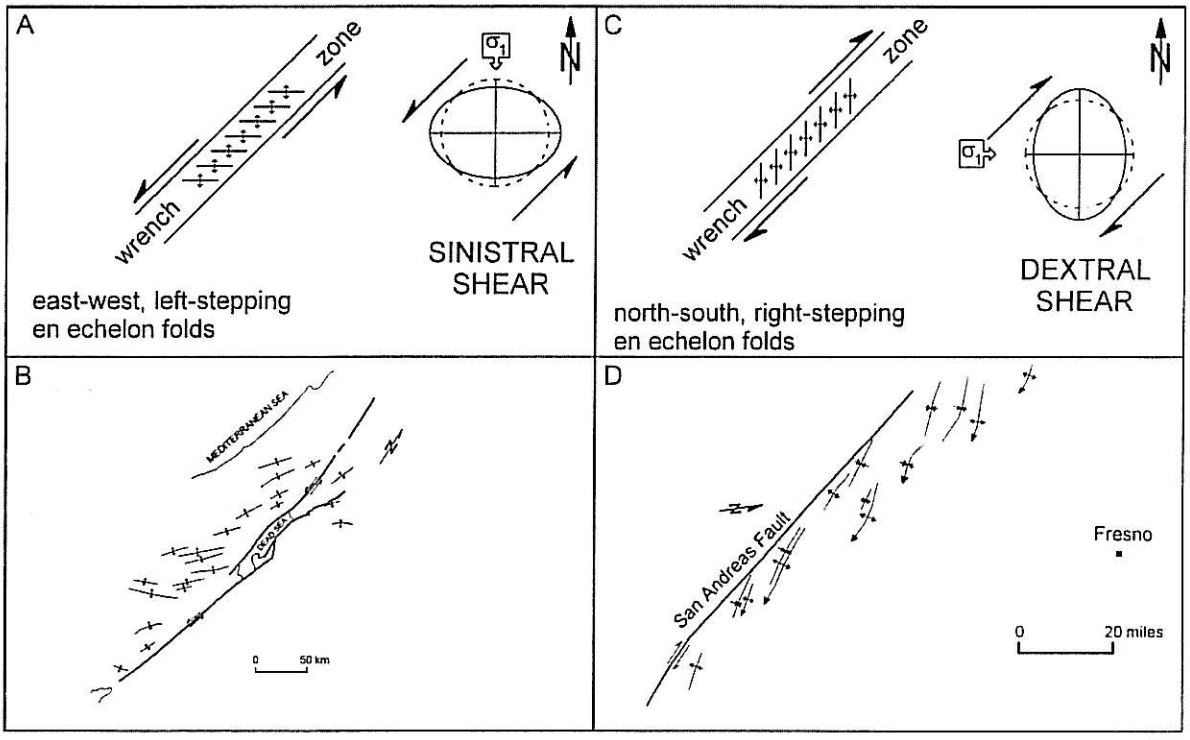


Fig. 17. The alignment of *en echelon* folds in a predicted orientation depending on the wrench system being A: sinistral or C: dextral. B: The Dead Sea Rift System (modified from Quennell, 1959). D: The San Andreas Fault System (modified from Wilcox *et al*, 1973.

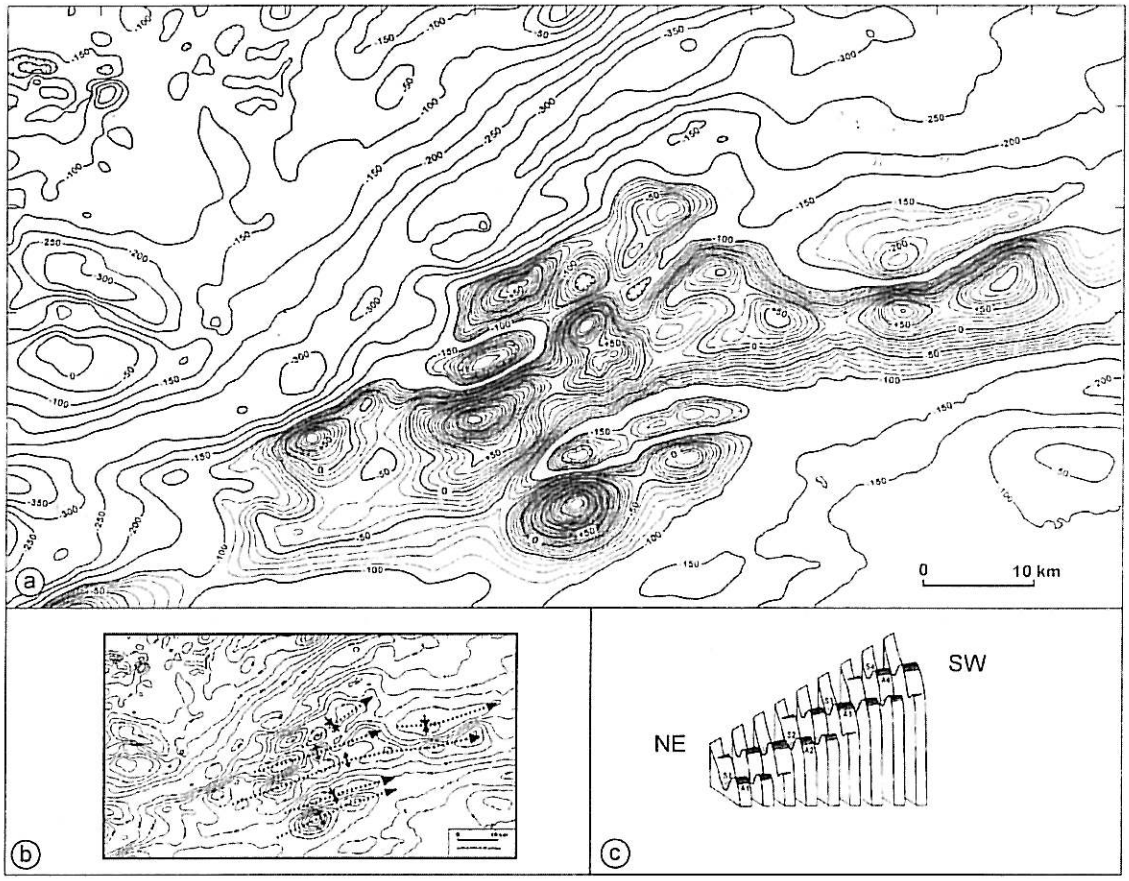


Fig. 18a. Sub-zone B, highlighted to show the possible *en echelon* configuration of folds in the basement in response to the kinematic model proposed. B: Trends of fold axes showing plunge to east-northeast. C: A 3D representation of folds, modified from Cambell (1958).

accommodated for within the framework of the proposed mechanical model. A pertinent example is given by Harding and Lowell (1979) for the evolution of a wrench fault developing hydrocarbon trapping, modelled after examples in California. This example is presented in figure 19 to match the case for a sinistral wrench system, which is the case in Dalma area (Survey area, see Fig. 10) while the original California example is that of a dextral wrench system. It can be seen that the initial stage creates connected *en echelon* folds (Fig. 19 A). At a later stage, and while the axes of these folds continue to extend east-west, the crests of these folds are cut by sinistral faults having either left-stepping or right-stepping *en echelon* patterns (Fig. 19 B). At a more advanced stage (Fig. 19 C) the folds are dissected by the sinistral faults, for which these faults will join together to form either rhomboid horsts or grabens, depending on the *en echelon* offsets they have.

There is a direct relationship between the structural setting of a wrench system and the hydrocarbon accumulation within the closures at the crests of the *en echelon* folds. This is shown by the

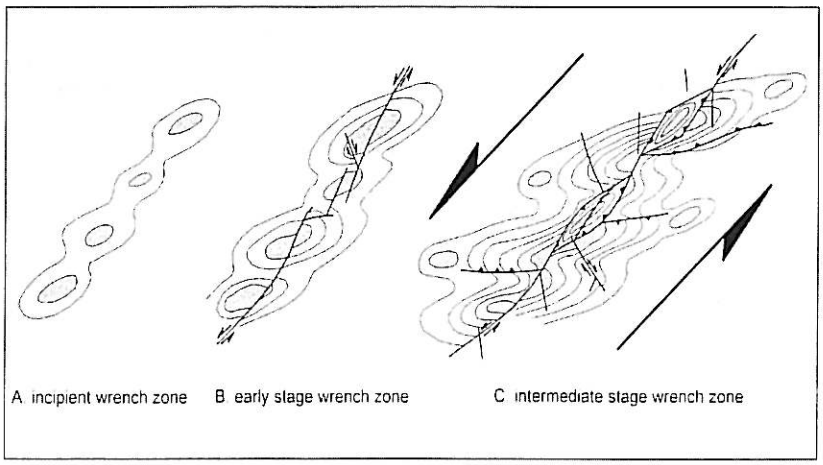


Fig. 19. The revolution of a wrench system, developing *en echelon* folding followed by faulting which will create lozenge or rhomboid structures. Shaded regions represent potential hydrocarbon traps within closures in fold crest modified

shaded closures in figure 19, where they represent the ideal hydrocarbon traps, being isolated at the highest levels of the structures and sealed by faults at predicted levels and orientations. This model is in good agreement with the *en echelon* fold pattern shown on figure 18, as well as with the kinematic layout given for the magnetic anomalies R1-R5 and both D and U anomalies. With the assumption that the magnetic map and all the structures deduced from it being that of the granitic basement, and if such *en echelon* folding in this basement is transmitted to the sedimentary cover, then the model proposed here could be adopted for hydrocarbon exploration in the area, where it could prove to be productive.

While most of the structural trends identified on the surface were shown, from the qualitative evaluation of the magnetic map, to have conforming structural influence at the "basement" level, the north-south *en echelon* set of grabens (stippled on Fig. 7 c) had no print on this basement (this is clearly seen on Fig. 12), despite their profound impact on the distribution of faults in all the filtered trend maps. According to the mechanical model of figure 9 d-1, the structural trends defining Graben 1 and Graben 2 (Fig. 7 b) belong to the north-south normal faults of that model. These are the tension fractures of Wilcox *et al* (1973), and according to their clay cake experiments, these tension fractures are short-lived and only develop at the early stages of wrenching, if they develop at all. Accordingly, these *en echelon* grabens are not expected to extend vertically to the depth of the granitic basement, firstly because they develop during the early stages of wrenching, they are easily taken over by folds and conjugate faults, and secondly, these same folds and conjugate faults will build up compressive stresses which will seal the walls of these *en echelon* grabens and will not allow them to extend vertically beyond the shallow depths of the crust, hence they will arguably not show on the magnetic map. This is a supporting evidence for the nature of the *en echelon* set of grabens in the area as discussed under *Structural Framework*, and a conformation for the mechanical model (Fig. 9 d-1) proposed for the area.

REFERENCES

Allen, P. A. and Allen, J. R., 1997. *Basin Analysis: Principles and Applications*. Blackwell Scientific Publications, Oxford. 441 p.

Aydin, A. and Nur, A., 1982. Evolution of pull-apart basins and their scale independence. *Tectonics*, **1**, 91-105.

Bachtadse, V. and Briden, J. C., 1991. Palaeomagnetics of Devonian ring complexes from the Bayuda Desert, Sudan: new constraints on the apparent polar wandering path for Gondwanaland. *Geophys. J. Intern.*, **104**, 635-646.

Badgley, P. C., 1965. *Structural and Tectonic Principles*. Harper & Row, New York. 521 p.

Bellini, E. and Massa, D., 1980. A stratigraphic contribution to the Palaeozoic of the southern basins of Libya. In: M. J. Salem and M. T. Busrewil (eds.) *The Geology of Libya*. Academic Press, London, **I**, 3-56.

Billings, M. P.,1972. *Structural Geology*. Prentice Hall, New Jersey. Third Edition. 606 p.

Campbell, J. D., 1958. En echelon folding. *Econ. Geol.*, **53**, 448-472.

Condie, K. C., 1982. *Plate Tectonics and Crustal Evolution*. Pergamon Press, New York. 310 p.

Dobrin, M. B., 1976. *Introduction to Geophysical Prospecting*. McGraw-Hill, New York, 630 p.

Freund, R., 1974. Kinematics of transform and transcurrent faults. *Tectonophysics*, **21**, 93-134.

Harding, T. P., 1974. Petroleum traps associated with wrench faults. *Bull. Am. Assoc. Petrol. Geol.*, **58**, 1290-1304.

Harding, T. P. and Lowell, J. D., 1979. Structural styles, their plate-tectonic habitats, and hydrocarbon traps in petroleum provinces. *Bull. Am. Assoc. Petrol. Geol.*, **63**, 1016-1058.

IRC, 1980. Residual Total Intensity Aeromagnetic Map of Jabal Dalma Area; 1:250 000. 1980. Compiled by Pacific Aero Survey Co., Tokyo, Japan., *Industrial Research Centre*, Tripoli, Libya. Unpublished Rep.

Klitzsch, E. H., 1966. Comments on the geology of the central parts of southern Libya and northern Chad. *In:* J. J. Williams *(ed.) South-Central Libya and Northern Chad: a Guidebook to the Geology and Prehistory. Petrol. Explor. Soc. Libya*, 8th Annu. Field Conf., 1-17.

Morel, P. and Irving, E., 1978. Tentative paleocontinental maps for the early Phanerozoic and Proterozoic. *J. Geol.*, **86**, 535-561.

Nagy, R. M., Ghuma, A, and Rogers, J. J. W., 1977. A crustal suture and lineament in Northern Africa. *Tectonophysics*, **31**, T67-T72.

Neev, D., Hall, J. K., and Saul, J. M., 1982. The Pelusium Megashear System across Africa and associated lineament swarms. *J. Geoph. Research.*, **87**, 1015-1030.

Nettleton, L. L., 1976. *Gravity and Magnetics in Oil Prospecting*. McGraw-Hill, New York, 464 p.

Quennell, A. M., 1959. Tectonics of the Dead Sea rift. *Asociación de Servicios Geológicos Africanos 20th Internat. Geol. Cong.*, México, D. F., 1956, Actas y Tr., 385-405.

Ramsay, J. G., 1980. Shear zone geometry: a review. *J. Struct. Geol.*, **2**, 83-99.

Ramsay, J. G. and Huber, M. I., 1987. *The Techniques of Modern Structural Geology*, vol. 2: Folds and Fractures. Academic Press, London, 700 p.

Reading, H. G., 1980. Characteristics and recognition of strike-slip fault systems. *In* P. F. Ballance and H. G Reading (eds.) *Sedimentation in Oblique Slip Mobile Zones. Spec. Publ. Internat. Assoc. Sedimentol.*, Blackwell, Oxford, **4**; 7-26.

Schandelmeier, H., Stern, R. J., Reynolds, P.-O., and Abdel Rahman, E. M., 1997. The Late Neoproterozoic (Venidian, ca. 570 Ma). *In* H. Schandelmeier and P.-O. Reynolds (eds.) *Palaeogeographic-Palaeotectonic Atlas of North-eastern Africa, Arabia, and Adjacent Areas*. Balkema, Rotterdam., 5-13.

Scotese, C. R., Bambach, R. K., Barton, C., Van der Voo, R. and Ziegler, A. M., 1979. Paleozoic base maps. *J. Geol.*, **87**, 217-277.

Tchalenko, J. S. and Ambraseys, N. N., 1970. Structural analysis of the Dasht-e Bayaz (Iran) earthquake fractures. *Bull. Geol. Soc. Am.*, **81**, 41-60.

Wilcox, R. E., Harding, T. P., and Seely, D. R., 1973. Basic wrench tectonics. *Bull. Am. Assoc. Petrol. Geol.*, **57**, 74-96.

Woodcock, N. H., and Fischer, M., 1986. Strike-slip duplexes. *J. Struct. Geol.*, **8**, 725-35.

Petroleum Res. J. Vol. 15 (2003); P. 23–32, 15 Figs.

Late Cretaceous Stratigraphy and Palaegeography of Zaltan Platform (Concession 59), South Central Sirt Basin, Libya

Miloud M. Abougares and Mahmud T. El-Bakai*

التتابع الطبقي والجغرافية القديمة بمنطقة مسطح زلطن بعقد الامتياز 59 جنوب وسط حوض سرت – ليبيا

ميلود أبو قارص و محمود البكاي

ينتشر التتابع الطبقي التابع للعصر الطباشيري العلوي فوق معظم أجزاء حوض سرت الرسوبي، ويحتوي على طين بحري وحجر جيري، ويمتد عمره الجيولوجي بين زمن التوروني وحتى المستريختي.

تنقسم التتابعات الطبقية في منطقة الدراسة إلى خمسة تكاوين واضحة المعالم ومميزة، ويعزي توزيعها إلى الجغرافيا القديمة لطبوغرافية المناطق السائدة وقت الترسيب ويمكن ترتيب هذه التكاوين تصاعدياً على النحو التالي:

الحجر الرملي التابع إلى عصر ما قبل الطباشيري العلوي، متبخرات تكوين إيثيل (التوروني) والمتكون من مسطحات مياه ضحلة ومحصورة، تكوين الرشمات الذي يمتد عمره من الكونياكيان إلى السانطوني والمتكون من رواسب بحرية ضحلة مفتوحة ومحمية جزئياً، تكوين سرت الطيني وهو مسطح ضحل ومحصور وأخيراً الحجر الجيري لتكوين الواحة التابع للعصر الماستريختي وهو مسطح جيري ضحل.

إثناء الزمن الطباشيري العلوي ارتفع منسوب سطح البحر وتقدم باتجاه الجنوب فوق صخور القاعدة الجرانيتية أو فوق الحجر الرملي للعصر ما قبل الطباشيري العلوي وإبان العصر السانطوني وبداية العصر الكمباني تقدم البحر تدريجياً ليغمر معظم مناطق الواحة والدفة.

أما في نهاية الطباشيري العلوي أي خلال زمن المستريختي فقد استمر البحر في التقدم باتجاه الجنوب وغمر معظم المرتفعات القديمة وذلك على إمتداد مسطح زلطن. وخلف هذا جزيرتين غير متصلتين كمناطق غير مغطاة تعرفان اليوم بحقل الواحة وحقل الدفة، وتم بناء أحزمة جيرية حولهما بسبب تقدم البحر إلى الأعماق وكجزء من هذه المرحلة تكونت السحنات الجيرية المعروفة بسحنات خزان الواحة النفطي الجيري حيث تغيرت جانبياً باتجاه مركز الحوض إلى تتابع طبقي من رواسب طينية تعرف بتكوين سرت الطيني.

Abstract: *The Upper Cretaceous stratigraphic sequences are widespread over the whole of Sirt Basin and consist of marine shale and limestone, ranging in age from the Turonian up to the Maastrichian. The sequences, in the study area (Zaltan platform), are divided into five clearly recognizable formations and their distribution is related mainly to the palaeogeography of the pre-existing topography. In ascending order they are; Pre-upper Cretaceous sandstone, evaporitic Turonian Etel Formation (shallow water restricted platform), Coniacian/ Santonian Rachmat Formation (shallow open marine, slightly protected), Campanian Sirte Shale (shallow*

*Petroleum Research Centre, P.O. Box 6431, Tripoli, Libya.

restricted platform) and Maastrichian Waha Limestone (shallow carbonate platform).

Upper Cretaceous sea transgressed towards the south either over the basement and granite wash or over Pre-upper Cretaceous sandstone. It encroached gradually on the Al Wahah and Ad Deffah areas at the close of Santonian and the beginning of Campanian time. During Maastrichian time, sea continued to transgress southwards and covered most of palaeohighs in the Zaltan platform. Two separated islands were left uncovered, forming the palaeohigh (Al Wahah and Ad Deffah field area). The carbonate belts around them grew narrower as the sea got too deep for the carbonate deposition. Carbonate facies, known as Waha reservoir facies, were developed on the highs and changed laterally basinward into shally sequence deposits of the Sirte Shale.

INTRODUCTION

The study area is located in the south central part of the Sirt Basin (Fig.1). It covers Concession 59 including Al Wahah, Ad Deffah fields and Al Harash area in Zaltan platform. This study was carried out in order to further understand the subsurface geology and the palaeogeographic distribution of the Late Cretaceous stratigraphic sequences. It includes from base to top; the Pre- upper Cretaceous, Etel, Rachmat, Sirte Shale, Waha Limestone and Kalash Formation. The relation between structural system and facies development in the Zaltan platform is also considered.

The present study is based on subsurface well logs data, collected and analyzed from twenty five wells located in Concession 59 of the Al Wahah, Ad Deffah field areas. Regional geological cross-sections, palaeogeographic maps and schematic block diagrams were also constructed for this purpose.

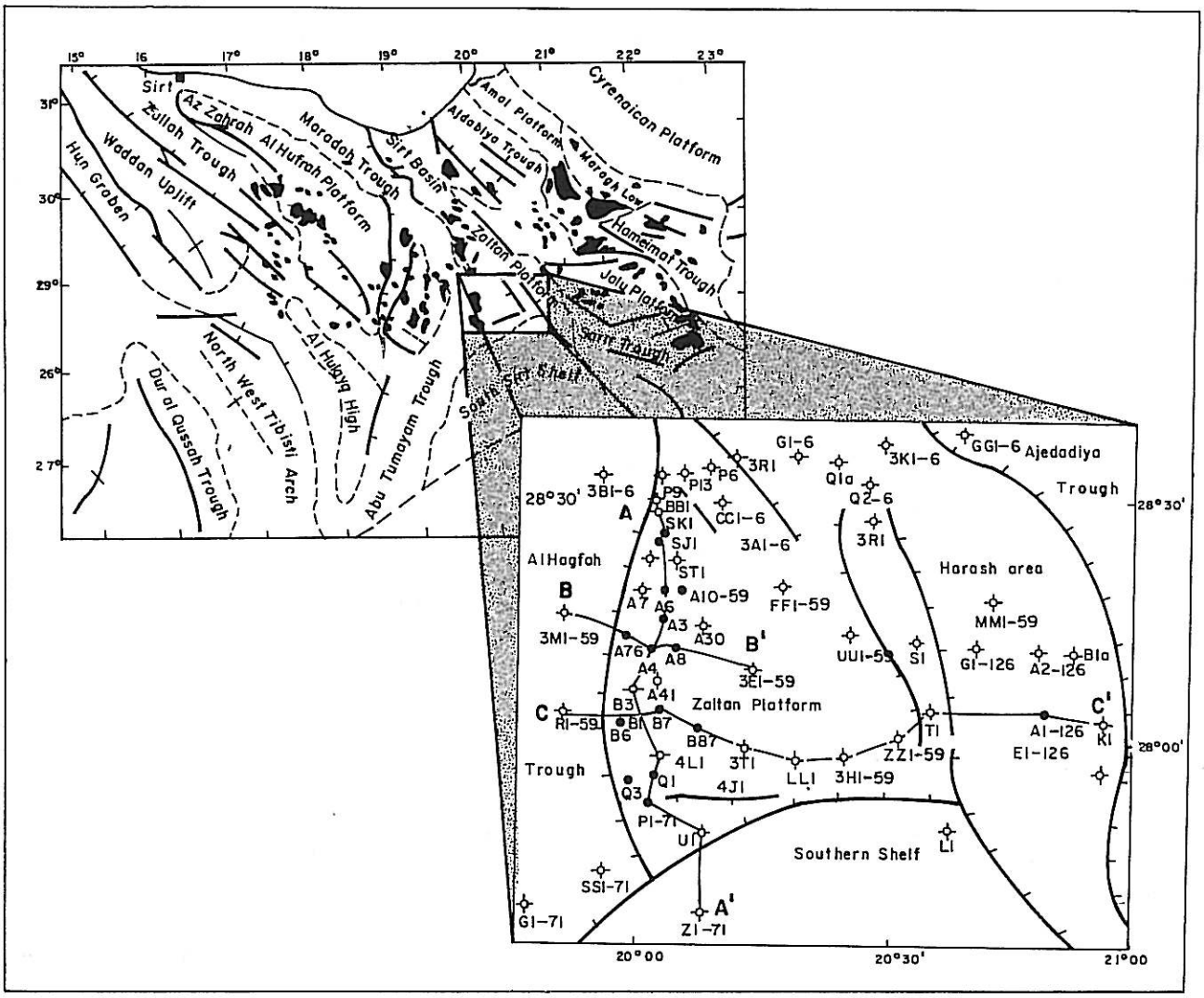


Fig. 1. Map showing the major tectonic elements and location of wells and cross sections in the studied area.

GEOLOGICAL SETTING AND STRATIGRAPHY

The Mesozoic and Tertiary sequences of the Sirt Basin were formed in a tensional regime with large-scale area of uplift and subsidence, associated with normal faulting and a noticeable absence of compressional folds. The absence of Upper Paleozoic and Lower Mesozoic sediments suggests that the area was domed, faulted and eroded during the Late Mesozoic (Lawson, 1988).

The widespread distribution of the Maastrichtian carbonate facies over much of the platform and basin areas suggests that the tectonics were relatively inactive during the Maastrichtian time (Gumati and William, 1985).

In the study area, the Zaltan platform has a NW-SE trend parallel to Al Hagfah trough. It gets wider towards the southern portion of the basin and is tilted down towards the east while the depth of the basement is comparatively deeper to the north (Fig.1).

The geological history of the Sirt Basin, during the Upper Cretaceous period, demonstrates that there has been a gradual onlapping over the fault - block topography by marine sediments. At the very end of the Late Cretaceous, almost all the topographic eminencies were completely buried and shale and carbonates were deposited during the Late Cretaceous time. Abrupt lateral facies changes are apparent from Platform areas toward the deeper troughs along with steep down dip thickening (Fig. 2). Contemporaneous faulting along structural elements and normal step faults probably assisted these conditions.

The regional geological setting and distribution of the Upper Cretaceous sediments is illustrated (Figs. 3 -12). Figures 11,12 and 13 exhibit the relationship between the sedimentary patterns and structural features of the central part of the study area.

PALAEOGEOGRAPHICAL DISTRIBUTIONS AND DEPOSITIONAL HISTORY

Pre-Upper Cretaceous

Nubian Sandstone

The term Nubian Formation or Nubian Sandstone was first applied for a widespread, non-marine sandstone sequence that is well exposed in Nubia, in the Nile Valley of Upper Egypt. Nubian Sandstone was used informally in Libya to cover a broad group of poorly dated detritus sediments representing a major clastic body that had shaped the pattern of distribution and thickness in the study area (Figs.3 and 4). The Nubian Formation in the Sirt Basin was divided into three members namely an upper sandstone member, middle shale and lower sandstone member (Abdulgader, 1996). These continental deposits reach a thickness of more than 800 feet in well P1-71. It unconformably overlies the basement on the eastern - side and south-central part of the Zaltan platform and is absent in the basement palaeohigh of Al Wahah - Ad Deffah ridge (Fig. 4).

Thick sequence of Nubian Sandstone is widespread, over the south and east of Ad Deffah, Al Wahah and Al Harash areas, and extend to the south of Ad Deffah area, which fill a large graben at wells P1-71 and U1-71 (Fig. 4). The Lower and Upper Sandstone members represent fluvial sedimentation that has taken place under regressive conditions

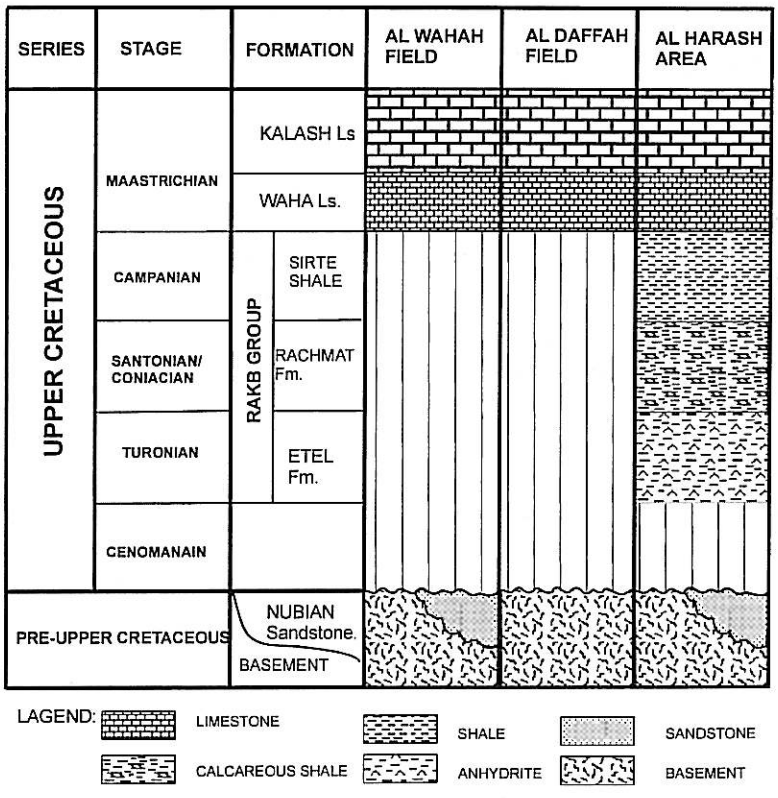


Fig. 2. General stratigraphy of the study area.

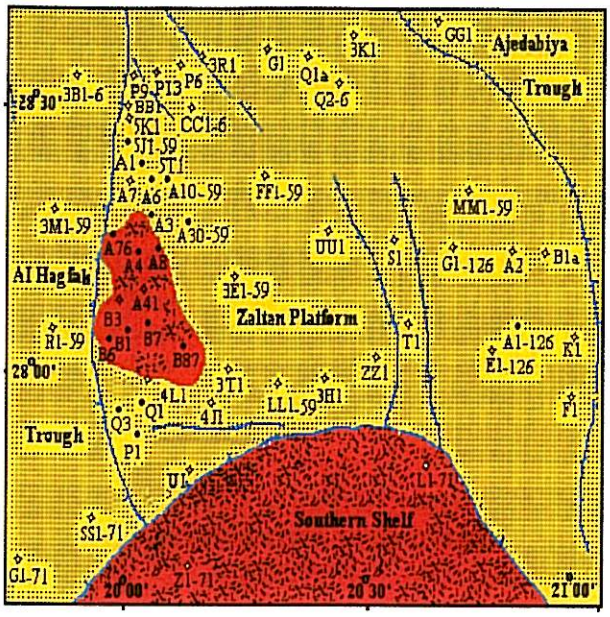


Fig. 3. Palaeogeographic map of pre-Upper Cretaceous sandstone in Zaltan platform.

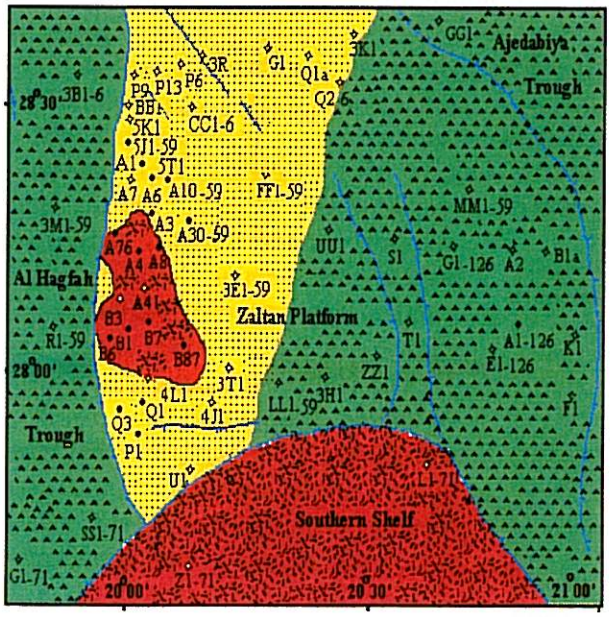


Fig. 4. Palaeogeographic map of Etel Formation in Zaltan platform.

(El-Hawat.1996). On the other hand, Middle Shale Member may represent deposition in lagoon during the time of maximum sea level rise or still- stand stage.

During the Cenomanian time, shallow restricted platform deposits (Lidam Formation) represent the first marine transgression episode that was related to a global rise of sea level and tectonic subsidence. Locally over the central parts this shallow restricted platform deposits onlapped the continental clastic of Nubian Formation.

Upper Cretaceous

Rakb Group

Etel Formation (Turonian Age):

Barr and Weegar (1972) introduced the name and the type section, which is located in the subsurface in well O2-59. The formation is widespread across the study area and its thickness increases gradually from 50 feet at well LL1-59 up to 330 feet at wells U1- 59 and ZZ1-59. It reaches more than 1365 feet at the Al Hagfah and Ajdabiyah troughs, but it is absent on the regionally high areas of Al Wahah and Ad Deffah field areas (Fig. 4). Lithologically it is composed of Anhydrite interbedded with dolomitic limestone, shale and sandstone. The upper contact is placed at the top of the anhydrite below the shale or carbonates of the Rachmat Formation (Fig. 2), which conformably overlies the Etel Formation. In the Zaltan platform, the Etel Formation is transgressive over older formations and unconformable overlies the Nubian Sandstone. It becomes slightly less restricted in the eastern side of the study area where the dolomite rocks are commonly interbedded with anhydrite, southward the Turonian Etel sequence bordered by the basement palaeohighs, is known to geologists as the southern shelf. In general, the Etel Formation is deposited in arid climatic, shallow water restricted platform and subtidal and intertidal with low energy protected environment (Fig. 9).

Rachmat Formation (Santonian / Coniacian)

The Rachmat shale, according to Barr and Weegar (1972), contains Santonian - Coniacian shales and its type section was located in well O2-59. It's thickness in the Zaltan platform ranges between 120 to130 feet in wells ZZ1-59, 3H1 and LL1-59. It gets thicker towards the east in the deep trough area and, is absent on the ridge of Al Wahah and Ad Deffah areas (Fig. 5).

In the study area, the lithology of the Rachmat Formation consists of dark gray green shale with minor limestone, sandstone and occasional dolomite interbeds in the lower part (Barr and Weegar, 1972). The lower boundary is conformable with the Etel Formation and the upper boundary is conformable to disconformble with the Campanian - Maastrichtian Sirte Shale (Fig. 2). The overall distribution of the pre-existing palaeohighs during Santonain-Coniacian time was similar to that of the Turonian time, except

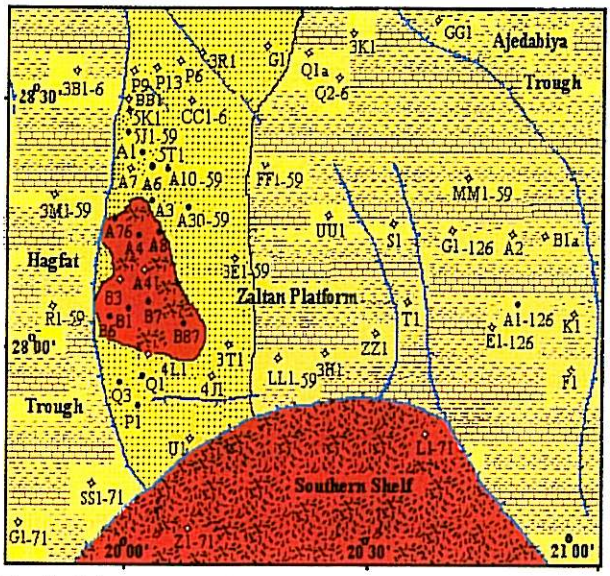


Fig. 5. Palaeogeographic map of Rachmat Formation.

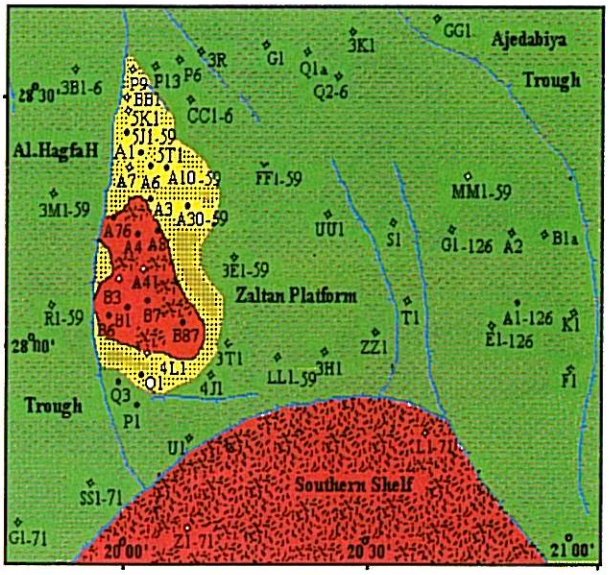


Fig. 6. Palaeogeographic map of Campanian Sirte Shale in Zaltan platform.

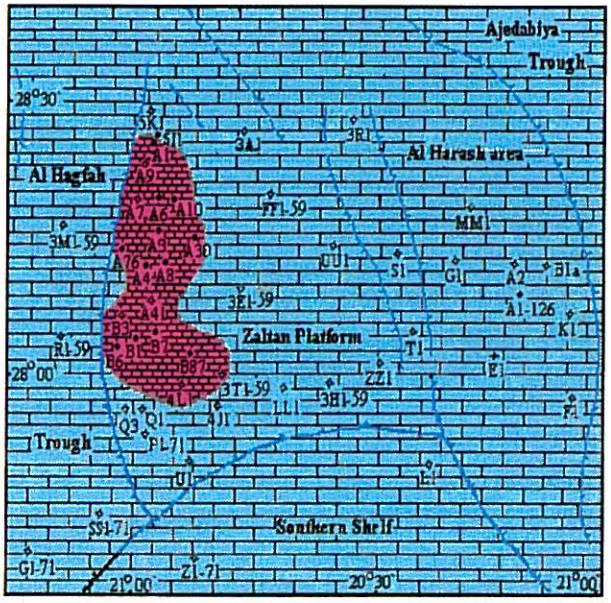


Fig. 7. Palaeogeographic map of Maastrichtian Waha and Kalash formations.

that the Rachmat Formation was deposited in less restricted conditions where carbonate and shale predominated. It is encountered in the wells drilled in the central area of the Zaltan platform and also in Al Hagfah and Ajdabiyah troughs (Fig.10). A gentle gradual thinning westward toward the Al Wahah - Ad Deffah ridge suggests the existence of a gentle slope shelf during the deposition of the Rachmat Formation.

Sirte Shale (Campanian):

The Sirte Shale is dominantly a shale sequence with thin limestone interbeds. It attains an average thickness of about 270 feet and increases towards the eastern part of the Zaltan platform. In the western portion of the study area it is getting gradually thinner towards the regional high of Al Wahah and Ad Deffah field area (Fig. 6). It conformably overlies the Upper Cretaceous (Santonian/Coniacian) Rachmat Formation and in the northeastern part of the study area, the Sirte Shale grades laterally and overlies the Pre- Upper Cretaceous continental sandstone. The upper boundary is conformable with the Maastrichtian Kalash Limestone (Fig. 2). At the close of Santonian and the beginning of Campanian time Al Wahah and Ad Deffah ridge remained subareally exposed separating the Ajdabiyah trough to the east from Al Hagfah trough to the west at an early stage of their subsidence. Widespread gradual transgression extended shale deposition covering the area of study except at the regional highs (Hammuda, 1980).

Shallow restricted environmental setting dominated the whole region of the central basin in the Zaltan platform and deposited thick sequences of Sirte Shale in the Al Hagfah, Ajdabiyah troughs. This shale is interpreted as shallow restricted platform that is characterized by the dominance of dark - grey shale and sandy limestone in the lower part.

Waha and Kalash Limestone (Maastrichtian)

The Waha Limestone exhibits its maximum thickness at well A76-59 along the margin of the Al Wahah and Ad Deffah areas of the Zaltan platform and thins towards the northern and southern parts of the Zaltan platform. In other places it overlies the basement rocks

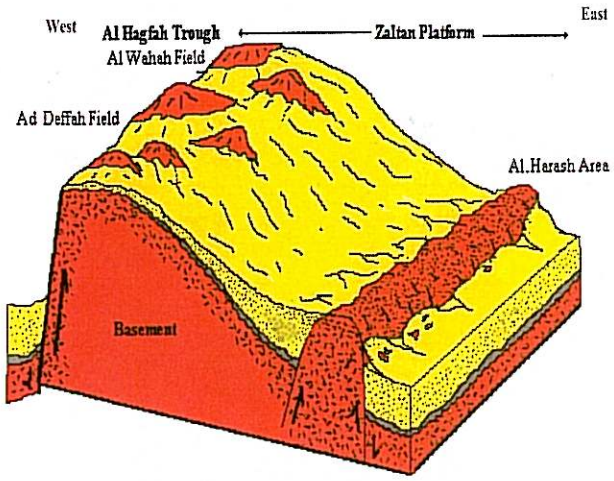


Fig. 8. Depositional model of pre-Upper Cretaceous sandstone (schematic).

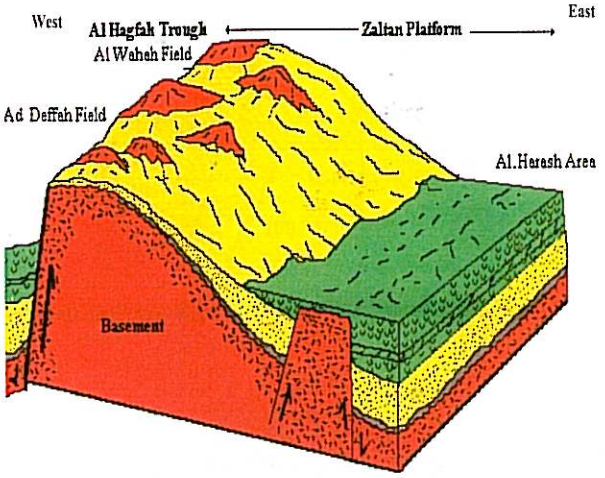


Fig. 9. Depositional model of Turonian Etel Formation (schematic).

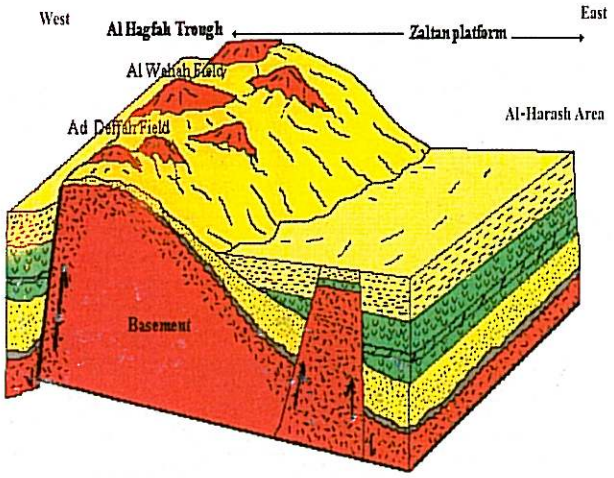


Fig.10. Depositional model of Santonian / Coniacian Rachmat Formation (schematic).

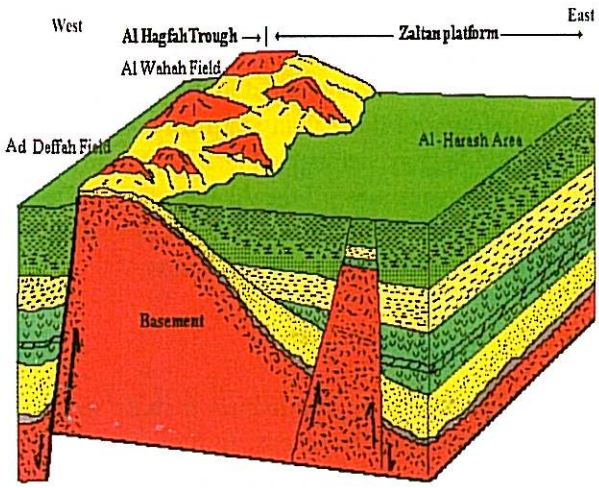


Fig. 11. Depositional model of Campanian Sirte Shale (schematic).

and is conformably overlain by an unusually thinly developed Maastrichtian Kalash Limestone (Figs.13, 15). In Ad Deffah field area, Defa Limestone overlies the Waha Limestone; the latter is underlain by the basement rocks (Fig.13). It ranges in thickness from 145 feet to 200 feet in Ad Deffah field area at wells B1, B2, B7 and B87-59. Widespread distribution of the Maastrichtian Waha carbonate facies over much of the Zaltan Platform and surrounding areas suggests that tectonics were relatively inactive during the Maastrichtian (Hammuda, 1980). (Figs. 7 and 12).

In the southern part of the Zaltan platform, Waha Limestone is the principal reservoir in Al Wahah field (Fig.15). Here it is composed of a skeletal calcarenite onlapping the structurally high area and was subjected to winnowing, creating excellent reservoir conditions. It is restricted to the platform areas because of its shallow - water, high- energy depositional environment. (Wenneker *et al*, 1996).

Kalash Limestone is widely recognized over much of the Sirt Basin and is well defined in its type section at well E1-57. It is conformably overlies the Sirte Shale and Waha Limestone and it is overlain by Paleocene Hagfa Shale or Lower Sabil Carbonates. Abundant foraminifera fauna defined its age and indicated that the kalash Limestone was deposited in an open sea, probably neritic conditions during Maastrichtian age. Because of its widespread distribution it has characteristic signature on the wire line logs. For this reason it was used as the datum line on the top of Kalash Limestone. Towards the south, the Kalash Limestone is distal, more shaly and it onlaps the southern shelf and gradually disappears through non-deposition (Wenneker *et al*, 1996).

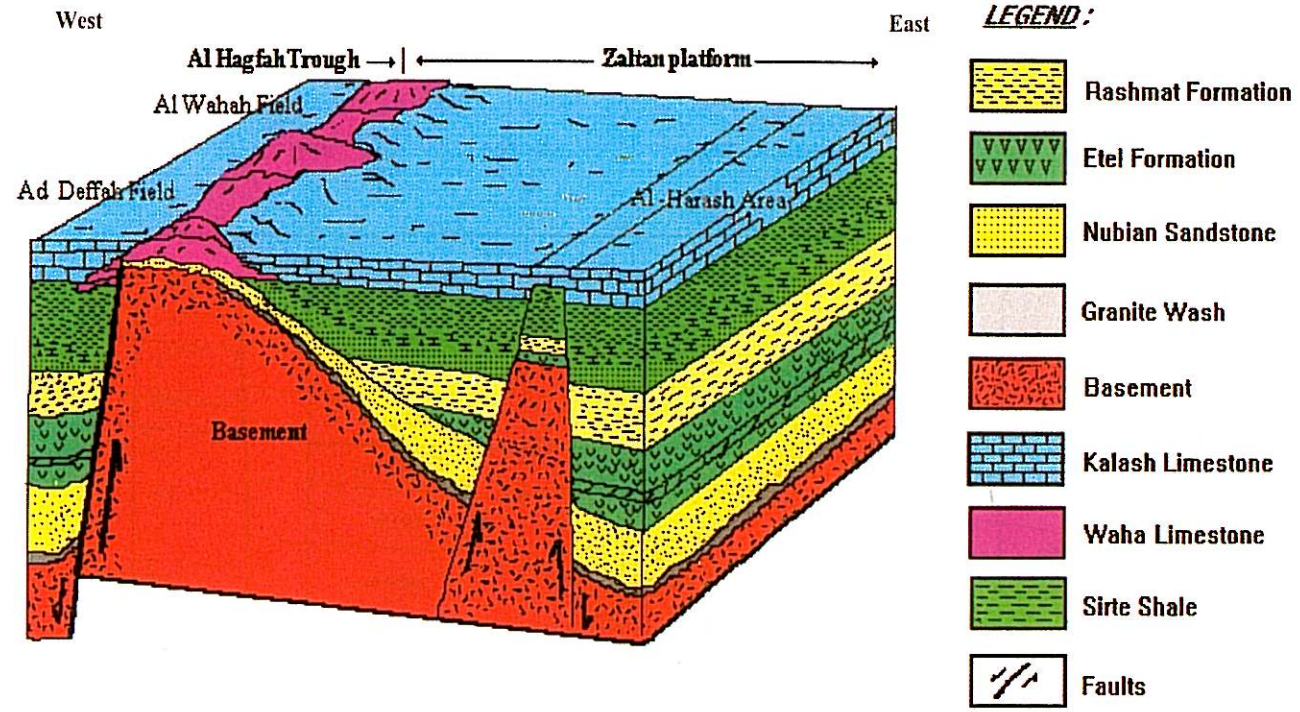


Fig. 12. Depositional model of Maastrichian Waha and Kalash formations (schematic).

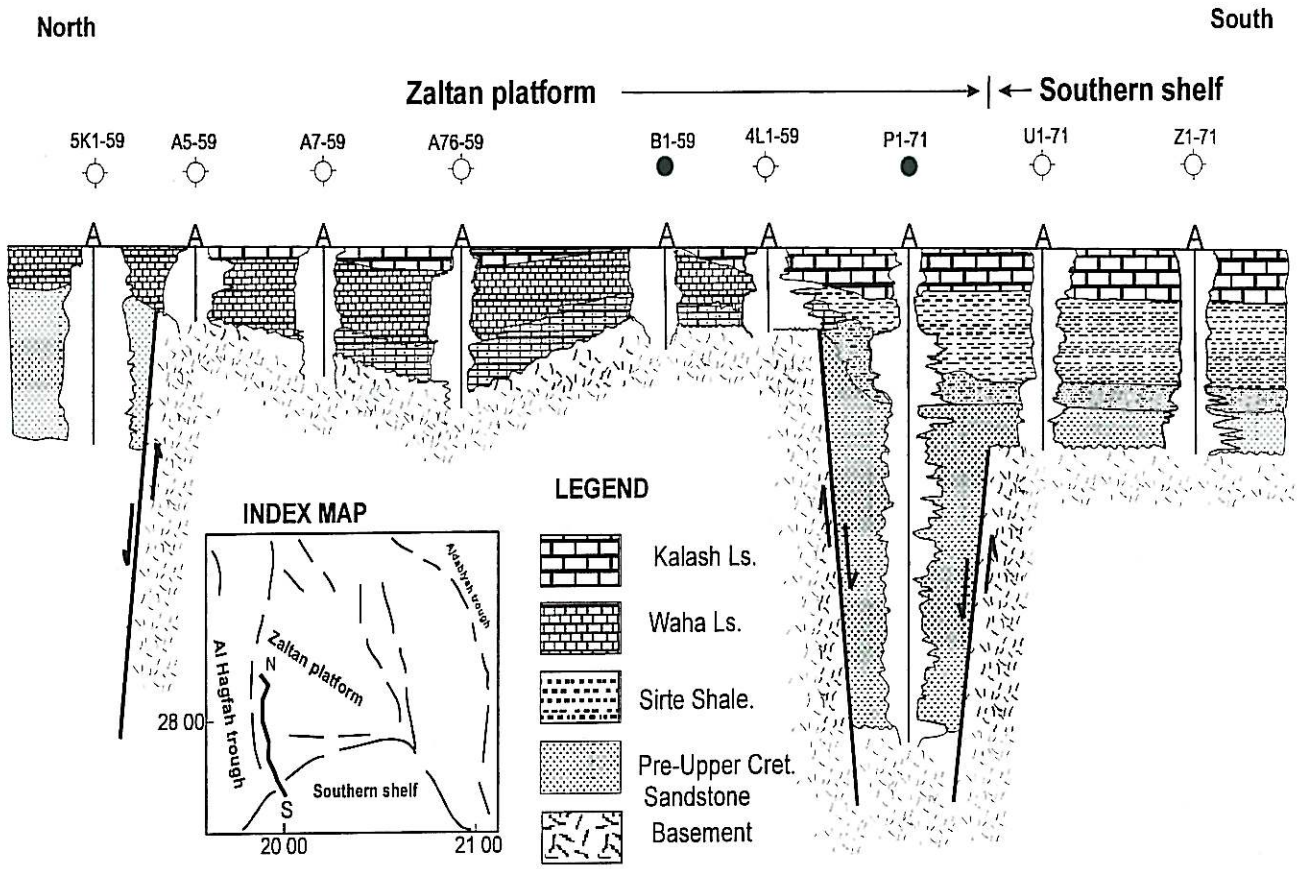


Fig. 13. N-S structural cross-section over Zaltan platform.

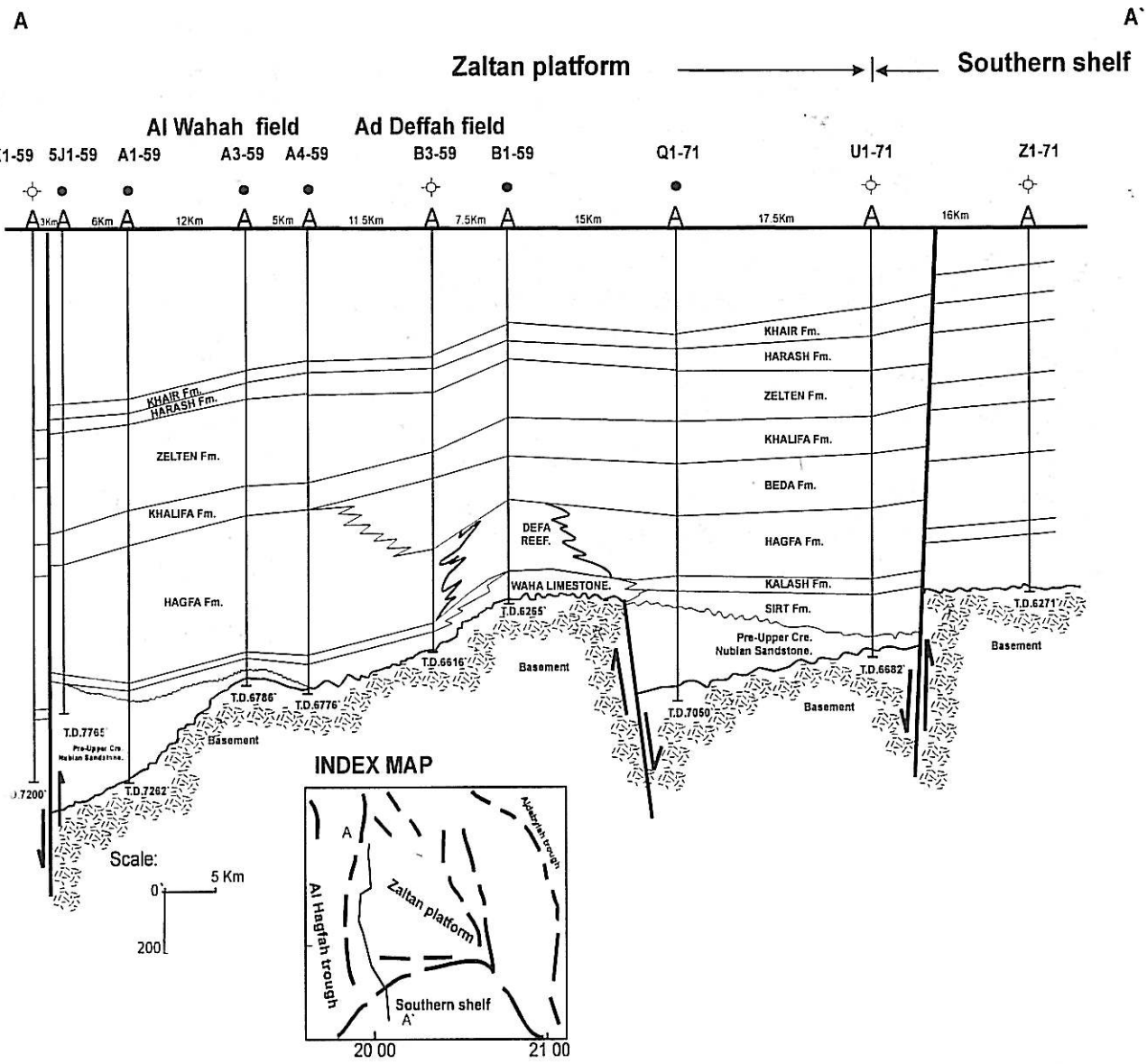


Fig. 14. Cross-section across Al Wahah and Ad Deffah fields, Zaltan platform.

DISCUSSION AND CONCLUSION

The distribution of the lithostratigraphic rock units was related mainly to the palaeogeography of the pre-existing topography. They are: Pre-Upper Cretaceous sandstone, evaporitic Turonian Etel Formation, Coniacian / Santonian Rachmat Formation (shallow open marine, slightly protected). Campanian Sirte Shale (shallow restricted platform). Maastrichtian Waha Limestone (shallow carbonate platform). The Paleocene and Eocene sequences comprise Hagfa Shale, Beda and Khalifa formations, Zeltan Limestone, Harash and Khier formations.

Shales and carbonates were deposited during all stages of the Upper Cretaceous as a lateral time equivalent facies. It was developed in the western palaeotopography high of the Zaltan Platform area towards the deeper trough, east of the Harash area. Contemporaneous faulting assisted the thickening.

During the Upper Cretaceous time southward advancing seas, encroached gradually on the Al Wahah and Ad Deffah areas which remained emergent until the end of Early Campanian time.

At the close of Santonian stage, the Zaltan platform remained subaerialy exposed separating the Ajdabiyah trough to the east from the Al Hagfah trough to the west at an early stage of their subsidence. The area of Al Wahah and Ad Deffah fields existed at this time as an island or peninsulas surrounded by Pre-Upper Cretaceous sandstone (Nubian Sandstone) which was

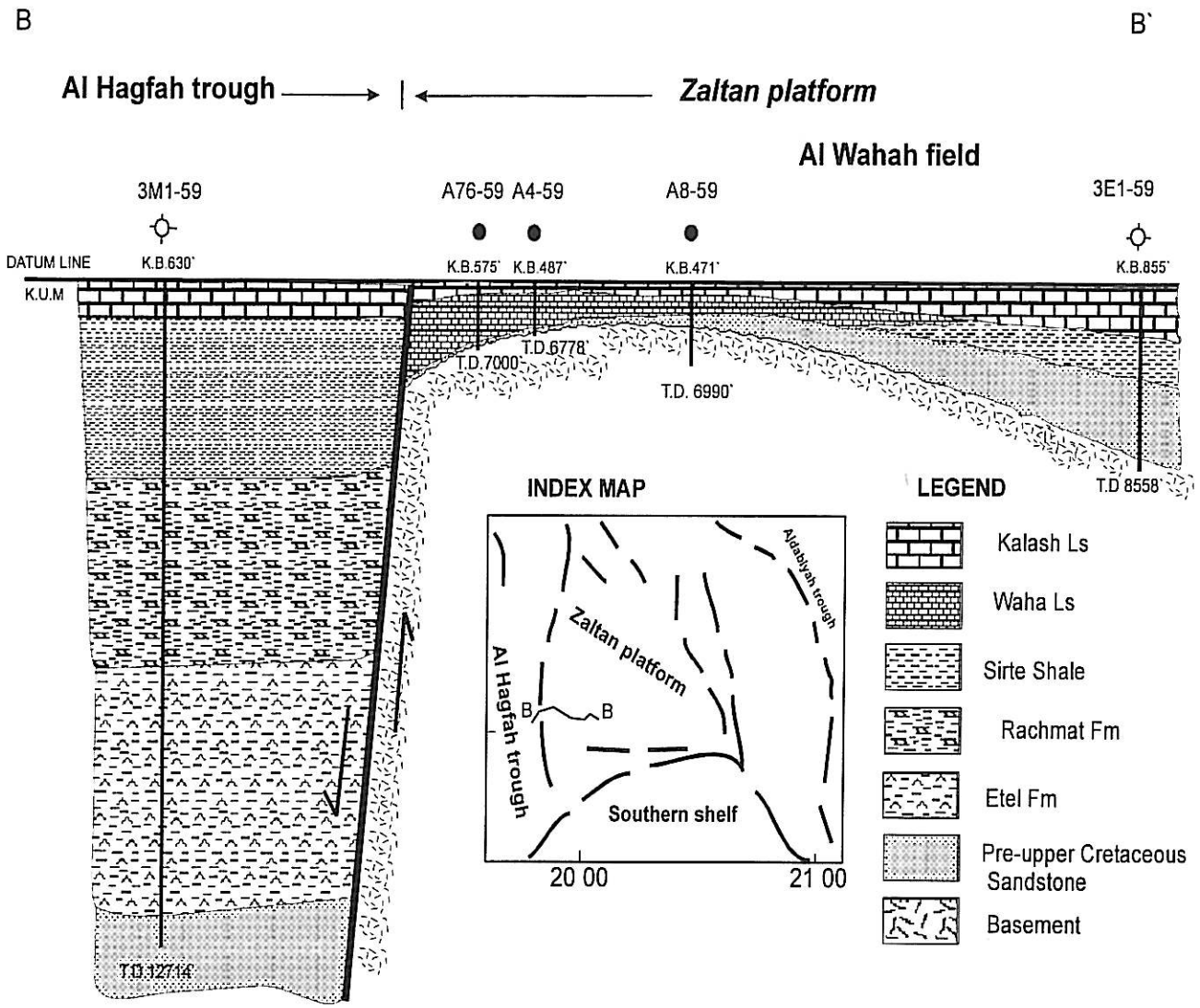


Fig. 15. Cross-section across Al Wahah field, Zaltan platform.

deposited east of Ad Deffah-Al Wahah area and south of Ad Deffah field. Furthermore, seas advanced toward the south at the Early Campanian stage resulted in a sea connection between Ajdabiyah and Al Hagfah troughs.

During Late Campanian and Early Maastrichtian times seas transgressed over Ad Deffah - Al Wahah ridge and reworked pre-existing sands from high areas and redeposited them as marine shoreline calcareous sands.

During Maastrichtian time the sea continued to transgress southwards onto the peninsula until Al Wahah ridge was separated from Ad Deffah ridge forming two separate islands, while the carbonate belts around them grew narrower as the sea got too deep for carbonate precipitation. Rudist carbonate facies developed on the highs. These deposits are well known as Waha reservoir facies in this area.

ACKNOWLEDGEMENT

We would like to express our deep appreciation to the General Manager of the Petroleum Research Centre for his support, and also thank Prof. Busrewil and Prof. A. Sbeta for their constructive remarks and valuable comments. Our thanks are extended to all members of the Exploration Research Department for their help during the preparation of this work.

REFERENCES

Abdulgader. G, 1996. Sedimentology and reservoir heterogeneities of the Nubian Formation, south eastern Sirt Basin, Libya. In: *Geology of Sirt Basin*, **II**. 223- 249. Elsevier, Amsterdam.

El Hawat, Ahmed. S ,1996. The Nubian sandstone in Sirt Basin and its correlatives. In: *Geology of Sirt Basin*, **II**. 3 - 30. Elsevier, Amsterdam.

Barr. F. T and Weegar, A, 1972. *Stratigraphic Nomenclature of the Sirte Basin, Libya.* Publication of Petroleum Exploration Soc. Tripoli, Libya, P.179

Bergig. K. A ,1991. *Al Wahah Oil Field, Case History.* Unpublished report, *Petroleum Research Centre*, Tripoli, Libya.

Butt. A. A, 1986. Upper Cretaceous biostratigraphy of the Sirt Basin, Libya. *Revue de paleobiolgie,* **5**(2) 175-191.

Gumati Y. D. and William. H, 1985. Early Tertiary subsidence and sedimentary facies - northern Sirte basin, Libya. *Am. Assoc. Petrol. Geol.* **69** No.1. 39- 52.

Hammuda. O. S, 1980. Sediments and palaeogeography of the Lower Campanian sand bodies along the southern tip of Ad Deffah -Al Wahah, Sirt Basin. *In: Symposium on the Geology of Libya* Tripoli, Libya, 509-520, London Academic Press.

Lawson. W. G, 1988. *Progress Report On North Al Wahah And Al Wahah Field Areas*, (internal report), *Waha Oil Company,* Libya. 23 p.

Wennekers J. H, Wallace F. K. and Abugares. Y. I. 1996. The geology and hydrocarbon of the Sirt Basin: *Synopsis. In: Geology Sirt Basin.* **II**, 3–56, Elsevier, Amsterdam.

Petroleum Res. J. Vol. 15 (2003): P. 33–48, 6 Figs.

Petrography of the Uppermost Bahi Formation in the West Az Zahrah (B) Field, Az Zahrah - Al Hufrah Platform, NW Sirt Basin, Libya

Muftah Ahmid*

بتروغرافية الجزء العلوي من تكوين الباهي بالمنطقة الغربية من حقل الظهرة (ب) بشمال غرب حوض سرت، ليبيا

مفتاح أحمد

يتراوح عمر تكوين الباهي بين المرحلة السينومانية والمرحلة الماسترختية، حيث تتواجد صخور هذا التكوين تحت السطح بمسطح الظهرة – الحفرة، بالجزء الغربي من حوض سرت. ترسب تكوين الباهي فوق تكوين الحفرة (القرقاف)، ويتناقص سمكه تدريجياً حتى يختفي فوق منطقة مرتفع الظهرة. أوضحت دراسة العينات اللبية وجود طبقات رملية متداخلة مع طبقات من طين ووجود بعض الرقائق الدولوماتية في بعض الأجزاء. يتميز أعلى الجزء العلوي من تكوين الباهي بكثرة وجود معدن الجلوكونايت وبمتوسط سمك يصل إلى 30 قدم (9 أمتار) مما يدعم تأثير الترسيب البحري في المنطقة.

بينت الإختبارات البتروغرافية أن هذه الصخور تتكون أساساً من حبيبات من معدن المرو وبمتوسط نسبة حجميه تصل إلى 76% كما يوجد معدن الفلدسبار بنسبة تصل إلى 22%، معظمها من النوع القلوي (أوثوكليس وميكروكلاين)، ونسبة أقل من بلاجوكليس (أوليوكلاس)، بينما يمثل الفتات الصخري ما نسبته 1.6% تقريباً من المكونات الأساسية للصخر، ونتيجة لذلك يمكن أن يصنف أعلى الجزء العلوي من تكوين الباهي بتحت رتبة الأركوزك إلى أركوزك. أما المعادن الثانوية المتمثلة في المايكا والبايرايت وأكاسيد الحيد والزركون والترمالين والروتايل والإلمانيت فتوجد بنسبة حجمية ضئيلة جداً.

توجد عدة أنواع من المعادن الطينية مثل: الكاولونايت، إلاّيت والكلورايت، هذه بالإضافة إلى بعض المعادن اللاحمة مثل: الدولومايت والكالسايت والإنهيدرايت. وتسبب تواجد المعادن الطينية واللاحمة بين الحبيبات الرملية في تغير ملحوظ في مسامية الصخور موضع الدراسة.

Abstract : *The Bahi Formation is diachronous in age, range from Cenomanian to Maastrichtian, and occurs in the subsurface of the Az Zahrah – Al Hufrah Platform in the western part of the Sirt Basin. The Bahi Formation onlapping the Al Hufrah Formation /Gargaf Formation and wedged out against the Az Zahrah Palaeo-high area. The core samples from the studied wells record mainly sandstones units interbeded with shales and thin layers of dolomites in some parts. The uppermost portion of the formation is characterised by abundant glauconite, suggestive of a marine influence with an average thickness of about 30 feet (9 m). Petrographic* investigation *shows that the rock compositions of the uppermost Bahi Formation are mainly quartz with an average of 76%; feldspars make up to 22% mostly potassium feldspar (orthoclase and microcline) and minor*

*Petroleum Research Centre, P. O. Box 4631, Tripoli, Libya.
E-mail: akhmuftah@yahoo.com

plagioclase (oligoclase) and rock fragments. The latter represent only 1.6% of the total rock framework composition, as a result the uppermost Bahi Formation is classified as subarkose to arkosic-arenites. Accessory minerals such as pyrite, mica, iron oxides, zircon tourmaline, rutile, ilmenite and apatite are present in a minor amount. Presence of several kinds of clay minerals such as kaolinite, illite, and chlorite, in additional to, other cements such as dolomite, calcite and anhydrite, forming and growing of these minerals in-between sand grains, caused a noticeable changes in the porosity of the studied part from the formation.

INTRODUCTION

The Bahi Formation is present in the subsurface of the northwestern margin of the Az Zahrah - Al Hufrah region. The formation consists of sandstones interbedded with shale and with thin laminae of dolomite in some intervals. It is unconformably underlain by Lower Palaeozoic quartzitic sandstone and in some areas by basement rocks. The formation is diachronous with Cretaceous sediments and in-turn overlain with the Late Cretaceous marine sediments or Tertiary sediments in some areas. The Bahi Formation is equivalent to a number of formations, Maragh Formation in Amal platform and Basal Upper Cretaceous sandstone in the Hameimat trough east of Sirt Basin. The formation age, ranges from Cenomanian to Maastrichtian (Baird, 1964). Barr and Weegar, (1972) studied the stratigraphy of the Bahi Formation in the Bahi oilfield and subdivided it into upper and lower units. The uppermost part of the upper unit is dominated by glauconite, which indicates marine environment. They have recorded, that the Bahi Formation deposits vary in thickness from a few feet to more than 400 feet, and are comprised of inter-bedded sandstones, siltstones, shales and conglomerate. Later work by Sghair, (1990 and 1996), presented a detailed petrographic description of the Bahi Formation in the Az Zahrah - Al Hufrah region, particularly in the Bahi field, and classified the Bahi Formation as subarkosic sandstone, cemented with carbonate and anhydrite and proposed that it was derived from reworking of craton basement and recycled sediments. All previously mentioned authors concluded that the formation is diachronous in age, and its bulk, initially, was as an alluvial and fluvial deposits, which passes into marine-influenced sediments in its uppermost part.

The area of study extends between Az Zahrah Palaeo-high at Az Zahrah "B" field to the east and Zallah trough to the west (Fig.1). Core samples were selected from the six bore holes: JJ1-32, Q1-32, LL1-32, FF1-32, II1-32 and MM1-32 (Table 1).

Detailed petrographical study for the uppermost Bahi Formation in the study area is presented. Several petrographical techniques are applied in studying the selected samples and polished thin sections, such as binocular and polarizing microscope examination, scanning electronic microscopy (SEM). The percentage of component minerals for each thin section was calculated using an automatic point counter. As a result, rock framework minerals, porosity, matrix and cement amounts and types were determined. Percentage contents are expressed in terms of total rock composition (TRC), and total rock framework grains (TRFW).

Table 1. Data base of the study wells; formation thickness, core lengths and number of samples of the uppermost Bahi Formation.

Well name	Subsea depth Bahi Fm	Thickness in ft.	Core length	Samples *
JJ1-32	-3740' to -3931'	191' (58 m)	10.5' (3.2m)	5
Q1-32	-3735' to -3870'	135' (41 m)	21' (6.5 m)	10
LL1-32	-3725' to -3930'	205' (62.5m)	15' (4.6 m)	8
FF1-32	-3723' to -3895'	172' (52.5m)	33' (10.0 m)	13
II1-32	-3777' to -3866'	89' (27.0 m)	35' (10.7 m)	13
MM1-32	-3768' to -3851'	83' (25.3 m)	30' (9.1 m)	11
* The total samples include; 2 samples dolomite and 2 samples shale from FF1 and LL1, and one shale sample from JJ1-32.				60

Geological Setting of the Bahi Formation

The Bahi Formation was penetrated in Concession 32 in the Bahi field area and some parts of the Az Zahrah region, in the northwestern part of the Sirt Basin on high structural area called the Az Zahrah – Al Hufrah Platform. The concession is topographically higher than the surrounding areas that border it to both west southwest and east northeast; the subsurface strata also show thin stratigraphic sections and shallow depths to basement relative to those preserved on both adjacent down thrown sides, the Zallah trough to

the west southwest and the Maradah trough to the east northeast (Fig. 1).

The thickness of the Bahi Formation varies from a few feet to 400 feet (122 m). in the Bahi field area, and is about 200 feet (61 m) thick in the south western corner of the Concession -32, at the wells LL1 and FF1-32. It wedges out against the Az Zahrah Palaeo-high to the east at well B1-32 and B2-32 where the Bahi Formation was absent due to non-deposition or to exposing the region to strong erosional events (Figs. 2 and 3). As a result the formation is diachronous and is both overlain by/or equivalent to sediments ranging in ages from Cenomanian to Maastrichtian, or may be younger in some parts (Fig. 4).

PETROGRAPHY OF THE UPPERMOST BAHI FORMATION

General Lithology Description

The uppermost Bahi Formation sandstones are: whitish, grey, to light greenish in colour in hand specimen. They are fine to medium, occasionally coarse in grain size; sub-rounded to sub-angular, occasionally rounded or elongate-shaped grains; moderately to well sorted, but locally poorly sorted. They are moderate to well indurated. Some horizons display oriented grains, which may reflect the direction of flow during deposition. Clay-rich and carbonate-cemented units show random grain orientation with lack of primary porosity. The uppermost part of the sandstone units are thicker, coarser and highly porous with less interstitial clay.

The dominant mineral is quartz followed by feldspar with only minor amounts of rock fragments and micas. Phosphatic fragments and glauconite grains are also present in very small amounts at the upper contact boundary and sparsely within some clay-rich samples, but they are absent in the cleaner sandstone units.

Rock Framework Minerals Composition

Quartz

Both monocrystalline and polycrystalline quartz grains are present throughout the formation.

Monocrystalline quartz: is the most abundant framework mineral in the studied samples of the

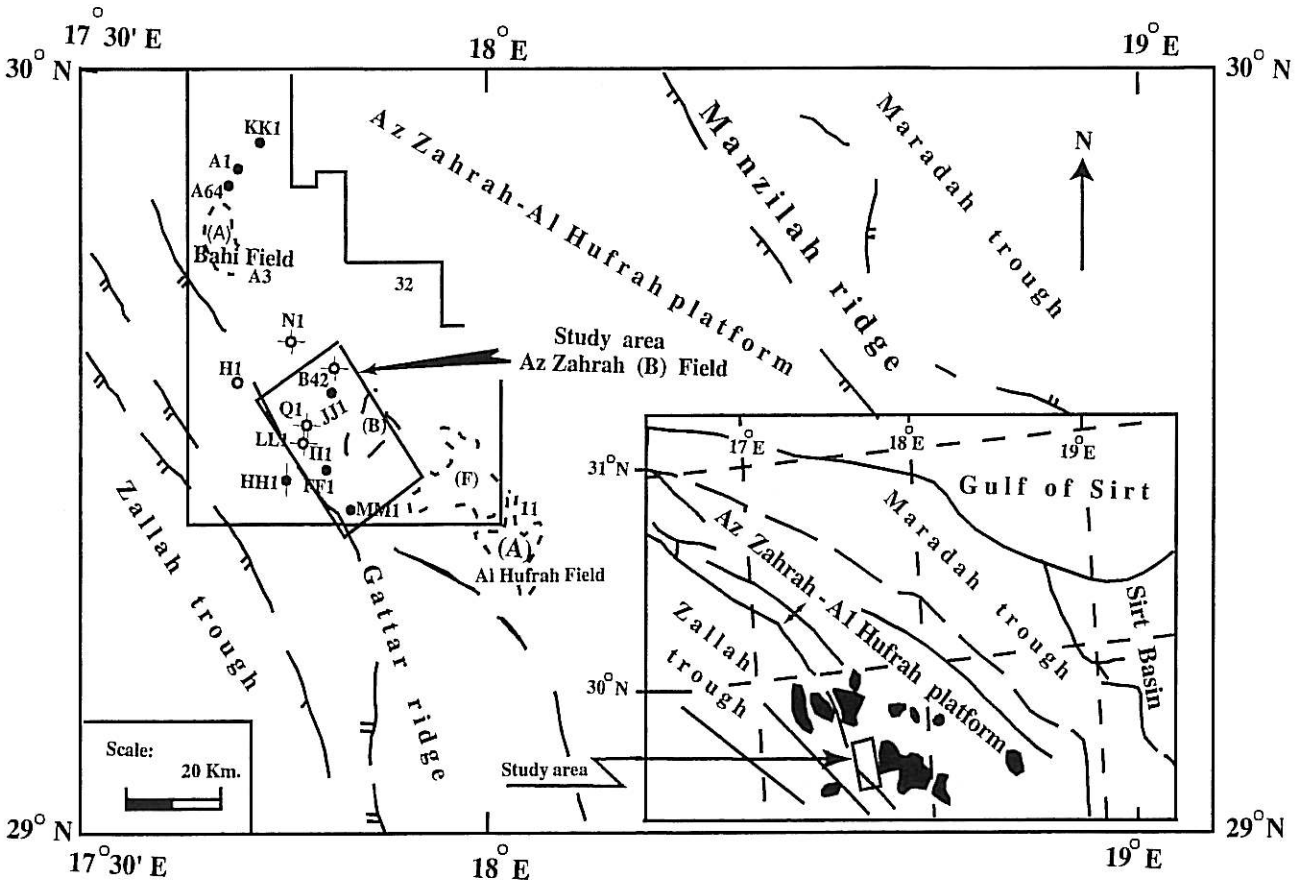


Fig.1. Shows the structural boundaries of the Az Zahrah-Al Hufrah platform and the location of the study area.

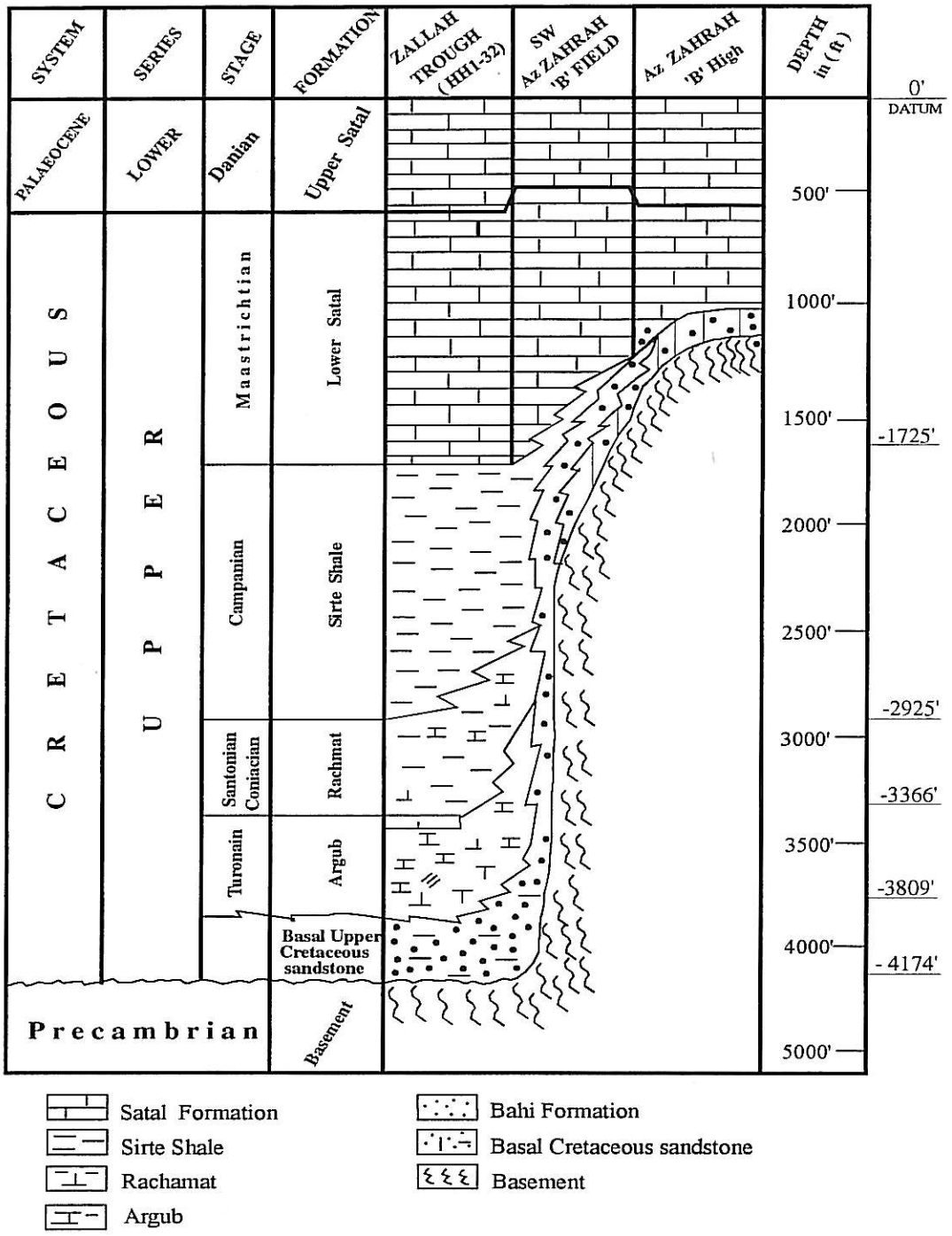


Fig. 2. Shows the correlation between the srtatigraphic columns of the Zallah trough (HH1-32), the SW Az Zahrah (B) field and the Az Zahrah palaeo-high at (B) field.

uppermost Bahi Formation. Table 2, shows the percentage range in each well and indicates that the average percent of total quartz ranges between 68.4 to 81.7%, with an average of 73.4% of the total framework. The grains typically display weak undulosity with rare grains that are moderately undulose. Straight extinction is also rare. Grains commonly contain trails of vacuoles and occasionally microlith inclusions of tourmaline and rutile.

Polycrystalline quartz: is present in the studied samples in minor content only making up 0.87 to 3.2% of the total rock composition with an average of 1.47% (Table 3). The uppermost Bahi Formation is characterized by fine to medium, occasionally coarse polycrystalline quartz. With increase in grain size the percentage of the polycrystalline quartz also increases, ranging from 4.99% of total framework grains in the coarse to

Table 2. Distribution of monocrystalline quartz (Qm) in the various wells (TRC; total rock composition. TRFW; total rock framework).

Well name	Qm % range (TRC)	Aver. (TRC)	Qm % range (TRFW)	Aver. (TRFW)
JJ1-32	47.7 to 55.7	52	73.72 to 87.03	81.7
Q1-32	20.7 to 61	43.3	58.46 to 87.71	75.42
LL1-32	33 to 41.7	37.1	63.64 to 74.86	68.44
II1-32	37.3 to 53.3	46.3	61.39 to 83.56	73.87
FF1-32	37 to 44	39.5	62.08 to 76.14	66.43
MM1-32	33 to 52	43.3	61.97 to 82.14	74.52
Aver. all	34.8 to 51.1	43.6	63.54 to 81.99	73.40

Table 3. Shows distribution of the polycrystalline in comparison with grain size (TRFW; total rock framework. TRC; total rock composition).

Well name	Grain size	Q Poly % (TRFW)	Q Poly % (TRC)	Chert % in (TRC)
JJ1-32	C to VC	4.99	3.2	0.3
Q1-32	C to V (CF-VF)	2.50.73	0.87	0.3
LL1-32	F-M	1.46	0.95	0.4
II1-32	F-V (FM-C)	1.182.9	1.19	0.13
FF1-32	F-M	2.37	1.36	0.1
MM1-32	F-VF (F-m)	1.381.17	0.73	0.2
Average		3.11	1.47	0.9

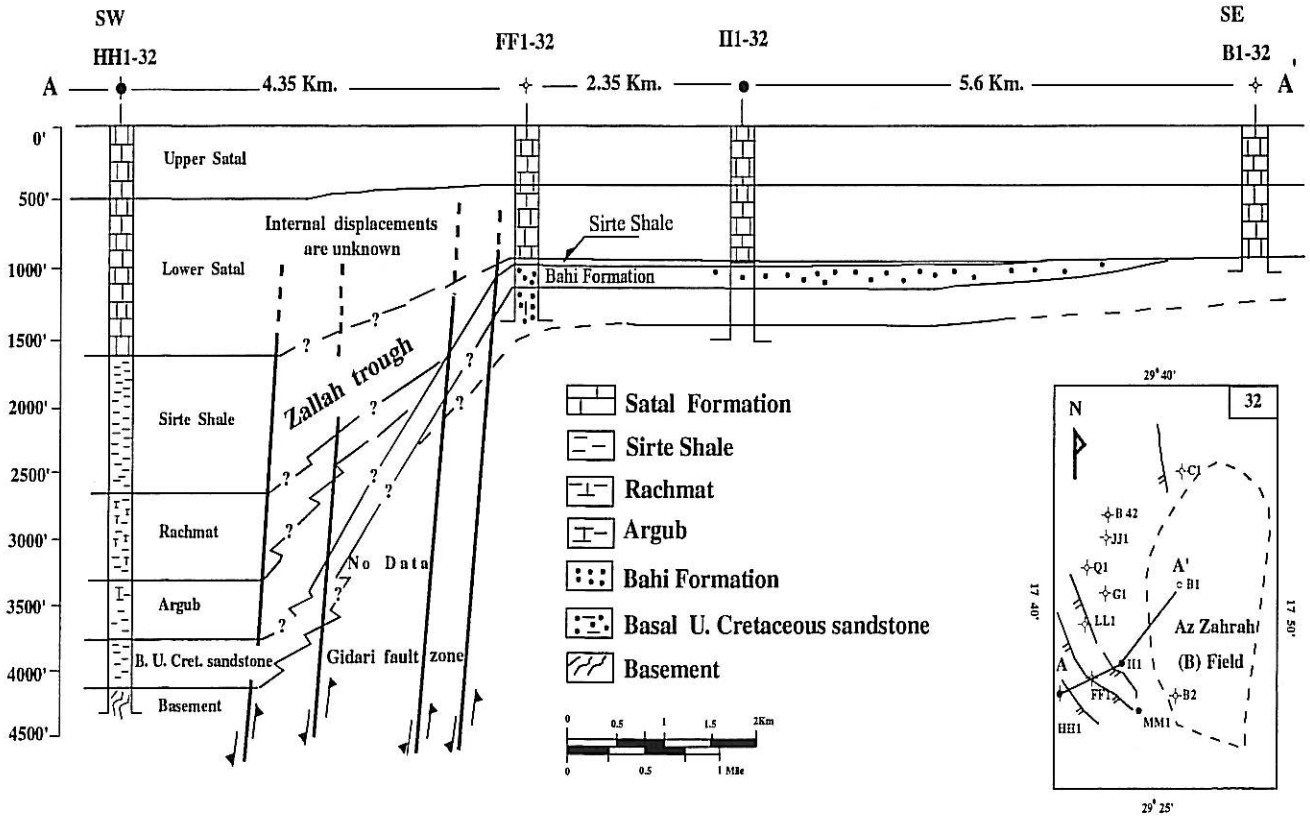


Fig. 3. Geological cross-section A A2 across the Zallah trough (HH1-32), the west of the Az Zahah (B) field (FF1-32 and II1-32) and the Az Zahrah palaeo-high (B1-32), indicates wedging out of the Bahi Formation against the Az Zahrah palaeo-high.

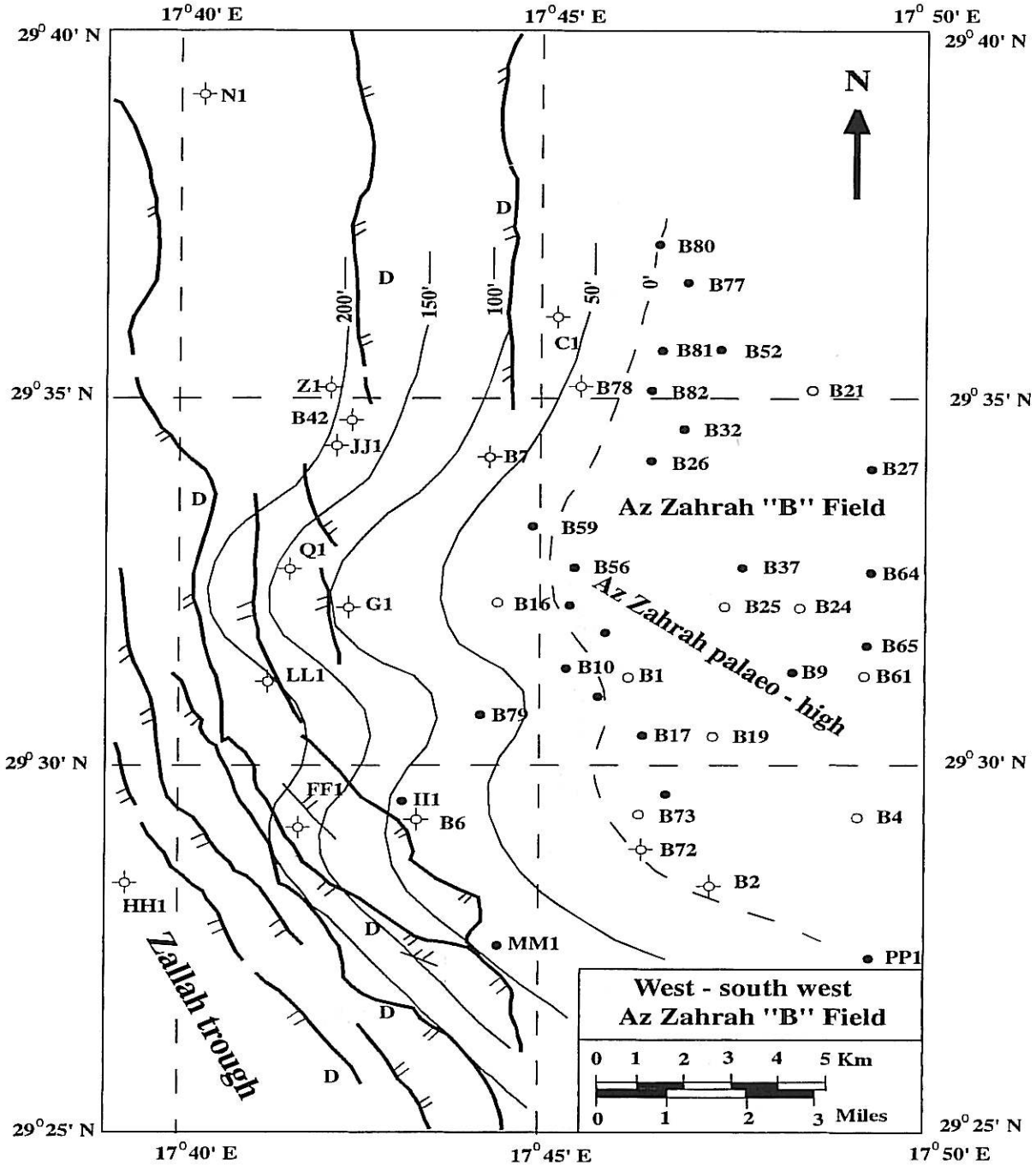


Fig. 4. Isopach map of the Bahi Formation western Sirt Basin, showing the wedging out of the formation against the Az Zahrah palaeo-high.

very coarse sands (JJ1-32), down to 1.17% in the finer sands (MM1-32).

Feldspars

The uppermost Bahi Formation framework mineral counts indicate that feldspar shows variation in amount, which is the inverse of the quartz content (Table 4) reflecting the fact that these are the two dominant minerals in the sandstones.

The average percentage of the total feldspars in the different wells of the total framework ranges between 11.48% in JJ1 to 30.37 % in FF1-32, with an average of 22.318%, (Table 4). Variation in feldspar content may be related to variation in grain size, percentage of primary cement and development of secondary porosity. At the same time, back-scattered electron image analysis shows that the percentage of the feldspar present is often higher than that established using point counting with the

Table 4. The uppermost Bahi Formation framework grains in percent, (total quartz; Qt, total feldspar; Ft, and total rock fragments; Lt).

Well name	Average % of Qt in (TRFW)	Average % of Ft in (TRFW)	Average% of Lt in (TRFW)	General classification
JJ1-32	87.08	11.48	1.45	sub-arkosic arenites
Q1-32	77.96	18.79	3.25	sub-arkosic arenites
LL1-32	70.82	28.18	0.99	arkosic arenites
II1-32	75.9	22.13	1.97	sub-arkosic arenites
FF1-32	68.65	30.37	0.98	arkosic arenites
MM1-32	76.16	22.96	0.88	sub-arkosic arenites
Average	76.096	22.318	1.586	sub-arkosic arenites

petrological microscope. This can be as high as 20 to 30% more in some samples. In fact it is possible that most of the samples are arkosic rather than subarkose according to the classification by (Pettijohn *et al.,* 1987). This highlights the difficulty experienced in identifying some of the feldspars, particularly unaltered orthoclase, which can be mistaken for quartz, and micro-size grains, which may be too small to count.

Plagioclase: is found in all samples in small amounts (Plate I -1); with average range of 0.6 to 1.7% of total rock volume.

Potassium Feldspar: is more chemically stable than plagioclase, and the most abundant feldspars, consist mainly of microcline and orthoclase (Plate I-2). The average percentage of potassium feldspar ranges from 6.03 to 17.03% of total rock volume.

Perthite: is also present, some of the perthite-*sensu stricto* the lamellae are well defined (Plate I-3) whereas in the authigenic form the albite lamellae tend to be much more irregular and often grade into discrete patches or crystals of albite (Plate I-4). It is considered that the detrital perthite is rare in the samples whereas the authigenic form occurs in all cored intervals. Even so, the average percentage per rock volume in the studied samples is very low, and ranges from 0.18 to 0.37% of total rock volume.

Rock Fragments

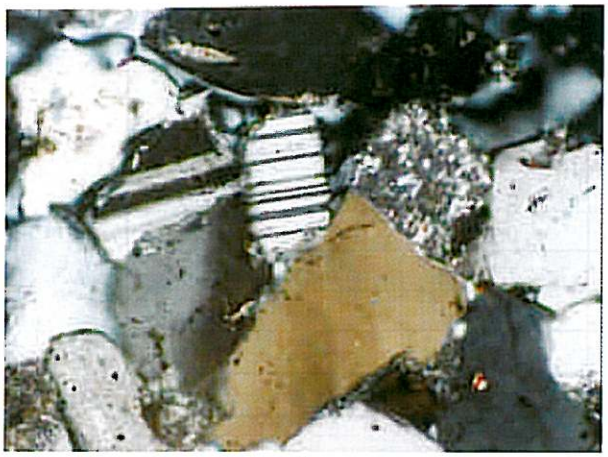
The rock fragments form only a small proportion, ranging between 0.49% to 1.96% with average of 0.97% of total rock volume, and between 0.49% to 3.25%, with average of 1.59% of total rock framework (Table 5).

The abundance of the rock fragments is clearly related to grain size; the coarse-grained sandstones contain more lithic fragments than the fine-grained sediments in which the fragments have been broken down to their individual components. The most common rock fragments are quartz grains with inclusions of stable non-opaque minerals such as tourmaline, zircon and rutile. These fragments could be igneous or metamorphic. The estimated percentage of this lithic type is about 40% of the total average of rock fragments.

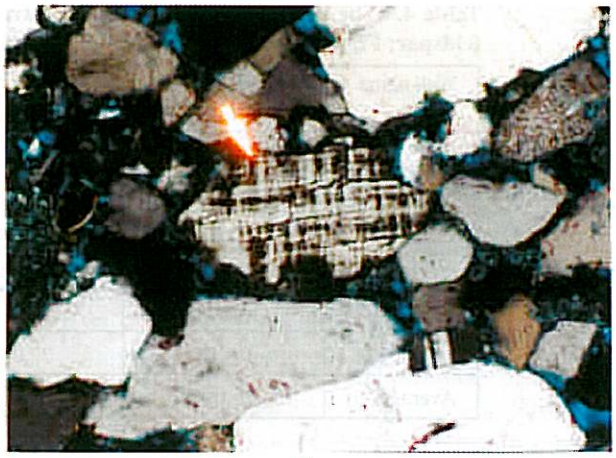
Metamorphic Fragments: Polycrystalline quartz aggregates are fine to medium- grained and rarely coarse in size and display sutured,

Table 5. Framework percentage of samples in the study wells, (Qm; monocrystalline quartz, Ft; total feldspar, Lt; total rock fragments, L; rock fragments; igneous, metamorphic and sedimentary).

Well name	Qm % range (TRFW)	Ft % range (TRFW)	Lt % range (TRFW)	Aver. L % (TRC)	Aver. L % (TRFW)
JJ1-32	73.72 - 87.03%	7.09 - 19.63%	4.07 - 8.9%	0.93%	1.45%
Q1-32	58.46.- 87.71%	8.05 - 37.54%	1.16 - 11.44%	1.96%	3.25%
LL1-32	63.64 - 74.86%	20.29 - 33.27%	1.89 - 4.85%	0.55%	0.99%
II1-32	60.75.- 83.56%	10.17 - 35.05%	1.25 - 9.05%	1.26%	1.97%
FF1-32	53.66 - 76.14%	21.87 - 34.56%	1.04 - 5.97%	0.6%	0.98%
MM1	61.97 - 82.64%	16.5 - 35.06%	1.4 - 4.57%	0.49%	0.88%
Average	73.40%	20.73%	3.68%	0.97%	1.59%



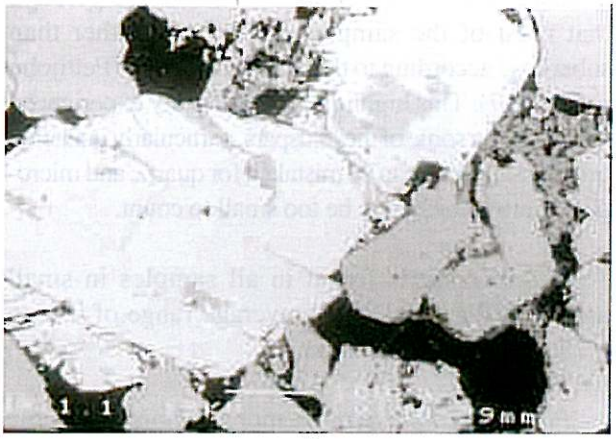
1



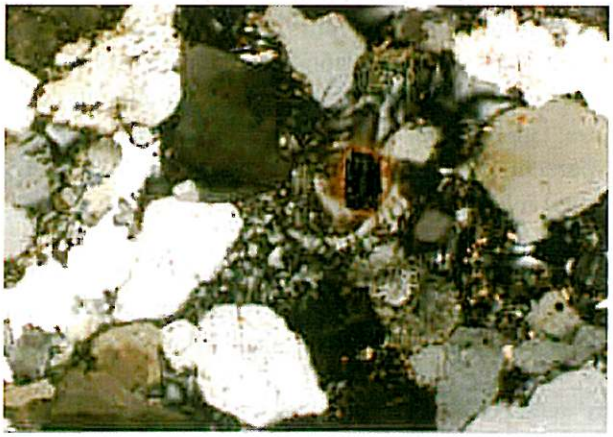
2



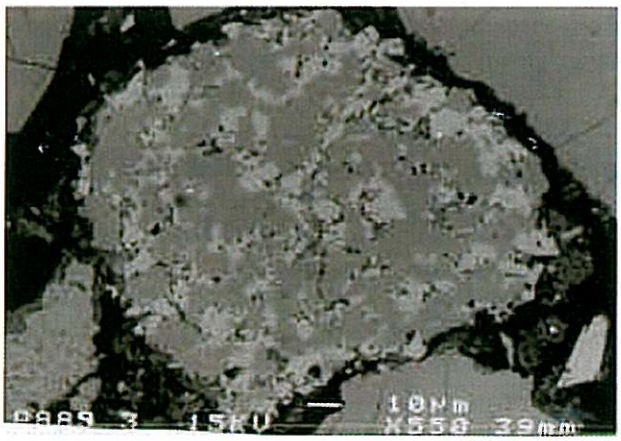
3



4



5



6

Plate -I

Plate I-1. Fresh plagioclase with albite twinning (A), orthoclase: cloudy grain (O), MM1-32, 4645' (- 37402), 22' below formation top. Thin section XP x 20.

Plate I-2. Microcline feldspar showing cross-hatch twinning. MM1-32, 4737.5' (-3780.5'), 12.5' below top. Thin section XP x 10.

Plate I-3. Perthite: K-feldspar grain intergrowth with albite along cleavages. MM1-32, 4741' (-3783'), 26' below formation top. Thin section XP x 20.

Plate I-4. Perthite: K feldspar intergrowth with albite in patchy form. JJ1-32, 4921' (3740'), 12' below formation top. BSE.

Plate I-5. Polycrystalline rock fragments with elongated grains components and sutured grain boundaries. FF1-32, 4946' (-3699'), 22' below formation top. Thin section, XP x10.

Plate I-6. Igneous rock fragments: micrograph quartz: quartz intergrowth in mosaic texture with k-feldspare. Q1-32, 4889' , 3' below formation top. SEM (BSE).

crenulated internal grain boundaries (Plate I-5). Such grains, though they are rare, typically metamorphic in origin. These types of fragments make up about 15% of the total average lithic fragments in the studied samples.

Igneous Fragments: A few rock fragments were identified as igneous in origin. Some of these, identified by Back Scattered Image, are polycrystalline quartz with equant grains, granitic in character and consisting of a mosaic texture of about equal percentages of microcrystalline quartz and potassium feldspar (Plate I-6). Others display micrographic textures (Plate II-1) and still others show intergrowth of quartz and perthite (Plate II-2). These kind of fragments make up about 25% of the total rock fragments.

Sedimentary lithic fragments: They represented the major rock fragments detected in the samples, make up about 60 %, or more of the total average rock fragments. They are represented by detrital carbonate aggregate (Plate II-3), mudstone fragments, which are frequent in some sand sequences, especially near sandstone/shale contacts (Plate II-4). Siltstone aggregate (Plate II-5), and chert, which is frequently present in minor amount in some samples varying between 0.3 and 1% of total rock volume, and between 0.1 to 0.4 % of the total rock composition (Table 3) and (Plate II-6). Recycled quartz grains are those derived from older sandstones rather than igneous or metamorphic rocks, they can be distinguished from first generation grains by the degree of roundness and abraded overgrowth (Plate III-1).

Inter-framework Material

The average of the total inter-framework materials including (detrital and authigenic cements such as (calcite, pyrite and iron oxides) are ranged from 18.78 to 33.28%, with an average of 20% of the total rock composition.

Matrix: The uppermost Bahi Formation shows that the framework grains in some samples are found floating in the clay matrix in the clay-rich sandstones. Here the matrix is mainly clay and microcrystalline quartz with very fine feldspar grains (Plate III-2). This clay is contemporaneous with deposition of the sand-size grains or introduced soon after deposition. In some samples, matrix is patchy, which may be interpreted as squashed clay fragments. Clay minerals are detected by SEM and XRD techniques in the most of studied samples, which include kaolinite, illite and traces of chlorite (Fig. 5).

Accessory Minerals

The topmost of the upper Bahi Formation samples contain only very minor amounts of accessory

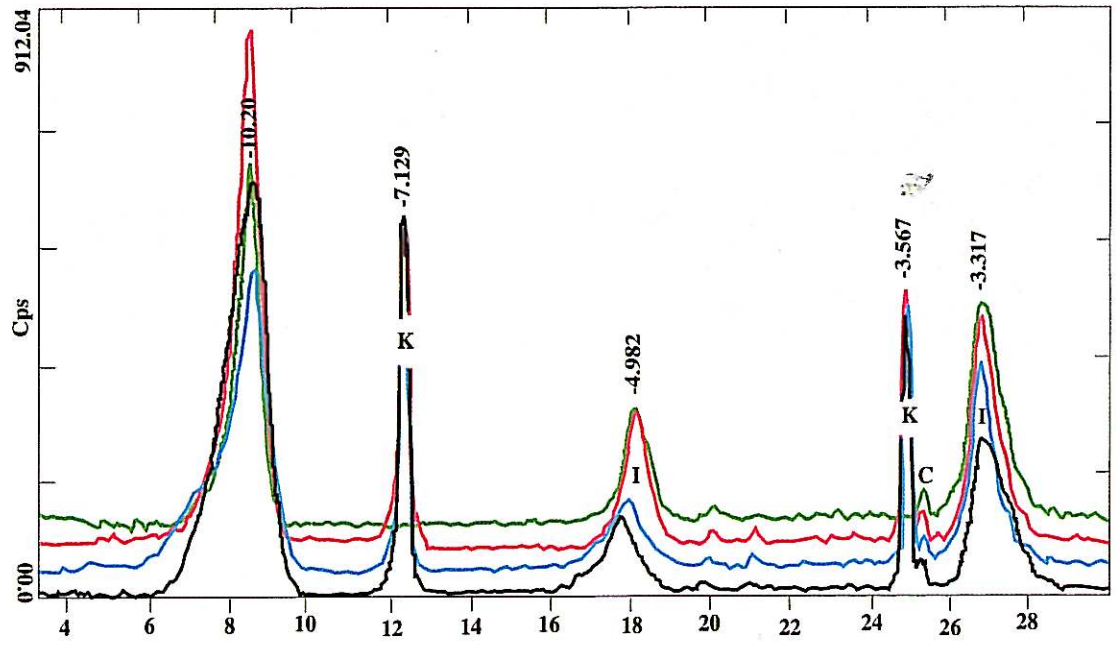


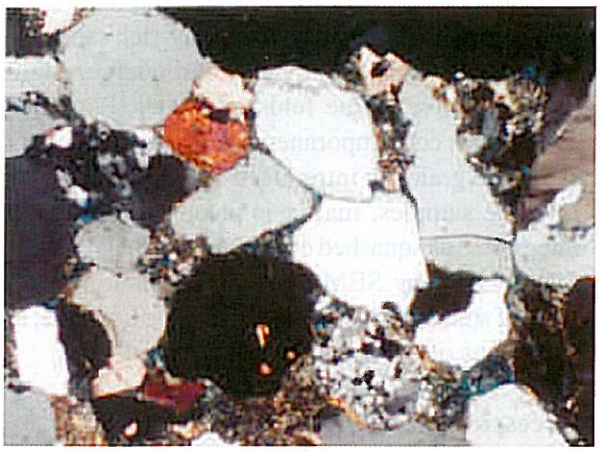
Fig. 5. XRD diffraction patterns of MM1-32, depth 4748' , 23' below formation top. Displays illite(I), and kaolinite (K) and traces of chlorite (C). The sample treatment patterns are (black: air dried, blue: glycolation, pink: heating to 350° C and green: heating to 550° C).



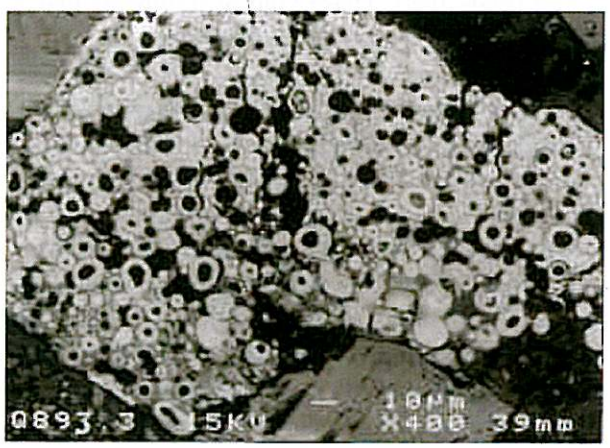
1



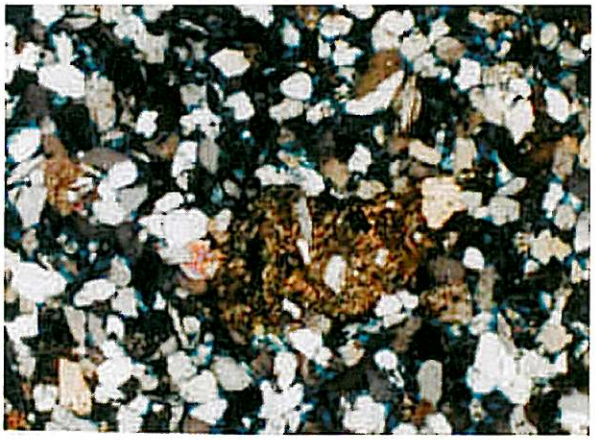
2



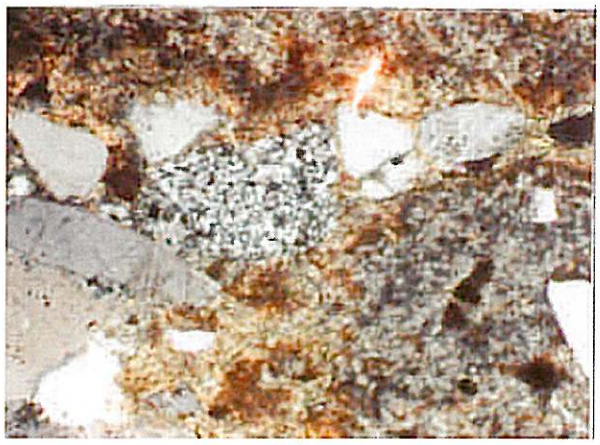
3



4



5



6

Plate-II

Plate II-1. Micrographic quartz fragments, suggestive of igneous sources. MM1-32, 4753' (- 3796'), 28' below formation top. Thin section XP x 10.

Plate II-2. Perithite-quartz rock fragments, suggestive of igneous sources. MM1-32, 4753' (- 3796'), 28' below top. Thin section XP x 20.

Plate II-3. Phosphatic rock fragment of micro algae, displaying quasi-oolitic texture, marine sediment source. Q1-32, 4893' (-3742'), 7' below formation top. BSE.

Plate II-4. Clast of silty clay fragments within fine sandstone. FF1-32, 4635' (3730'), 12' below formation top. Thin section XP x 4.

Plate II-5. Siltstone rock fragments, well rounded grains. Q1-32, 4895' (-3747'), 4' below formation top. Thin section X P x 4.

Plate II-6. Chert rock fragments. Q1-32, 4907' (-3756'), 21' below formation top. Thin section XP x 10.

minerals: iron oxides, zircon, tourmaline and rutile with traces of apatite, glauconite, and ilmenite. They show percentage variations range from 0.56 to 1.08% of the total average rock composition.

Mica: Both mica types (muscovite and biotite) are present in the studied samples, as they are quickly removed from their sources (metamorphic or igneous), carried and deposited by various depositional processes in sediments.

Muscovite: is the dominant type of mica in the studied samples, especially in the fine sandstone and clay-rich sequences (Plate III-3). It varies in amount from one well to another; the average value range between 0.58 to 1.8%, with average of 1.31% of total rock volume. The general indication is that the percentage of muscovite mica flakes increases gradually with decreasing sample grain size.

Biotite: it is present as traces in the topmost of the upper Bahi Formation, mainly in the fine-grained sandstone and in clay-rich sequences (Plate III-4). It is rare in coarse grain size beds, high porosity zones, and in the carbonates cemented units. This could be related to strong diagenetic processes, which occurred in these types of sequences, or to hydraulic grain size/shape sorting and separation during transport.

Glauconite: it occurs in the uppermost part of the cores. In the well II1-32, at 4899 feet (1493.6 m); 4904 feet (1495 m) and 4907 feet (1496 m). In the well Q1-32, at depth 4913 feet (1497.8 m). It occurs in traces as small grains, especially in the clay-rich laminae (Plate III-5).

Heavy Minerals

Two different types of heavy minerals; non-opaque and opaque, were distinguished.

***Non-Opaque Minerals*:** The non-opaque minerals such as zircon, tourmaline, rutile and apatite are present in minor amounts or as traces in the cored intervals. Average percentages range from 0.38, to 1.23, 0.56% of the total rock composition, with an average of 0.77% of total rock composition.

Zircon: is the most abundant non-opaque heavy mineral, representing about 60 to 70% of the total percent of the non-opaque heavy minerals (Plate III-6).

Tourmaline: it makes up the second most common non-opaque mineral with an average ranging from 10 to 20% of the total. It is common as inclusions in quartz (Plate IV-1).

Rutile: is also present making up about 15 to 20% of the total non-opaque heavy minerals. It occurs as inclusions in quartz, as tiny single grains in the matrix and in between expanded mica flakes in association with kaolinite alteration (Plate IV-2).

Apatite: this is abundant in the contact zone between the Sirte Shale and the Bahi Formation where it replaces phosphatic fragments, and is also present as traces in the uppermost Bahi Formation samples (Plate IV-3).

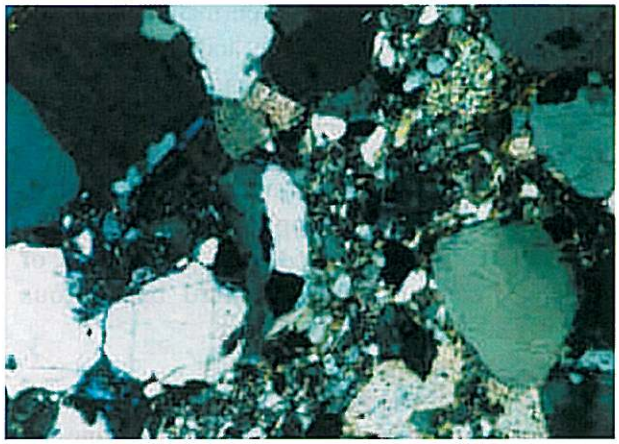
Opaque Minerals: are such as iron oxides (heamatite, limonite and magnatite), which formed as a result of oxidation of detrital iron-rich grains during or after deposition. Pyrite which can be derived from dissolved of rich sulphide-iron minerals, or from seas or formations waters, this occasionally precipitates under reduction conditions in marine environments (Berner *et al.*, 1979). The uppermost Bahi Formation shows presence of pyrite, iron-oxides and traces of ilmenite.

Pyrite: Is found scattered in the most of the uppermost Bahi Formation with average range from 0.2 to 1.9%. Most of the wells samples are much the same value except for Q1-32, which shows very low content. These may be related to the depositional environments (Plates IV-4 and 5).

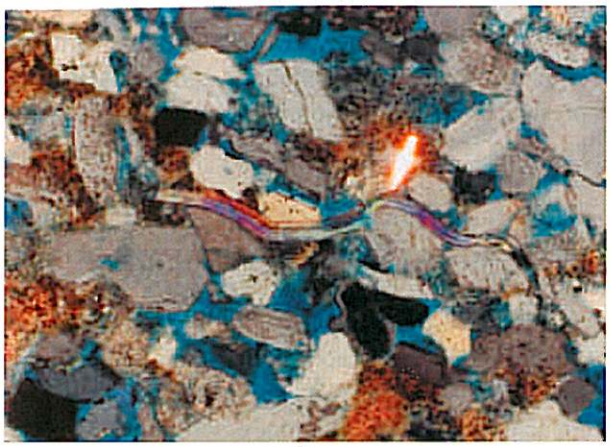
Iron Oxides: are widely spread, usually as coatings on the detrital grains or as authigenic cements; they include haematite and limonite. Haematite cement is present especially in middle and lower parts, which suggests continental depositional environments (Plate IV-6). The studied samples also show limonite, dark brown to yellowish in colour, coating the detrital grains especially in areas surrounding pyrite where it appears to be an alteration product (Plate IV-4). The total percentage of iron oxides is very minor ranging between .05 and 0.39% of the total rock composition. MM1-32 samples have the highest percentage distributed throughout some samples and appear to be absent from FF1 and LL1-32, well samples.



1



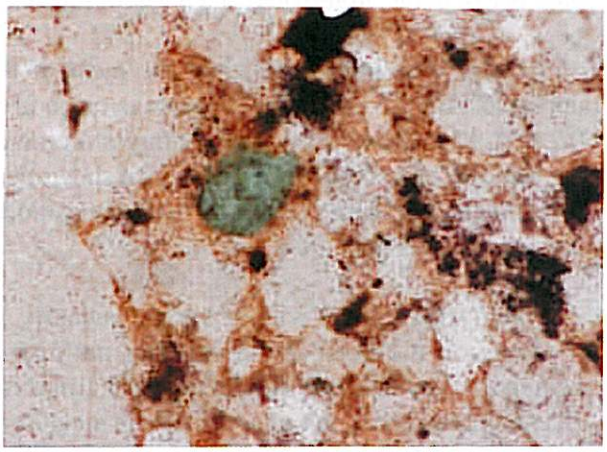
2



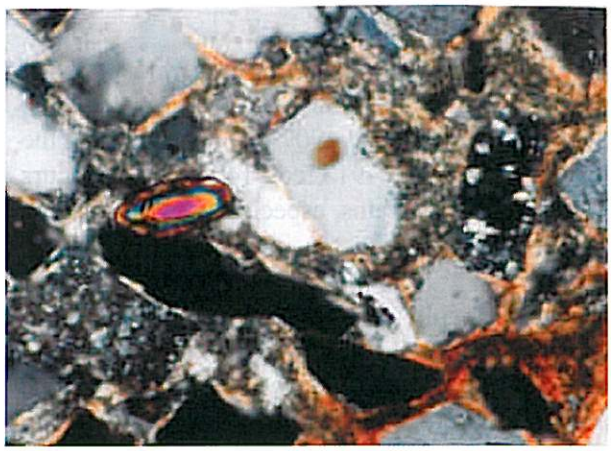
3



4



5



6

Plate-III

Plate III-1. Well rounded quartz grains suggesting recycled older sedimentary sources, shows also authigenic quartz overgrowth and anhydrite cement. Q1-32, 4907' (-3756'). 21' below formation top. Thin section XP x 20.

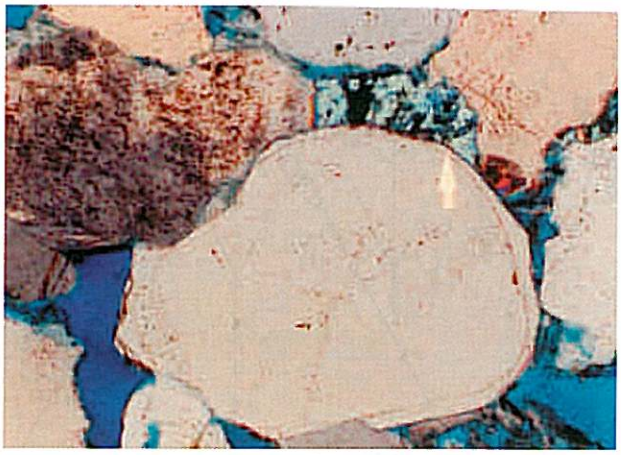
Plate III-2. Matrix and cements; very fine framework grains. Q1-32, 4886' (-3735'), at formation top. Thin section XP x20.

Plate III-3. Mica flakes bending in between detrital quartz grains due to sediments compaction. Q1-32, 4913' (-3762'), 27' below formation top. Thin section XP x10.

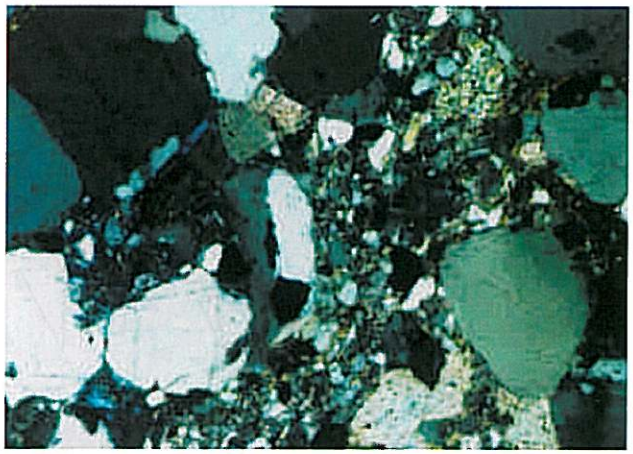
Plate III-4. Biotite flakes bending in between detrital grains. MM1-32, 4741' (-3784') 16' below formation top. Thin section XP x10.

Plate III-5. Glaoconite grain Q1-32, 4913' (-3762'), 27' below formation top. Thin section XP x20.

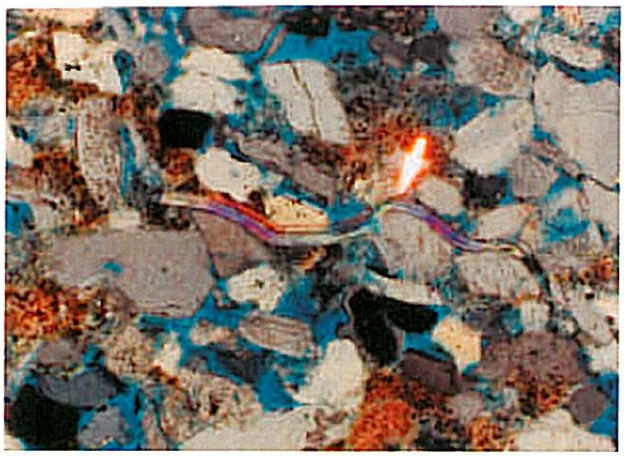
Plate III-6. Zoned zricon in subrounded crystal shape probably recycled. Q1-32, 4905' (-3754'), 19' below formation top. Thin section XP x10.



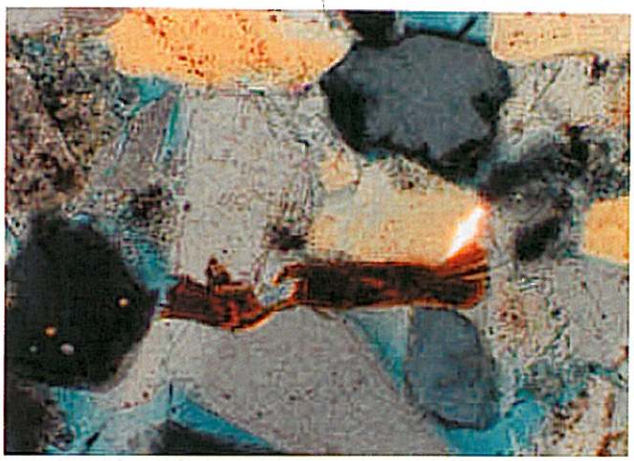
1



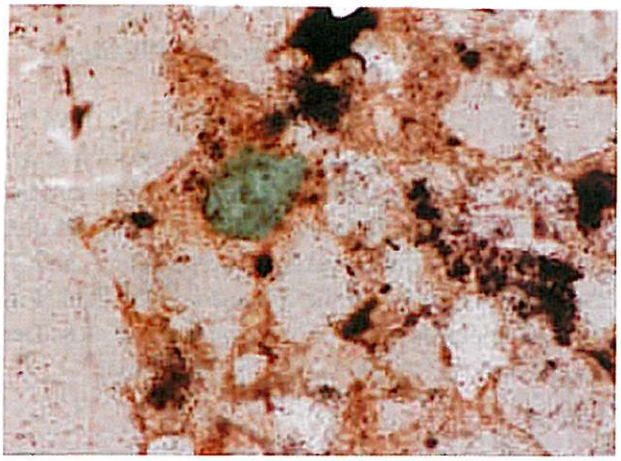
2



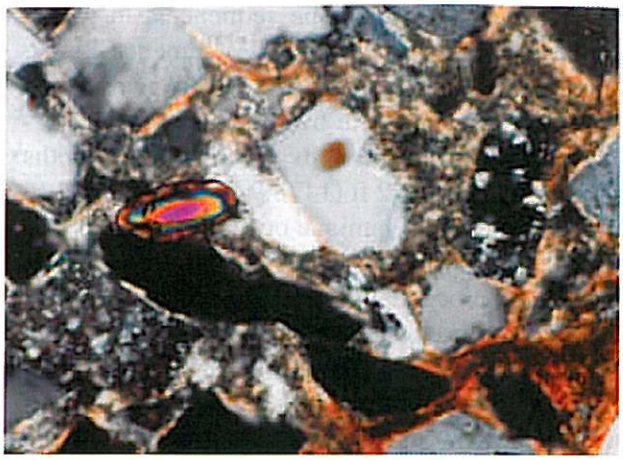
3



4



5



6

Plate -IV

Plate IV-1. Tourmaline inclusion in quartz. Q1-32, 4889' (-3738'), 3' below formation top. Thin section XP x10.

Plate IV-2. Needle-shape rutile crystals inclusion in quartz grain. FF1-32, 4645' (-3740'), 22' below formation top. Thin section XP x10.

Plate IV-3. Phosphate – apatite fragment. LL1-32, 4850' (3740'), 15' below formation top. BSE.

Plate IV-4. Discontinuous laminae of pyrite and authigenic limonite. MM1-32, 4729.2' (-3772.2'), 4.2' below formation top. Thin section XP x20.

Plate IV-5. Authigenic formboidal pyrite. FF1-32, 4628' (-3723') at top. SEM.

Plate IV-6. Haematite cement locally precipitated between and around the detrital grains. Q1-32, 4895' (-37442), 9' below formation top. Thin section XP x20.

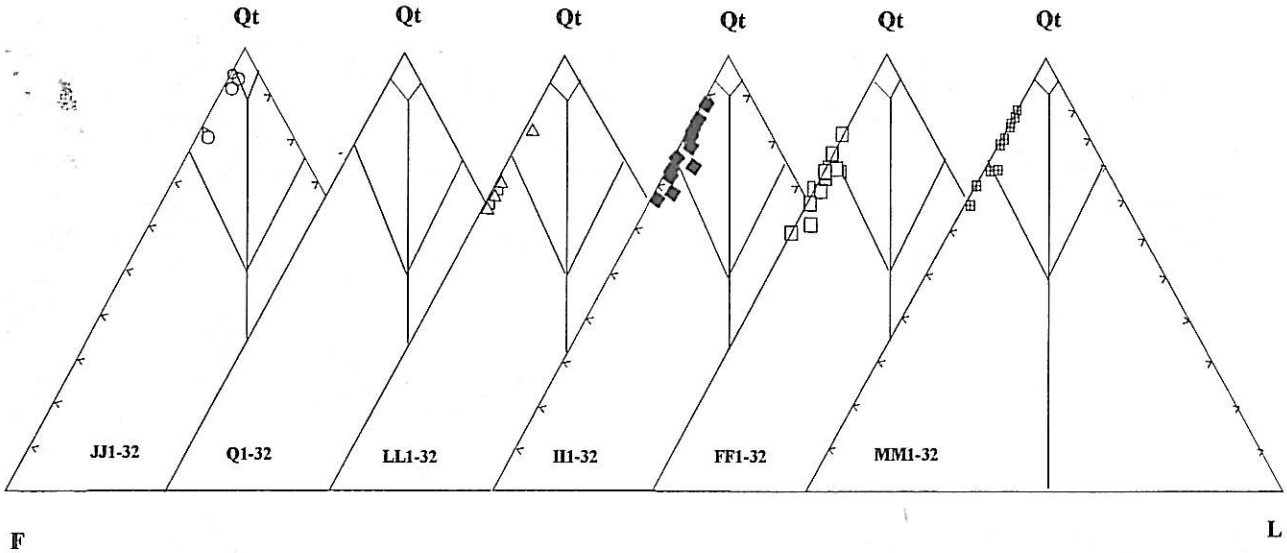


Fig. 6. QLF diagram (after Pettijohn, 1987). for the framework grain composition of the uppermost Bahi Formation samples from the study area wells (JJ1-32, Q1-32, LL1-32, II1-32, FF1-32 and MM1-32. All the samples fall within subarkosic and arkosic fields (Qt: total quartz, F: total feldspars, L: total rock fragments).

Ilmenite: It is present in traces as single and skeletal crystals (Plate V-1).

Dolomite-Rich Units

The uppermost Bahi Formation contains a few thin beds of dolomite and some sands rich in carbonate cement. The dolomite beds range in thickness from 2 to 4 inches (5-10 cm), inter-bedded with the sandstone sequences, in which carbonate (dolomite and calcite) cement fills the porespace between the framework grains and crystals. The dolomite beds occur in well LL1-32, two dolomite thin beds were noted at depths 4850.9 ft and 4852.2 ft (1478.9 and 1479.3 m). In well FF1 dolomite laminae occur at depth 4631 ft (1411.9 m). The dolomite in these thin beds is crypto to microcrystalline, showing almost idiotopic crystals textures with some xenotopic textures (Plate V-2). Widely dispersed, small patches of pyrite occur throughout the beds or as infills of fine fissures, quartz and feldspar grains are scattered through the beds.

Porosities

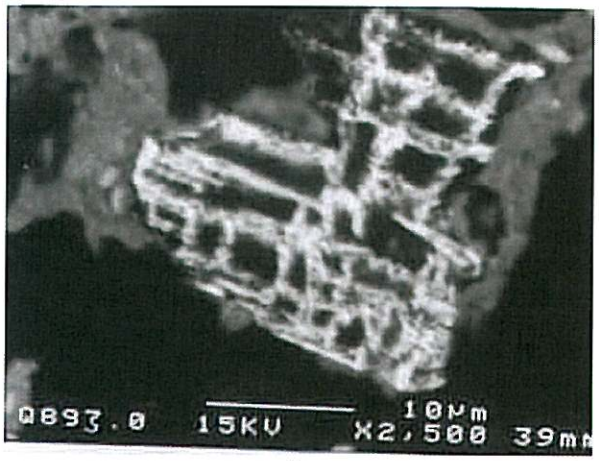
Primary Porosity is not easy to detect primary porosity in the upper Bahi Formation as the sediment has been subjected to a range of diagenetic processes. As a result primary porosity may have been completely plugged by authigenic cements precipitated on detrital grains with interlocking texture (Plate V-3), or by pore-filling cement, which may display detrital grains floating in cements such as in carbonate (Plate V-4). Partial reduction of primary porosity is indicated by precipitation of authigenic cements associated with free pore space (Plate V-5). Enlargement of primary porosity is indicated by alteration and dissolution of detrital grains and matrix (Plate V-6). These changes may be classified as secondary porosity.

Uppermost Bahi Formation Classification

Applying the classification model find by (McBride, 1963) and modified by (Pettijohn *et al.*, 1987), the uppermost Bahi Formation studied samples show that 32 samples out of 55 (58%) of the studied samples fall in the sub-arkosic arenite field, and 23 samples (42%) fall in the arkosic arenite field (Fig. 6). The uppermost Bahi Formation may be classified as sub-arkosic to arkosic-arenite sandstone.

CONCLUSION

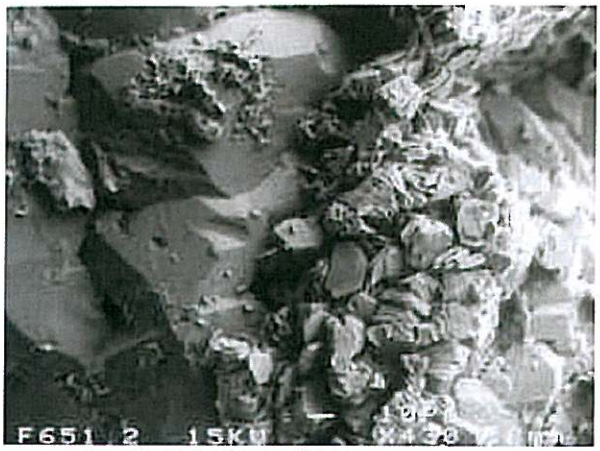
The Bahi Formation consists of sandstone sequences interbedded with shale beds, the formation, subdivided to upper and lower units, was deposited mostly under continental conditions. The presence of glauconite in the uppermost part of the upper unit is suggestive of a marine influence. The petrographic investigations of the uppermost Bahi Formation leads to the following conclusions:



1



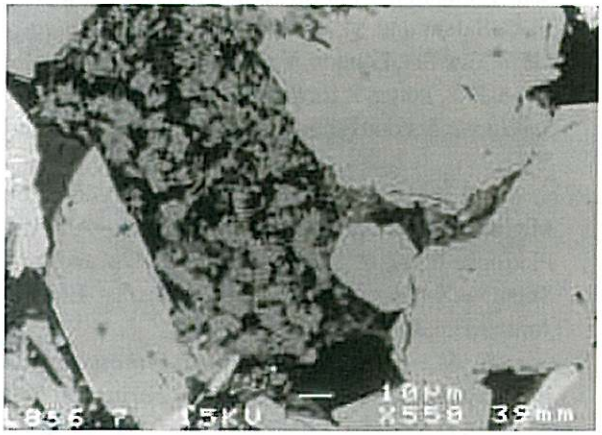
2



3



4



5



6

Plate -V

Plate V-1. Ilmenite mineral structure Q1-32, 4893' (-3742'), 7' below formation top. SEM.

Plate V-2. Dense crypotcrystalline dolomite laminae with fissures filled with relatively coarser idiotopic dolomite crystals, partially replaced by authigenic pyrite. Q1-32, 4895' (-3744'). 9' below formation top. Thin section XPx4.

Plate V-3. Authigenic quartz overgrowth and kaolinite completely filling the pore space between the detrital grains. FF1-32, 4651' (-3746'), 23' below formation top. SEM.

Plate V-4. Framework grains floating in early poikilotopic calcite cement, shows corrosion of quartz grains margins. JJ1-32, 4824' (-3755'), 15' below formation top Thin section XP x 10.

Plate V-5. Authigenic kaolonite pore filling partially occupied part of intergranular porosity, LL1-32, 4856' (-3747'), 7' below formation top. BSE.

Plate V-6. Porosity enlargement due to dissolution of matrix and unstable grains. MM1-32, 4784' (- 3791'), 23' below formation top. Thin section XP x20.

Monocrystalline quartz is the dominant mineral in the uppermost Bahi Formation. It represents up to 76% of the total rock framework; feldspar minerals represent the second mineral represents about 22% and rock fragments display only minor percent. Main feldspar mineral is potassium feldspar (orthoclase and microcline), and less amounts of plagioclase (albite and oligoclase). Perthite grains are largely authigenic, with intergrowth in irregular and patchy forms rather than in a regular pattern within and parallel to the cleavages. In general SEM (BSE) investigation shows that the percentages of feldspars are much higher than the calculated percent by automatic Point Counter, these will affect the classification of the formation.

Rock fragments represent only a minor component, most of these are extrabasinal but some siltstone and mudstone fragments are almost certainly intraclasts formed as rip-up clasts from underlying beds. The presence of polycrystalline aggregates, and other rock fragment is highly controlled by grain size; coarse sandstones display higher percentage of coarsely crystalline fragments than the finer ones.

The common accessory minerals include mica (muscovite and biotite), non-opaque minerals (zircon, tourmaline and rutile); and opaque minerals (iron oxides and ilmenite) are present in trace amounts. The study shows only traces of glauconite, even though the cores are taken near or at the topmost of the upper Bahi Formation, which is described in the literature as glauconitic. The fact of low amount of glauconite in the samples can be related to diagenetic alteration processes. Glauconite is best seen in the well LL1-32 samples, where its presence, in addition to dolomite beds, support the idea that the uppermost part of the Bahi Formation was deposited in marine depositional environments and it is approximate thickness is about 30 feet. These show some differences from the pervious studies, which determined the thickness of these marine sediments with about 20 feet.

Matrix is well developed in some units and comprises a mix of clay minerals, fine grained quartz, feldspars and other minerals. Illite and kaolinite are the dominant clay minerals, whereas few samples indicate the presence of traces of chlorite. The primary porosity is hard to distinguish from the secondary porosity as the formation had been subjected to a complex diagenesis processes. As a result the uppermost Bahi Formation can be classified as subarkosic to arkosic - arenite.

ACKNOWLEDGEMENTS

I wish to express my sincere thanks and appreciation to Dr. M. Anketell for his supervision of this work at the University of Manchester. Special thanks are extended to Mr R. Aburawi ex-exploration manager of Waha Oil Company – Libya, for providing the materials for this study and to Dr. Bourima Belgasem the manager of PRC for his unlimited support.

REFERENCES

Abbas, M. S., 1988. *Bahi Formation Time Map.* Unpublished report, Waha Oil Company, Tripoli, Libya.

Baird, D. W., 1964. *Stratigraphy of the Bahi Sandstone, Sirt Basin, Libya.* (Internal Report No. 54), Oasis Oil Company - Libya Inc.

Barr, F. T., and Weegar, A. A., 1972. Stratigraphic Nomenclature of the Sirte Basin, Libya. *Petrol. Explor. Soc. Libya*, Tripoli, 179 p.

Berner, R. A., Baldwin, T., George, R. and Holdern, Jr., 1979. Authigenic iron sulfides as palaeosalinty indicators. *J. Sediment. Petrology*, **49**. no. 4, 1345-1350.

McBride, E. F., 1963. A Classification of common sandstone. *J. Sediment. Petrology*, **33**, 664-669.

Mouzughi, A. J., 1991. Petrography and lithofacies of the Satal Formation in1 northwestern Sirt Basin, Libya. In: M. J. Salem and M. N. Belaid, eds. *The Geology of Libya*, Elsevier, London, **V**, 1841-1854.

Pettijohn, F. J., Potter, P. E., and Siever, R., 1987. *Sand and Sandstone*, Second Edition. Springer, Verlag, New York, 553 p.

Rohi, M. 1996. Geological History and Hydrocarbon Migration Pattern of the Central Az Zahrah – Al Hufrah Platform. In: M. J. Salem, A. S. El-Hawat and A. M. Sbeta, eds. *The Geology of Sirt Basin*, Elsevier, Amsterdam, **II**, 435-454.

Sghair, A. M., 1990. *Stratigraphy, Lithofacies and Environmental Analysis of the Bahi Formation in the North-western Sirte Basin, Libya*. MSc. Thesis, Geology Department, Glasgow University, 171 p.

Sghair, A. M., 1996. Petrography, Diagenesis and Provenance of the Bahi Formation in the Western Part of the Sirt Basin, Libya. In: M. J. Salem, A. S. El-Hawat, and A. M. Sbeta, eds. *The Geology of Sirt Basin*, Elsevier, Amsterdam, **II**, 65-82.

Petroleum Res. J. Vol. 15 (2003): P. 49–56, 5 Figs.

Controls on Porosity and Permeability of the Lower Cretaceous Nubian Formation Reservoir, Abu Attiffel Oil Field, Eastern Sirt Basin, Libya.

Milad M. Ben Rahuma*

ضوابط المسامية والنفاذية بخزان تكوين النوبة التابع للعصر الكريتاسي السفلي بحقل أبو الطفل النفطي، شرق حوض سرت، ليبيا

ميلاد رحومة

يشكل تكوين الحجر النوبي التابع للعصر الكريتاسي السفلي قاعدة التتابع الطبقي بحقل أبو الطفل النفطي وتعلوه، وبسطح عدم التوافق، صخوراً فتاتية تتمثل في العضو الثامن من مجموعة الركب تنتمي إلى الجزء العلوي من العصر الطباشيري.

يمثل تكوين الحجر النوبي، والذي لم يكن بالإمكان الوصول إلى الجزء السفلي منه، رواسب أنهار ذات نظام صرف متشعب ومتعرج. وتم من خلال الدراسة البتروغرافية تحديد عدة عوامل تتحكم في توزيع المسامية والنفاذية، حيث لوحظ أن أعلى نسبة للمسامية تتواجد في رواسب الأنهار المتعرجة وفي رواسب الحواجز الجانبية منها، وبالمقابل فإن رواسب ضفاف الأنهار لها مسامية ونفاذية منخفضتين.

تمثلت العوامل الثانوية بنتائج عمليات النشأة المتأخرة خاصة المواد اللاحمة (السيليكا والدولوميت والطين) وذوبان المكونات غير الثابتة (الفلدسبار والرواسب الأرضية)، كما أدى ترسب السيليكا والدولوميت الحديدي والكاولينايت إلى إنخفاض المسامية والنفاذية بالجزء العلوي من الخزان النفطي، أما نمو المرو وتكوين الكلورايت فقد أديا إلى إنخفاض المسامية والنفاذية بالجزء السفلي من الخزان النفطي. ونتيجة إلى زيادة دفن هذه الرواسب بالأعماق فقد أدى ذوبان الفلدسبار والمواد اللاحمة المكانية والرواسب الأرضية إلى إنتاج مسامية ثانوية وزيادة في النفاذية.

Abstract: *The Lower Cretaceous Nubian Formation forms the basal part of the sedimentary sequence in Abu Attiffel oil field. It is unconformably overlain by Upper Cretaceous clastic rocks (Member VIII of Rakb Group.) and the lower boundary is not reached. The Nubian Formation represents fluvial deposits of braided and meandering river systems.*

On the basis of detailed petrographic analyses several controls on porosity and permeability are designated to explain the present characteristics of the Nubian reservoir in Abu Attiffel oil field.

Primary controls, represented by the variation in the primary sedimentary texture of the facies, show a clear regular relationship to porosity and permeability values distribution. The highest porosity and permeability are present in the braided river and point bar deposits and, in contrast, the overbank deposits have lower porosity and permeability.

Secondary controls are represented by the product of the diagenetic processes particularly cements (silica, dolomite and clays) and dissolution of unstable constituents (feldspar and

* Petroleum Research Centre, P.O. Box 6431, Tripoli, Libya

matrix). The porosity and permeability in the upper part of the reservoir (braided river deposits) are mostly reduced by precipitation of silica, ferroan dolomite, and formation of kaolinite, whereas in the lower part of the reservoir (meandering river deposits) they are mostly reduced by quartz overgrowth, and formation of authigenic chlorite which can have a remarkably important effect in reducing the permeability. With further burial significant dissolution of feldspar, some authigenic cements (kaolinite), and matrix generate secondary porosity and enhance the permeability.

INTRODUCTION

The Abu Attiffel oil field is located on the Hameimat Trough, eastern Sirt Basin (Fig. 1) where the Nubian Formation and its equivalent strata have yielded major hydrocarbon production in addition to the Sarir and Messlah fields (Abdulgader, 1996). The stratigraphic sequence and lithofacies analysis of the area have been generally described (Hea, 1971).

The Nubian Formation forms the basal units of the Abu Attiffel oil field sedimentary sequence which is subdivided into three members (Fig. 2). The Upper and Lower members of the Nubian Sandstones represent braided and meandering river systems, whereas the middle member Nubian Shale represents shallow lake or lacustrine flood plain deposits. This formation is unconformably overlain by Upper Cretaceous clastic rocks (Member VIII of Rakb Group.) and the lower boundary is not reached. However, in a nearby well (Y1-80), the Nubian Formation overlies the basement rocks of igneous and metamorphic origins.

This study investigates the controls on porosity and permeability of the Nubian Formation. In order to achieve this objective one hundred and twelve thin sections were made from conventional cores recovered from A61-100 and A67-100 AGIP wells. Petrographic analyses revealed the existence of several diagenetic events which may explain the present characteristics of the reservoir.

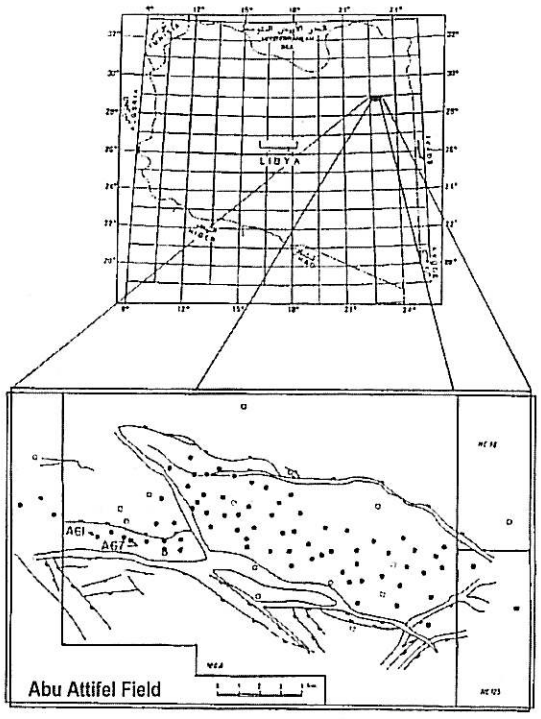


Fig. 1. Location map of the studied wells.

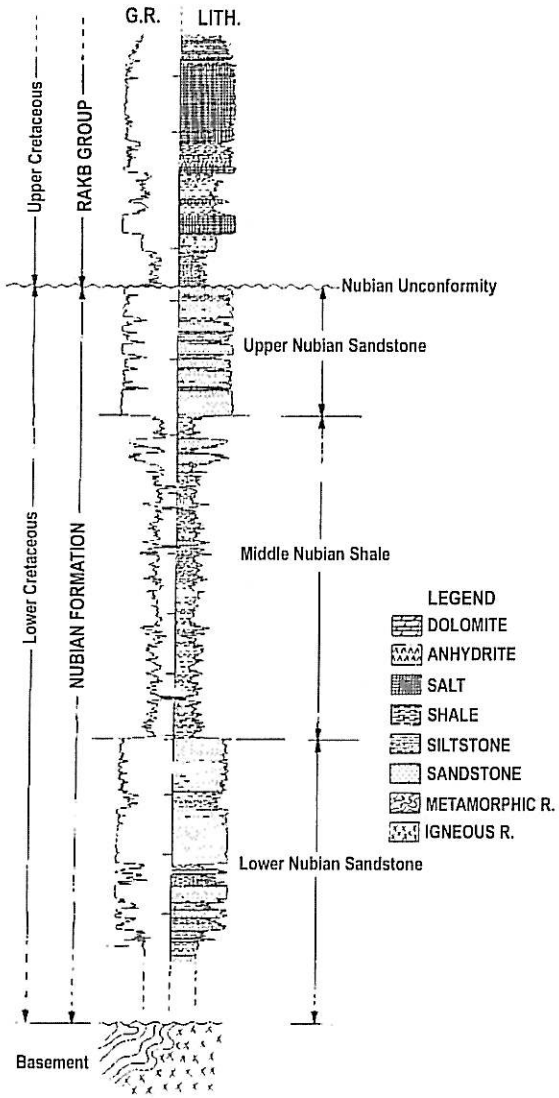


Fig. 2. Generalized composite section of Nubian Formation, compiled from final well logs of the wells A61-100, A64-100 and Y1-80.

Geological Settings

The Sirt Basin is tectonically a northwest-southeast elongated basin or embayment in which the major structural features trend northwest-southeast. Several trending faults in the basin probably reflect the original basement block-faulting and subsequent movement along these faults (Goudarzi, 1980).

Early Cretaceous rifting in the Sarir and Al Hameimat zone in the south of the Sirt Basin, therefore, formed E-W and ESE-WNW trending basin. The trend of these rifts was largely controlled by the craton margin-parallel basement faults of the north African megashear zone, which were in turn strongly influenced by Hercynian structural trends (Anketell, 1996).

Controls on porosity and permeability

The study of selected rock samples of the A61-100 and A67-100 wells suggest that the primary depositional facies were considered the predominant control on porosity and permeability distribution (Ben Rahuma, 1997). The relationship of porosity and permeability, however, appears to have been affected by diagenetic processes, namely, formation of authigenic cements and clays, and porosity enhancement by dissolution of unstable minerals and microfracturing.

Primary Controls

On the basis of primary sedimentary texture variations, the facies types show a clear linear relationship to porosity and permeability distribution. The highest porosity and permeability values are present in the braided river and point bar deposits. This phenomenon is due to the fact that these sandstones are coarse grained, with typical moderate to good sorting characteristics and low detrital clay content.

In contrast, the overbank deposits have low porosity and permeability values owing to their poor sorting and moderate to high detrital mud content (Fig. 3a).

Secondary Controls

Further controls to primary sedimentary texture (grain size, sorting and matrix content) seem to have affected porosity and permeability development. These are represented by several diagenetic features, observed in thin sections which have played a significant role in modifying the original porosity and permeability. The most important of these features are compaction, cementation and dissolution.

Several signs of compaction in the formation were observed, and appear to have reduced the porosity. Many thin sections display the effect of pressure solution on sand grains in contact, where grains initially with point contacts changed to concave-convex, or sutured contacts and sometimes stylolitic (Fig. 3b and 5a). Permeability has also been reduced by pore throat narrowing and squeezing of clay and labile grains.

Authigenic cementation: The most common authigenic cements in these sandstones are silica overgrowths and carbonates, with less important ones such as anhydrite, barite and pyrite. The net effect of all these mineral cements has diminished or nearly completely destroyed the primary intergranular porosity.

Authigenic quartz: Abundant authigenic cement throughout the formation shows a clear inverse relationship to the detrital mud content and is strongly controlled by the sorting of the sediments. Quartz overgrowth is the most common type of porosity destroyer in sandstones, particularly in braided river and point bar deposits (Fig. 3c and d). There is, however, sufficient porosity remaining even at deep burial depth, but the permeability decreases dramatically, owing to plugging of pore throats by silica cement (Fig. 3d).

Carbonate cement: It is the second common type of cement mostly found in the braided river deposits. It occurs as typically rhomb-shaped crystals which caused reduction of the intergranular and dissolution porosities (Fig. 3e and f).

Authigenic anhydrite, barite, and pyrite: They occur as scattered traces of cement in the studied section causing negligible diminishing of porosity.

Authigenic clays: Authigenic clay minerals show a wide distribution in the studied sandstones. Kaolinite and chlorite occur as late pore filling minerals (Fig. 4b and c), and chlorite is found also as pore lining (Fig. 4a). The presence of these authigenic clays have destroyed part of the effective porosity and drastically reduced permeability. Initial examination of the petrographic data suggests that no clear trend exists

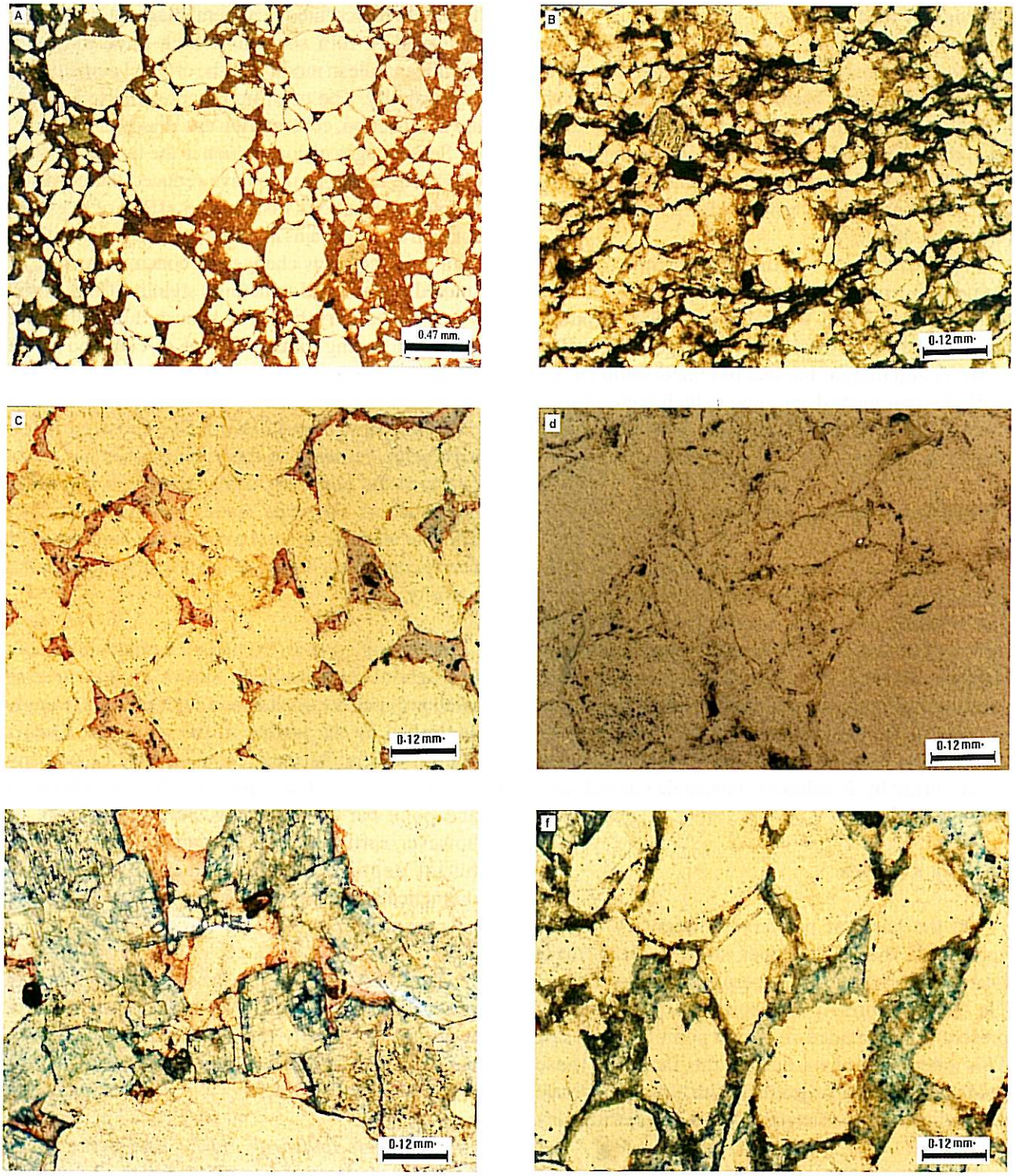


Fig. 3. A) An immature and poorly sorted texture, containing very high amount of matrix, has often inherited precipitation of authigenic cement, A67-100 well, 1472ft. B) Solution seems (low amplitude stylolites). This is formed during compaction of relatively uncemented material until relatively late in its diagenitic history, A67-100 well, 13976ft. C) A authigenic quartz cement (note euhedral crystal faces), in which a significant amount of pore space has been filled, A67-100 well, 13971ft. D) Advanced stage of silica cementation completely obliterating intergranular porosity, A67-100 well, 14052ft. E) Authigenic cementation, ferroan dolomite associated with anhydrite. In this case the dolomite is well recognizable by its rhombic outline, and sharply defined zonation. Ferroan dolomite is stained blue by Alizarin Red, and anhydrite remains unaffected (arrows), A67-100 well, 13944ft. F) Complex cementation. Quartz overgrowth formed as the first generations of cement were followed by ferroan dolomite. The ferroan dolomite marginally replaced the overgowth and both filled the porosity, A67-100 well, 13949ft. All of these figures are taken in plain light.

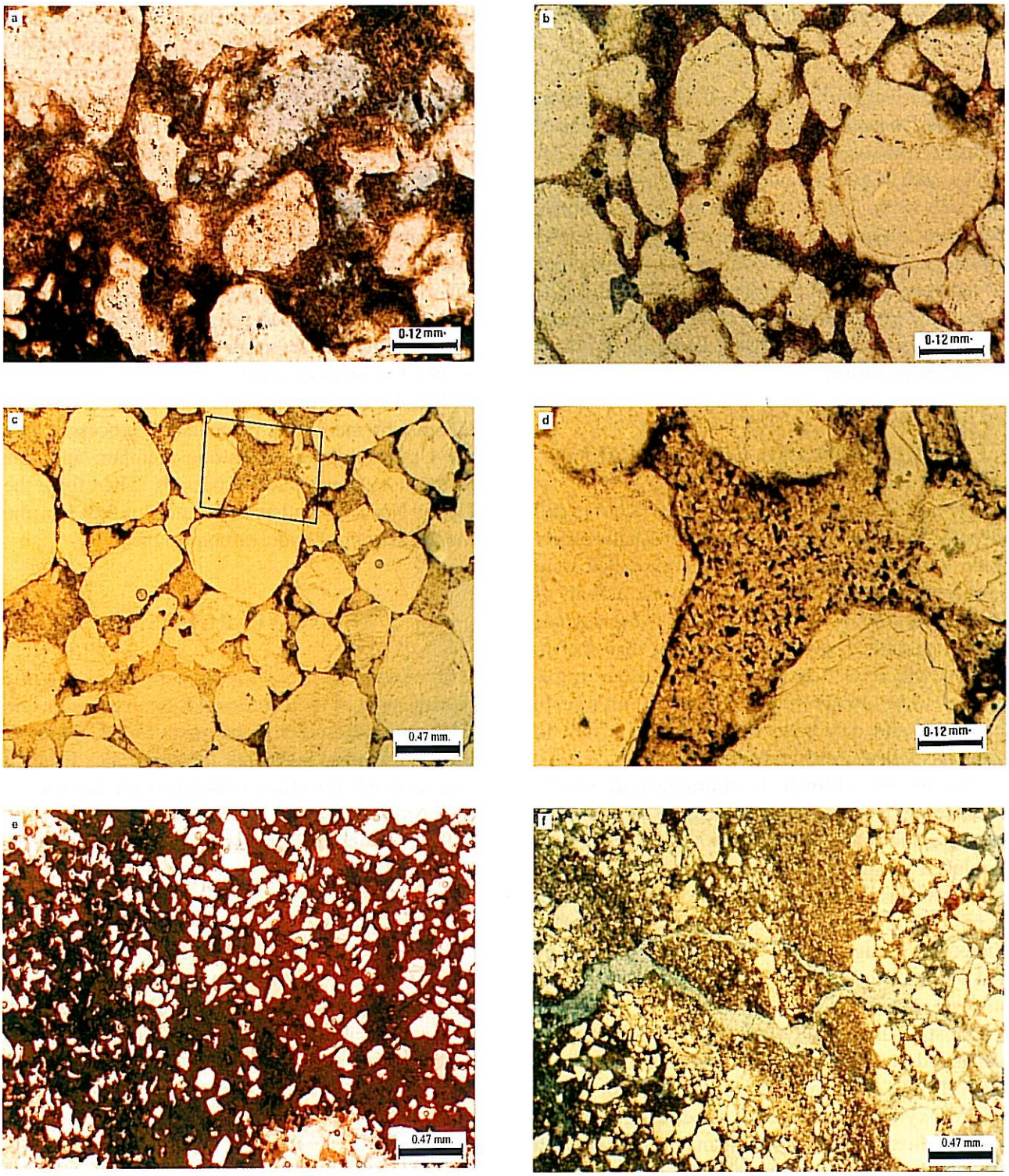


Fig. 4. A) Authigenic chlorite (as fibrous crystals), here seen pore filling and pore lining, clearly has destroyed the porosity and reduce the permeability, A61-100 well, 13902ft. B) Authigenic chlorite (here as plate like crystals), seen as pore filling, clearly destroyed the porosity, A67-100 well, 13982ft. C) Authigenic kaolinite cementation, here seen as pore filling completely is obliterating the porosity, A67-100 well, 13958ft. D) Enlarged view of the outlined area in the previous figure, showing more detailed crystal morphology of the kaolinite. This view showing micro-porosity of the kaolinite that has been completely filled by bitumen. E) Authigenic pyrite cementation, completely filling the intergranular porosity and replaced the matrix and detrital grains, A61-100 well, 14729ft. F) Ferroan dolomite filling fracture. This fracture may have formed at a relatively late during burial and has been completely healed by growth of dolomite cement, A67-100 well, 13944ft. All of these figures are taken in plain light, except of the figure E taken in reflected light.

between the distribution of authigenic clay minerals and porosity.

Porosity Enhancement: At effective burial secondary porosity was created by the dissolution of unstable constituent, particularly those of feldspar grains, rock fragments, matrix and authigenic cement (Fig. 5b to f). The dissolution of these unstable constituents highly enhanced the porosity, which later was reduced again by precipitation of a second phase of authigenic cement (ferroan dolomite, anhydrite, barite, and pyrite) and clays (chlorite and kaolinite) which were produced relatively during a later stage of diagenetic history.

DISCUSSION AND CONCLUSIONS

Authigenic kaolinite is characteristic of the braided river facies. The braided river deposits usually reflect depositional processes of high energy which were probably directly affected by the tectonic activity of the area during deposition. This allows feldspar grains to be aggregated in a higher amount than that in meandering river deposits. These feldspar grains appear to be completely alterated to authigenic kaolinite and can have a remarkable effect in reducing both porosity and permeability.

Authigenic chlorite is characteristic of the meandering river facies. It is clearly seen from the petrographic study of this facies that the chlorite is produced mostly from the alteration of the detrital mud, which is more abundant in the meandering river deposits. The distribution of authigenic clay minerals, therefore, is suggested to have been controlled by the variation of primary sedimentary texture and mineral content.

Most of the porosity is suggested to have been generated during burial by effects of carbonic acid. Burial and thermal maturation can cause decarboxylation of organic material, generating carbon dioxide (CO_2), which may combine with subsurface water to form carbonic acid (H_2CO_3), hence lowering the pH of the pore fluids and increasing the potential of the dissolution (Brown *et al*, 1989). The dissolution processes are directly related to the ability of formation fluid to move through the formation. Therefore, the dissolution processes are directly controlled by the primary sedimentary texture and burial rate through time. The overbank facies of meandering river deposits, characterized by high detrital mud content, prevents the movement of formation fluid and, therefore, less early diagenetic cementation and dissolution processes effect is expected. The braided river and point bar deposits containing little detrital mud and showing better sorting, render the dissolution processes more effective to enhance the porosity.

The cement and matrix dissolution porosities were mostly found in braided river deposits and were less abundant in point bar deposits, whereas intergranular and micro porosities were found more commonly in the overbank of meandering river deposits. Therefore, the braided river and point bar facies represent the best reservoir properties and form the main reservoir in the field.

The Lower Nubian Sandstone member is more affected by authigenic cementation processes than the Upper Nubian Sandstone member, and less affected by dissolution processes. Therefore, the Upper Nubian Sandstone member represents the main reservoir of hydrocarbons in the field.

ACKNOWLEDGEMENTS

I wish to express my sincere thanks to the management of the Petroleum Research Centre and Exploration Research Department for providing all the requirements necessary for this work . I should like to thank Dr Milad Ghummed for his fruitful discussion. Finally, I am most grateful to my colleagues, in particular Mr. Moh. Koni Omar, for their help.

REFERENCES

Abdulghader, G. S., 1996. Sedimentology and reservoir heterogeneities of the Nubian Formation, Southeastern Sirt Basin, Libya. In: M. J. Salem; A. S. El-Hawat and A. M. Sbeta eds. *The Sedimentary Basins of Libya, first symposium: The Geology of Sirt Basin* Elsvier, Amsterdam, **II,** 223-249.

Anketell, J. M., 1996. Structural history of the Sirt Basin and its Relationships to the Sabrata Basin and Cyrinaican platform, northern Libya. In: M. J. Salem; M. T. Busrewil, A. A. Misallati and M. A. Sola eds. *The Sedimentary Basins of Libya, first symposium: The Geology of Sirt Basin.* Elsvier, Amsterdam, **III,** 57-87.

Ben Rahuma,M.M.,1997.Depositional environment and reservoir geology of the Nubian Formation in the Agip A67-100 well, Eastern Sirt Basin. Internal Report, Petroleum Research Centre.

Brown, D. M., McAlpine, K. D., and Yole, R. W. 1989.

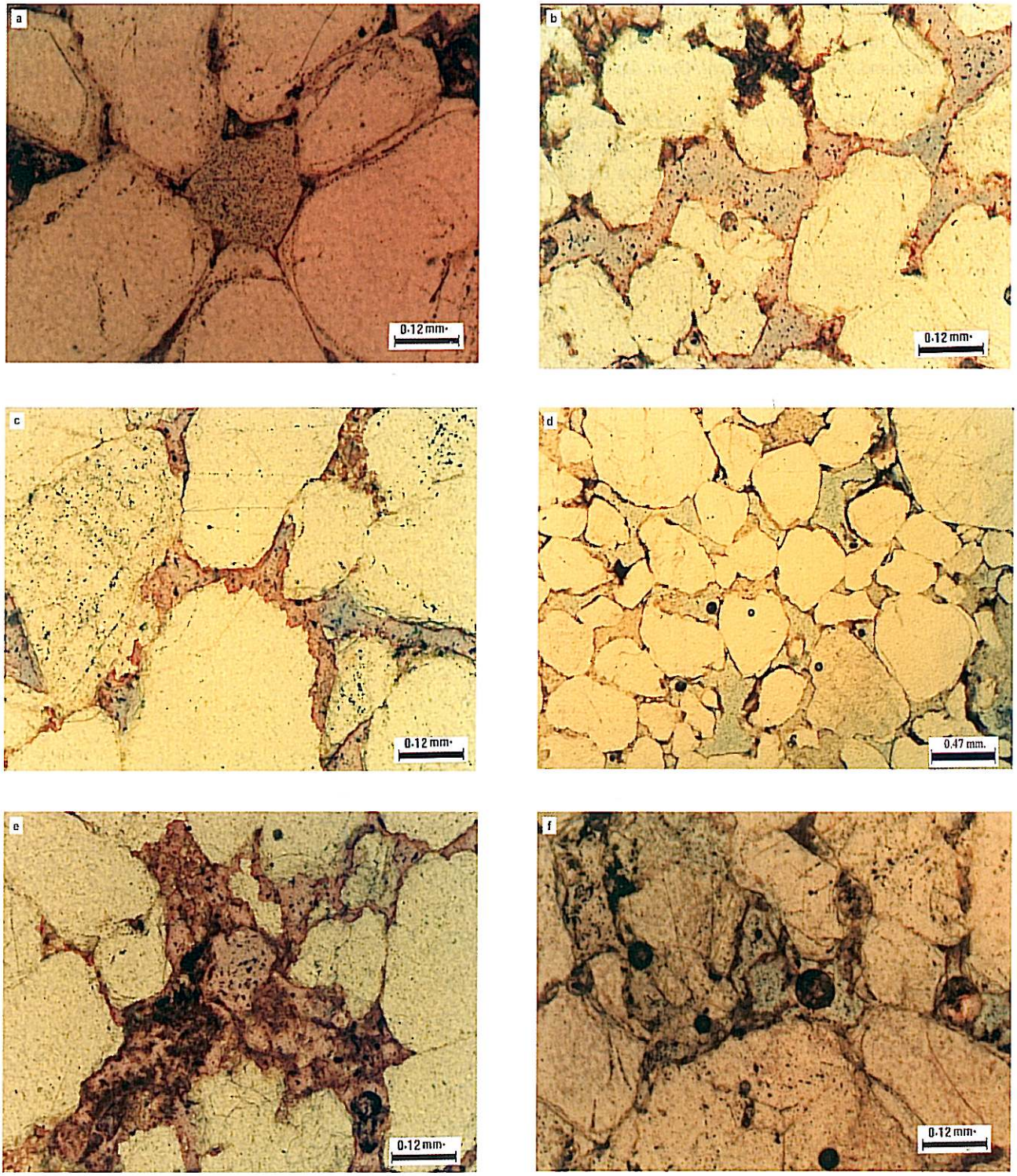


Fig. 5. A) Intergranular porosity confined by quartz overgrowth and physical grain compaction, A61-100 well, 13946ft. B) Chanalized porosity. This porosity have resulted from subsequent dissolution of matrix and authigenic cementing material has left interconnected pore spaces (appear mauve to blue coloured), A67-100 well, 14078ft. C) Partial dissolution of detrital quartz grain and quartz overgrowth has yielded leaching (secondary) porosity. This porosity has occurred as result of corrosion of the quartz grains during relatively late stage of the diagenitic history and has led to enhancement of the porosity and permeability, A67-100 well, 13967ft. D) This view show primary porosity completely destroyed by cementation of quartz overgrowth and authigenic kaolinite. From the other hand secondary porosity (marked by blue), were generated by dissolution. This secondary porosity are lined by head oil which it may have prevent re-cementation, A67-100 well, 13958ft. E) Selective leaching of unstable grains has generated secondary porosity. The remnant authigenic clay indicates original grain morphology, A67-100 well, 14048ft. F) The same phenomenon as in previous view, A61-100 well, 13891ft. All of these figures are taken in plain light.

Sedimentology and sandstone diagenesis of Hibernia Formation in Hibernia Oil Field, Grand Banks of Newfoundland. *Am. Assoc. Petrol. Geol.*, Bull., **73**, 5, 557-575.

Goudarzi, G. H., 1980. Structure - Libya. *In The Geology of Libya, 2nd symposium* In: M. J. Salem and M. T. Busrewil, eds. Academic Press Inc., London **III**, 879-892.

Hea, J. P., 1971. Petrography of the Paleozoic Mesozoic Sandstones of the Southern Sirt Basin, Libya. In: C. Gray ed. *1st Symposium of the Geology of Libya*. . 107-125.

Selley, R.C., 1992. *Applied Sedimentology* 2nd eddition. Academic Press, London.

Petroleum Res. J. Vol. 15 (2003): P. 57-64, 2 Figs.

Three New Ostracode Species of Buntonia and Protobuntonia from the Upper Cretaceous of Iraq

Jenan M. Taha Al-Bashir*

ثلاثة أنواع جديدة من طائفة الإستراكود، جنس بنتونيا وبروتوبنتونيا ضمن الكريتاسي العلوي بالعراق

جنان محمد طه البشير

أمكن التعرف ضمن التكاوين التابعة للتوروني العلوي والسانتوني بوسط وجنوب العراق على ثلاثة أنواع جديدة من طائفة الاستراكودا، هي بنتونيا إبن البيطاري وبنتونيا إبن رشدي وبروتوبنتونيا كازيبنسيس.

لقد تم تدوين نوع إبن البيطاري ضمن الكريتاسي العلوي بإيران، كما تمت، إضافة إلى دراسة تصنيف الأنواع موضوع الدراسة بالتفصيل، مناقشة نطاقهم الطبقي وتواجدهم.

Abstract: *Buntonia ibnalbaitari, and Buntonia ibnrushdi, two new Ostracode species of Buntonia, and Protobuntonia khasibaensis, a new species of Protobuntonia, are recorded from the Upper Turonian-Santonian formations of central and southern Iraq. Buntonia ibnalbaitari is also found in the Upper Cretaceous (Coniacian - ?Santonian) of Iran. Their taxonomy have been studied in detail and stratigraphic ranges and occurrences have be discussed.*

INTRODUCTION

The material examined in this study comes from subsurface cuttings and cores obtained from two drilling oil wells by the Iraqi National Oil Company, South Rumaila well-104, and East Baghdad Well-3; and three wells of the Basrah Petroleum Company (B.P.C.), Ghalaisan Well-1, Safawi Well-1, and Kifl Well-2 (Fig. 1). The samples studied are taken from the Upper Cretaceous Formation of the Khasib shaley and detrital limestones, the Tanuma fissile shale, and the Sadi marly limestone. The Khasib Formation is underlain uncomformably by the Mishrif or Kifl formations.

The Upper Cretaceous sequence is marked by a faunal break indicated by a first appearance of many ostracode genera and species, some of which are new, such as the new species of *Buntonia* and *Protobuntonia*: and disappearance of the older genera and species of the underlying strata of Cenomanian-Lower Turonian age.

The new species are described in details and their stratigraphic ranges are discussed (Fig. 2).

Repository

The Holotype specimens and the paratype specimens have been deposited with the author's collections. An internal catalogue numbering system has been used for these specimens.

*Oil Research and Development Centre, Baghdad – Iraq.

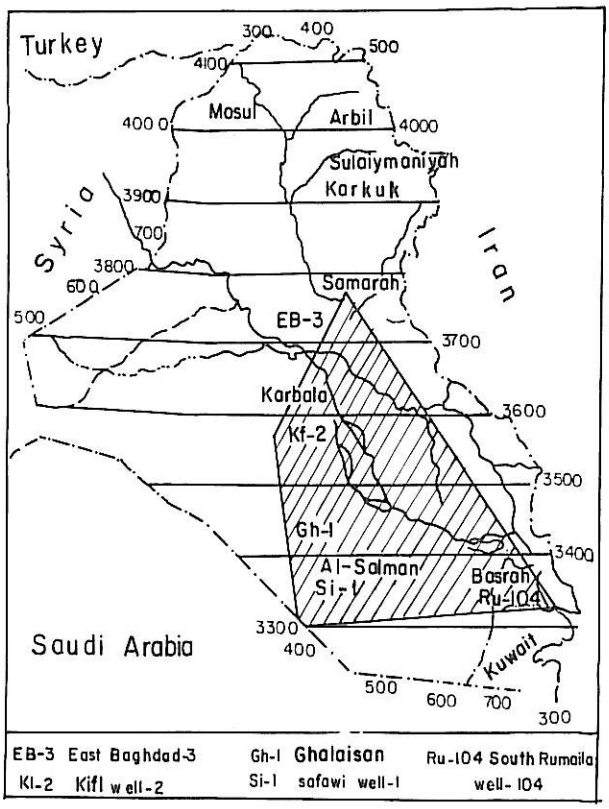


Fig. 1. Location map.

Systematic Description:

Subclass	OSTRACODA	Latreille, 1806
Order	PODOCOPIDA	Muller, 1894
Suborder	PODOCOPINA	Sars, 1866
Superfamily	CYTHERACEA	Baird, 1850
Family	TRACHYLE-BERIDIDAE	Sylvester-Bradley, 1948
Subfamily	BUNTONINAE	Apostolescu, 1961

Genus *Buntonia* Howe, 1935

Buntonia ibnalbaitari sp. Nov. pl. 1, figs. 1-7.

1973-*Buntonia* IRC_{33}, Grosdidier, pl.8, fig. 70 a-e.

Material: Total number of specimens are six. In Kifl Well-2, five specimens from the Tanuma Formation; In South Rumaila Well-104, one specimen has occurred in the base of the Sadi Formation.

Name: is named with reference to Abd Allah Ibn Al-Baitar , the celebrated Arab botanist in the twelfth century, who wrote two books which have made his name famous.

Diagnosis: A species of *Buntonia* with a smooth surface; three longitudinal ridges, the ventral being thick, a fourth short ridge is present between the median and the ventral ridge; one eye tubercle; a very narrow depressed anterior behind and parallel to the distinct anterior marginal area.

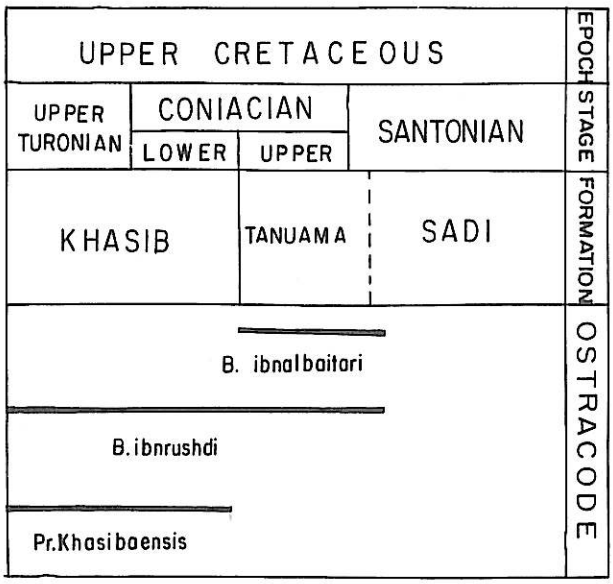


Fig. 2. Stratigraphic range chart of Bintonia ibnalbaitari, bintonia ibnrushdi and Protobuntonia khasibaensis.

Holotype: Femal carapace, BM(NH)OS12940, pl. 1, fig.1.

Paratype: J.T. 121, and H.T. (123-124).

Type locality and horizon: Kifl Well-2; Tanuma Formation, Upper Coniacian, at depth of 4370 ft.

Stratigraphic range: Upper Coniacian – Santonian.

Description: Carapace small, pear-shaped in lateral view. Greatest length is about the middle. Anterior margin is broadly and evenly rounded; posterior margin truncates in left valve, subrounded in the right valve. Dorsal margin is nearly straight; ventral margin is slightly concave typically turned upwards at posterior end. Left valve with pronounced posterior margin truncates in left valve, subrounded in the right valve.

Dorsal margin is nearlyh sraight; Left valve with pronounced posterior cardinal angle. No eye tubercle could be observed. The left valve is larger than the right.

A distinct and thickly developed marginal rim extends around the anterior margin continuing along the ventral margin. A very narrow depressed anterior area is present behind and parallel to the anterior margin rim.

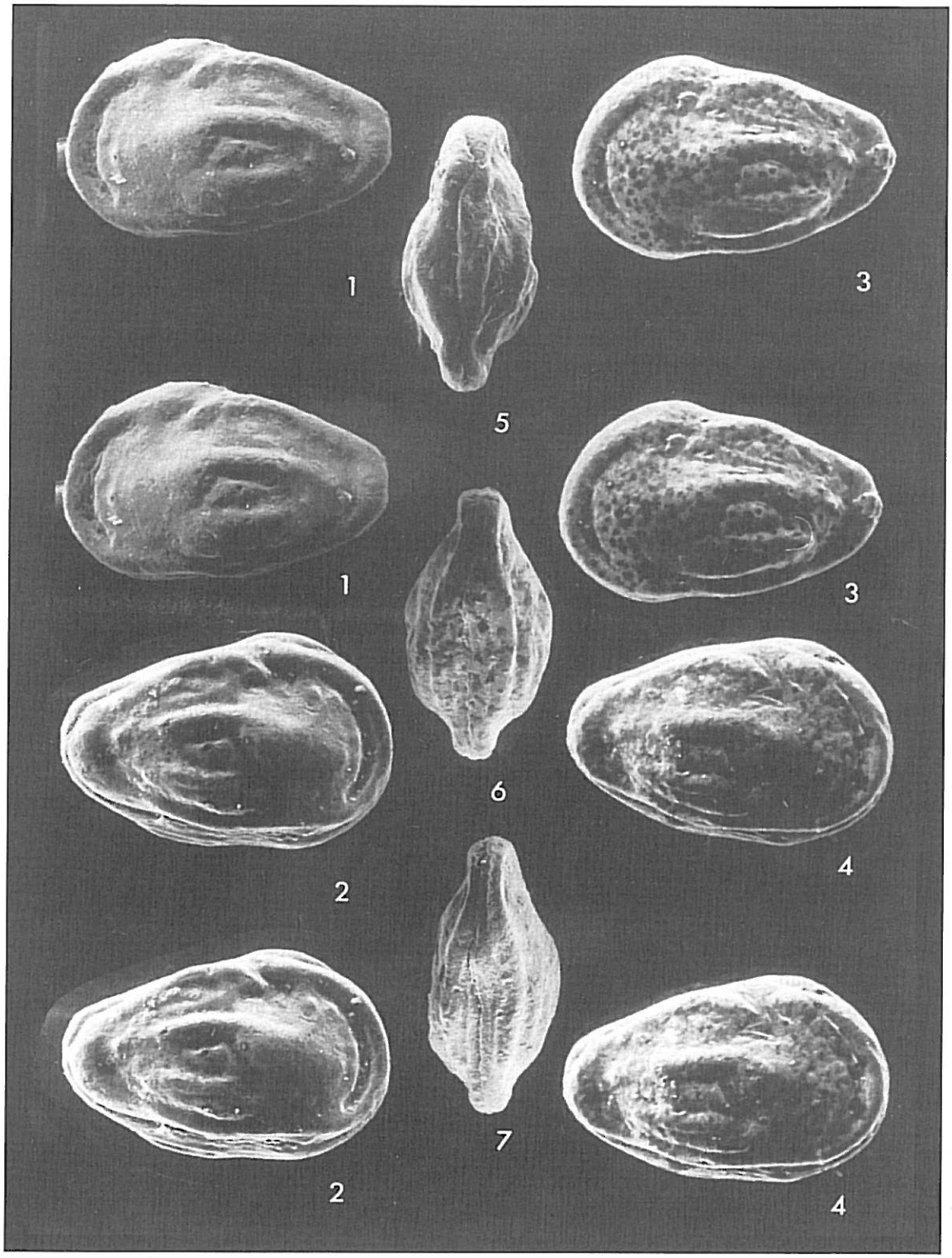


Plate - I

Buntonia ibnalbaitari sp. nov

All specimens are from the Tanuma Formation of Kifl Well-2.

Fig. 1. Female carapace, left valve, external, lateral view, (holotype OS 12940); stereoscopic paired photographs; 4370 ft; x103.
Fig. 2. female carapace, right valve, external, lateral view, (paratype J.T. 123); stereoscopic paired photographs; 4380 ft. x104.
Fig. 3. Female carapace, left valve, external, lateral view, (paratype J.T. 123); stereoscopic paired photographs; 4380 ft, x104.
Fig. 4. Female carapace, right valve, external, lateral view, (paratype J.T. 124); stereoscopic paired photographs; 4375 ft; x104.
Fig. 5. Female carapace, external, dorsal view, (paratype J.T. 124); 4375 ft; x92.
Fig. 6. Female carapace, external, ventral view. (paratype J.T. 123); 4380 ft; x90.
Fig. 7. Female carapace, external, ventral view, (paratype J.T. 121); 4360 ft: x92.

Main surface ornamentation consists of three pronounced longitudinal ridges; dorsal, median and ventral. The ventral ridge is thick and slightly swollen, begninning in the antero-ventral area, and fading at about three quarters of the length towards the posterior. A fourth short ridge present between the median and ventral ridges and bears a prominent pore cone.

The areas between the longitudinal ridges appear compressed. The entire surface of the carapace is smooth; a few very small pore cones and papillae are present in the posterior area at the ends of the median and ventral ridges, with faint ones in the anterior area and no internal details were seen.

Dimensions: (in mm)

		L.	H.	W.	L/H.
BM(NH) OS 12940	Female (Holotype)	0.490	0.315	0.260	1.555
J.T. 121	Female	0.490	0.330	0.240	1.484
J.T. 123, 124	Female	0.490	0.333	0.260	1.484

Discussion

Grosdidier (1973) illustrated forms which he called *Buntonia* IRC_{33} from the Santonian-Coniacian ? of the Coastal Fars Province in Iran which are identical to *Buntonia ibnalbaitari* sp. nov.

Occurrrnce

This species is known from the Upper Coniacian of Kifl Well-2, Santonian of South Rumaila Well-104; and from the Coniacian ?- Santonian of the Coastal Fars Province in Iran.

Buntonia ibnrushdi sp. nov.
Pl. 2, figs. 1-6

Name: Named after Abdul-Walid Ibn Rushid, a great Arab philosopher of Spain and who was celebrated in mediaeval Europe as Averrose of the twelfth century.

Diagnosis: A species of *Buntonia* with longitudinal rows of puncta in the central area; the rest of the valve is smooth. The eye tuberule is weakly developed. A slight ventral-lateral swelling is present. A thin marginal rim is present along the anterior and ventral margin. A distinet small node is situated on the poistrrior cardinal angle of the left valve.

Holotype: Male carapace, BM(NH) OS 12966, pl. 2, figs. (1-2)(5-6).

Paratype: J.T. 126 – J.T. 127.

Material: A total of 6 specimens have been found in the South Rumaila Well-104. five specimens from the Sadi.Tanuma and Khasib Formations, and one specimen from the uppermost beds of the Mishirf Formation(as contaminant).

Type locality and horizon: South Rumaila Well-104. Khasib Formation, Upper Turonian, depth of 2416m.

Stratigraphic range: Upper Turonian-Santonian.

Description: Carapace pyriform , male more elongate; greatest length passes through the central point. Anterior margin is broadly rounded; posterior margin is truncate; dorsal margin is slightly sinuous; entral margin is almost straight to weakly concave, with a very faint convexity centrally in the male. Dorsal and ventral margins converging strongly towards the posterior. Posterior cardinal angle of left valve is distinct and bears a small node. The left valve is larger than the right. The eye tubercle is weakly developed. Sexual dimorphism is pronounced. The central area appears swollen. A thin marginal rim is present along the anterior margin continuing along the ventral margin to the postero-ventral corner. The lateral surface has 7-9 longitudinal rows of pits or puncta in the central area of the valve; faint ribbing is developed between the median and ventrally placed puncta. A slight ventro-lateral swelling is present; the rest of the surface is smooth. In ventral view the ventro-marginal rim is seen. Internal details could not be observed.

Dimensions: (in mm)

		L.	H.	W.	L/H.
BM(NH) OS 12940	Female (Holotype)	0.630	0.330	0.260	1.909
J.T. 127	Female	0.540	0.305	0.282	1.770
J.T. 130	Female	0.610	0.380	0.305	1.605

Discussion

The species described by Sayyab (1956) as *Eohuntonia Seminuda* from the Upper Cretaceous strata of the Arabian Gulf Coast shows a close resemblance to *Buntonia ibnrushdi* sp. nov. in shape and outline, but differs in details of surface

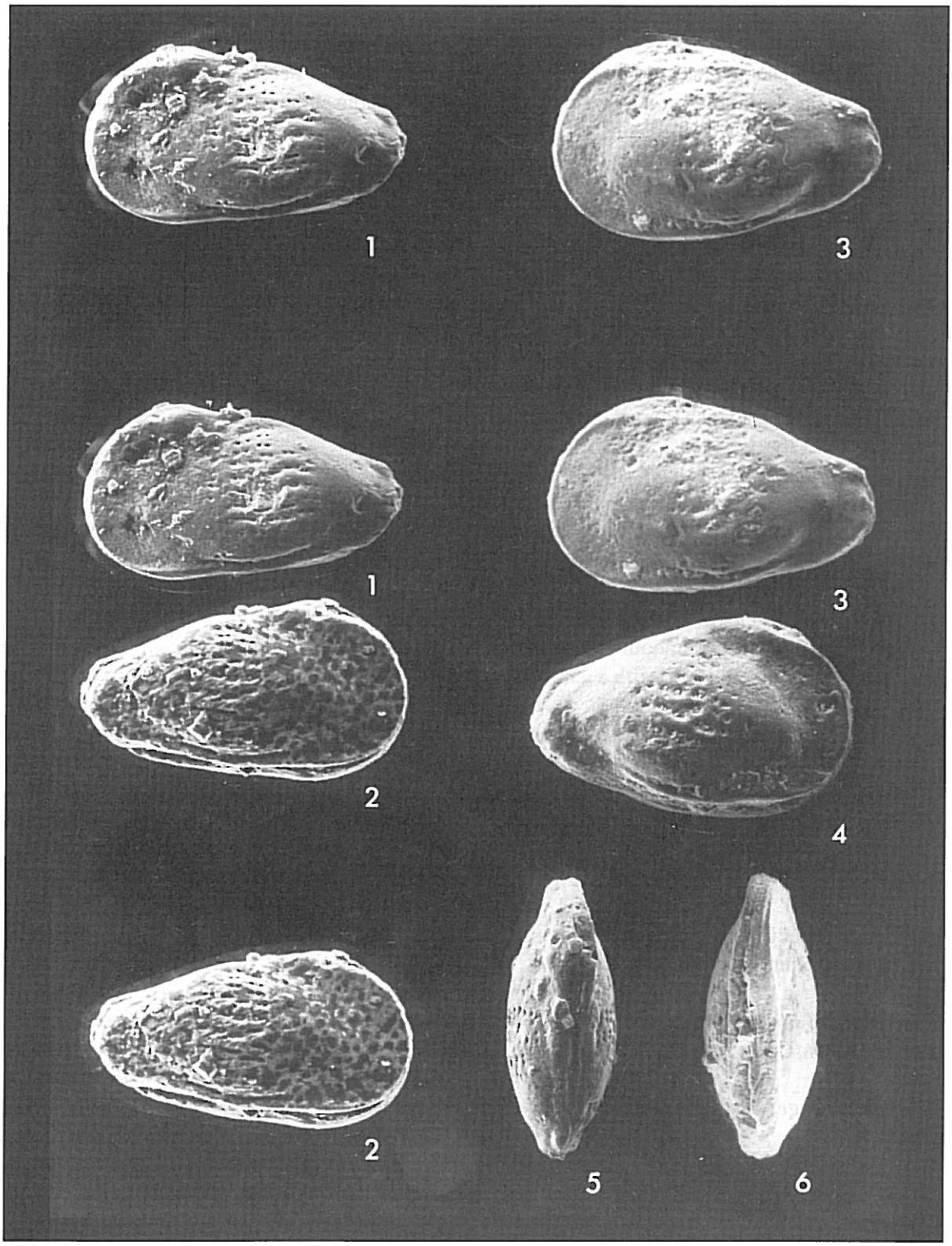


Plate - II

Buntonia ibnrushdi sp. nov.

All speciments are from the Khasib Formation of South Rumaila Well-104.

Fig. 1. Male carapace, left valve, external, lateral view, (holotype OS 12966); stereoscopic paired photographs; 2416 m; x79.

Fig. 2. Male carapace, right valve, external, lateral, view, (holotype OS 12966); stereoscopic paired photographs; 2416 m; x81.

Fig. 3. Female carapace, left valve, external, lateral view, (paratype J.T. 127); stereoscopic paired photographs; 2416 m. x95.

Fig. 4. Female carapace, right valve, external, lateral view, (paratype J.T. 127); stereoscopic paired photographs; 2416 m; x94.

Fig. 5. Male carapace, external, dorsal view, (holotype OS 12966); 2416 m; x72.

Fig. 6. Male carapace, external, ventral view. (holotype OS 12966); 2416 m; x73.

ornametation. *Buntonia ibnrushdi* sp. nov. has been placed in *Buntonia* on the basis of its external characters, no internal characters could be observed in these species so the possibility of a new genus is left for future investigation.

The species illustrated by Grosdidier (1973) as *Buntonia* IRE_9 from the Coniacian? of the Coastal Fars Province of Iran resembles *Buntonia ibnrushdi* sp. nov. in shape, general outline, in having a compressed anterior area; but differs in having a completely smooth lateral surface.

Occurrence: Known so far from the Upper Turonian-Santonian and as contaminants in the uppermost Lower Turonian of South Rumaila Well-104.

Genus *Protobuntonia Grekoff*, 1954
Protobuntonia khasibaensis sp. nov.

Name: After the Khasib Formation.

Diagnosis: A small species of Protobuntonia with a punctate surface except for a smooth area at the posterior, a very feeble eye tubercle with a shallow short sulcus behind it, a narrow shallow sulcus borders and parallel the wide antero-marginal zone.

Holotype: Female carapace, BM (NH) OS 12941, pl.3, fig. 1.

Paratype: J.T. 129 – J.T. 130.

Material: 4 specimens from the Khasib Formation of South Rumaila Well-104.

Type locality and horizon: South Rumaila Well-104; Khasib Formation, Upper Turonian, depth of 2408m.

Stratigraphic range: Upper Turonian – Lower Coniacian.

Description: Carapace small, elongate to subtriangular in lateral view, maximum length at about the middle, maximum height in front of the middle. The dorsal margin is nearly straight; the ventral margin is slightly concave; both margins converge towards the acutely pointed posterior end. The anterior margin is broadly and evenly rounded. The postero-cardinal angle is curved and distinct in the left valve, less distinct in the right. The eye tubercle is very feebly developed. The left valve is larger than the right, with overlap strongest anterodorsally, posterodorsally at the upper part of the posterior margin and along the ventral margin.

The lateral surface is punctuate except for a smooth area at the posterior. A very narrow shallow sulcus borders the wide anteromarginal zone parallel to the margin, another narrow sulcus parallel to the posterior margin bounds the smooth posterior marginal area, especially in the ventral part. A shallow sulcus lies just behind the feeble eye tubercle. The internal features could not be observed.

Dimensions: (in mm)

		L.	H.	W.	L/H.
BM(NH) OS 12941	Female (Holotype)	0.630	0.380	0.305	1.657
J.T. 129	Female	0.630	0.380	0.305	1.657
J.T. 130	Female	0.610	0.380	0.305	1.605

These species seem to be females rather than males when compared with other species belonging to *Protobuntonia*.

Discussion

Protobuntonia semmamaensis Bismuth and Le Fevre (1981) recorded by Bismuth *et al.* (1981) from the upper part of the Lower Cenomanian to Middle Cenomanian of Tunisia is similar to *Protobuntonia Khasibaensis* sp. nov., but the latter differs in having a more pointed posterior end, more distinct posterior cardinal angle, broader and evenly rounded anterior margin, wider anterior marginal zone with smaller punctuation, and the overlap is stronger anterodorsally. This species may be descended from the older *Protobuntonia semmamaensis*. *Protobuntonia numidica* Grekoff (1954) illustrated by Van Bold (1964) from the Santonian of Egypt, and by Reyment and Elofson (1959) who designated it as *Buntonia (Protobuntonia) numidica* (Grekoff) from the Santonian of Tunisia, shows some resemblance to *Protobuntonia Khasibaensis* sp. nov. in general outline, in possessing a pointed posterior end, and in the presence of a distinctly developed punctate lateral surface with smooth posterior marginal area; but the latter differs in having a very narrow curved sulcus bounding the wide antero-marginal zone, and a short sulcus lying just behind the eye tubercle.

Occurrence

Known so far from the Upper Turonian – Lower Coniacian of South Rumaila Well-104.

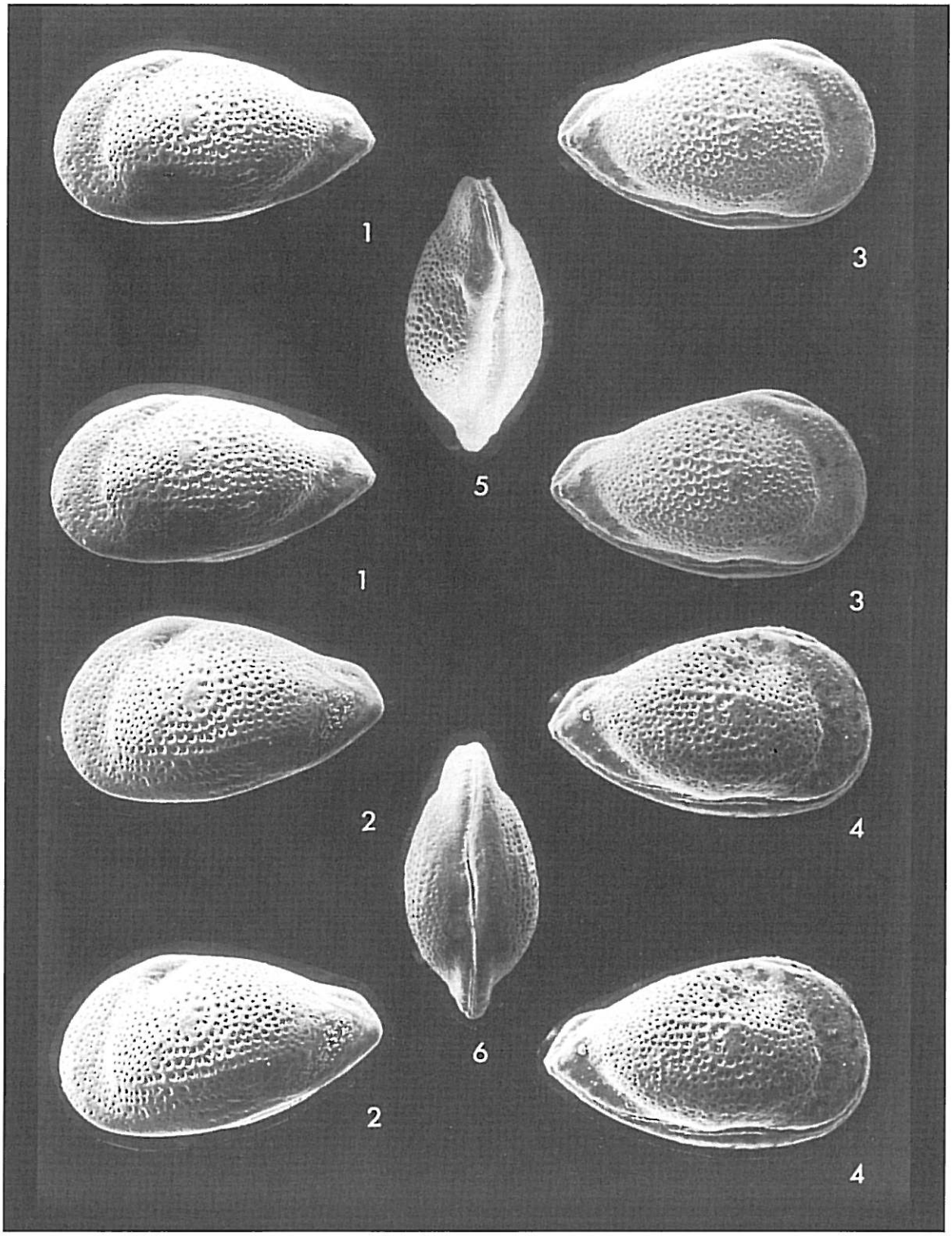


Plate - III

Protobuntonia khasibaensus sp. nov.

All specimens are from the Khasib Formation of South Rumaila Well-104.

Fig. 1. Female carapace, left valve, external, lateral view, (holotype OS 12941); stereoscopic paired photographs; 2408 m; x79.

Fig. 2. Female carapace, left valve, external, lateral view, (paratype J.T. 129); stereoscopic paired photographs; 2406 m; x80.

Fig. 3. Female carapace, right valve, external, lateral view, (paratype J.T. 130); stereoscopic paired photographs; 2412 m, x82.

Fig. 4. Female carapace, right valve, external, lateral view, (paratype J.T. 129); stereoscopic paired photographs; 2406 m; x80.

Fig. 5. Female carapace, external, dorsal view, (paratype J.T. 130); 2412 m; x74.

Fig. 6. Female carapace, external view. (paratype J.T. 130); 2412 m; x74.

ACKNOWLDGEMENTS

I would like to express my sincere thanks to Oil Ministry of Iraq for providing the samples studied in this paper.

REFERENCES

Al-Bashir, J.M.T., 1986. Cretaceous Ostracoda of the superfamily Cytheracea from Iraq, their biostratigraphy and correlation with adjacent regions, *Ph.D_Thesis. University of Glasgow, Scotland*; 587p., 89pl., 19 figs., 7 tables.

Al-Bashir, J.M.T., 1988. Cretaceous and Lower Tertiary Ostracoda from Dhifriya Well-1. *O.E.C., Internal Report*, p.74, pl. 17, fig. 1, table 1, chart 1.

Apostolescu, V., 1961. Contribution a l'etude Paleontologique (Ostracodes) et stratigraphique des Bassins Cretaces et Tertiaires del 'Afrique Occidentale. *Rev. Inst. Franc., Petrole*, **16**, 7-8; 779-786,pl. 1-18.

Baird,W., 1850. The Natural History of the British Entomostraca. *The Royal Soc., London*, 364P

Bismuth, H., Boltenhagen, C., Donze, P., Le Fevre, J. et Saint-Mare, P., 1981. Le Cretace moyen et superieur du djebel Semma (Tunisie du Centre-Nord); microstratigraphie et evolution sedimentoloque. *Bull. Centres Res. Explor. Prod. Elf-Aquitaine*, **5**, 2; 193-267, 11 pl., 9 figs.

Bold, W.A. Van den, 1964. Ostracoden aus der Oberkreide von Abu Rawash Agypten. *Palaeontoraphica*, **123**; 112-136.

Grekoff, N., 1954. Sur l'evolution et repartition quelques generes d'Ostracodes d'Ostracodes dans la serie geologique Post-Paleozoique. *Geol. Soc. Franc. C.R.*,**13**, 333-335.

Grosdidier, E., 1973. Associations d'ostracodes du Cretece d'Iran. *Rev. Inst. Fran. Petrole*, **28**,2,131-169, pl. 1-15.

Grosdidier, E., 1979. Principaux ostracodes marins de l'intervalle Aptien-Turonien du Gabon (Afrique occidentale). *Bull Centres Res. Explor Prod Elf-Aquitaine*, **3**, 1, 1-35, 12 pl., 1 fig., 2 tables.

Howe, H. V. and Chambers, J., 1935. Louisiana Sabine Eocene Ostracoda *Bull Geol. Surv.* La., Baton Rouge, **5**; 1-65.

Latreille, P.A., 1806. Genera Cruatacea et insectorum Koening, Paris, 4 parts in two volumes, 217-583.

Moore, R.C., (Editor). 1961. Treatise on Invertebrate Paleontology pt., Q. The Arthropoda 3. *Geol. Soc. Am. And University of Kansas Press* 422 p., text-figs. 1-334.

Morkhoven, F. P. C. M. van, 1963. *Post Paleozoic Ostracoda*, Amsterdam; Elsevier Publ. Co., Vol **2**, Generic Description; 478 p.

Muller, G. W., 1894. Die Ostracoden des Golfes von Neapel und der angrenzonden Meeresabschnitte. *Staz. Zool.* Napoli, Fauna Flora Neapel. Monographie, **31**, 1-404, 40 pls.

Reyment, R.A. and Elofson, O., 1959. Zur kenntnis der Ostracodengattung *Bunonia. Stockh. Contr. Geol*, **9**, 157-164, 3 pl.

Sars, G. O., 1866. Oversight of Norges marine Ostracoder. *Vidensk, Selsk. Cristiania, Forh.*, Oslo, **7**, 1-130.

Sayyab. A.S., 1956. Cretaceous Ostracoda from Arabian Gulf Area. Ph.D, dissertation, State University of lowa; 138 p; 5 pl.

Sylvester-Bradley, P.C., 1948. The Ostracode genus *Cytheresis. J. Paleontol.*, **22**, 6; 792-797.

Petroleum Res. J. Vol. 15 (2003): P. 65–72, 11 Figs.

FTIR Infra-red Observations of the Adsorption of Ethene, Ethyne and Carbon Monoxide on Supported Platinum Catalysts

Ezziddin A. Arafa*

دراسة إمتزاز الإيثين والإيثاين وأول أكسيد الكربون على حفازات البلاتين المدعم باستخدام الأشعة تحت الحمراء

عز الدين أحمد عرفة

تم في هذه الدراسة استخدام تقنية الأشعة تحت الحمراء في تتبع إمتزاز المواد، الإيثين والإيثاين وأول أكسيد الكربون على حفازات البلاتين المدعم على السيليكا والألومينا والماغنيسيا. على ضوء ذبذبات الأطياف المتحصل عليها من تجارب إمتزاز هذه المواد على الحفازات تحت الدراسة وتلك المنشورة على حفازات عناصر المجموعة الإنتقالية الأخرى، تبين أن إمتزاز الإيثين والإيثاين ينتج المركب إيثايليدين ذو التركيب ($-C-CH_3$) كمركب وسيط على أسطح الحفازات العذراء. بيد أن الحفازات التي تم استهلاكها في هدرجة الإيثاين بينت أطيافاً بها ذبذبات تشير لوجود المركبات الوسيطة ذات التركيب PtCH=CHPt ومركبات هيدروكربونية متبلمرة.

كذلك بينت الدراسة أن أول أكسيد الكربون يمتز في صورة خطية على أسطح الحفازات العذراء ويتغير إلى الصورة الجسرية عندما يتم أكسدة الحفازات بالهواء خصوصاً بالحفازات المدعمة على السيليكا.

Abstract: *The adsorption of ethene, ethyne and carbon monoxide on silica-, γ-alumina and magnesia-supported platinum catalysts was studied by Fourier Transform Infrared Spectroscopy (FTIR). On the basis of the observed band frequencies and the reported literature data, assignments have been made for the bands detected in the spectra. The addition of ethene and ethyne to freshly reduced Europt-1(6.0% Pt/SiO_2) resulted in the formation of an ethylidyne ($C-CH_3$) species as evidenced by the development of bands at 1297 cm^{-1} ($\delta_s(CH_3)$) and 954 cm^{-1} ($\nu(C-C)$) in addition to the $vs(CH_3)$ at 3074 cm^{-1}.*

While on ethyne/hydrogen deactivated catalysts, bands characteristics of surface species such as, PtCH=CHPt (band at 1693 cm^{-1}, $vs(C=C)$) and of hydrocarbon polymeric moieties (bands at 2974-2884 cm^{-1}, $\delta_s(CH_3)$ and 1374 cm^{-1} $vs(CH_3)$), were detected.

On freshly reduced catalysts, carbon monoxide was found to adsorb in the linear form (Pt–C=O, at $\nu_s C-O$ (2086 cm^{-1}, 2112 cm^{-1}, depending on support type). Exposure of the catalysts to air tends to convert the linear form of carbon monoxide to bridged form ($Pt\begin{matrix}\diagup C=O \\ \diagdown C=O\end{matrix}$) at $\nu_s C-O$ (1886 cm^{-1}, observed on silica-supported pt-catalysts).

INTRODUCTION

Although the chemical nature of the adsorbed species at metal surfaces has been the subject of debate for more than six decades, since the pioneering work of Horiuti and Polanyi[1], it can be said with

* present address: The independent (Al-Muhaied) bureau, P. O. Box 81437, Tripoli-Libya. E. mail: muhaied @Yahoo.com

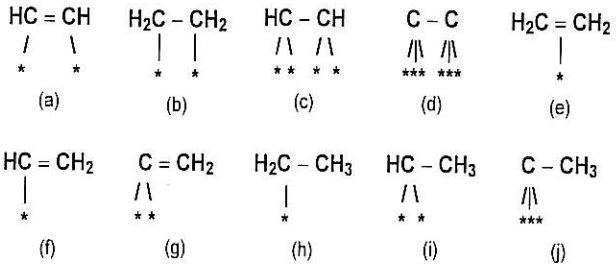


Fig. 1. The adsorption forms of ethane.

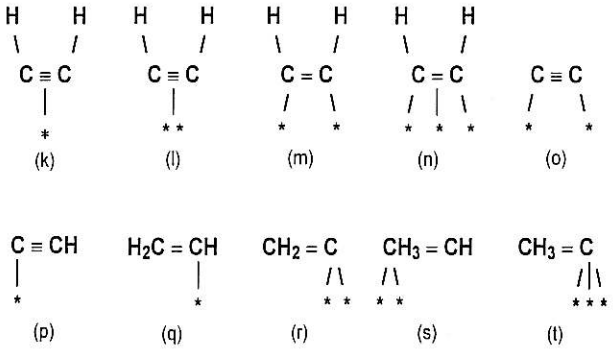


Fig. 2. The adsorption forms of ethyne.

confidence that, so far, these studies have not yet brought about a clear and unambiguous picture of the adsorbed states of even the most simple molecules, such as ethene and ethyne, at these surfaces. Knowledge concerning the adsorbed states of olefins, di-olefins and carbon monoxide has been obtained in part from infrared (I.R.) studies of organometallic chemistry[2] and the application of direct instrumental methods developed by surface physicists[3], such as, AES, LEED, XPS, *etc.*, which have been mainly concentrated on the adsorption of ethene and ethyne on single crystals. However, the application of the results of these methods to inerpret catalytic processes is not straightforward. This is due to the fact that most of these studies are carried out over clean surfaces (generally without hydrogen), under ultra-high vacuum conditions and usually at low temperatures, whereas catalytic reactions take place on surfaces covered with adsorbed species and under several pressures of reactant gases at ambient or elevated temperatures. The other source of information regarding the adsorbed states of unsaturated hydrocarbons and carbon monoxide comes indirectly from the kinetics and product distributions of various processes such as hydrogenation, adsorbed states of unsaturated hydrocarbons and carbon monoxide comes indirectly from the kinetics and product distributions of various processes such as hydrogenation, deuterium exchange and isomerisation of these compounds[4]. Various states of ethene adsorption have been proposed and these are presented in the formulae a-j (Fig.1). The findings of the studies of ethyne adsorption and hydrogenation on metal surfaces led to the postulation of the adsorbed species presented in the structures k-t (Fig.2). The presence of any of these adsorbed species on any particular metal surface is the subject of the literature data reported by many investigators and found to depend on, the metals themselves, their dispersion, oxidation state and the type of the support. A wealth of research has been done in recent years to try to understand the interaction of carbon monoxide with metal surfaces. Primarily this because CO chemisorption is an important step in various industrially important reactions, such as, the methanol synthesis, Fisher-Tropsch process and the formation of alcohols. Secondly, CO has been used widely as a probe for catalyst surface area determination and as a test molecule to distinguish the active centres in the catalytic reactions. The current knowledge of the spectroscopy of adsorbed molecules on catalyst systems originated from the pioneering studies on organometallic compounds[1,5-8]. The C-O stretching frequency of gaseous CO is at 2143 cm^{-1} and this band was observed to shift to between 2000 cm^{-1} and 2100 cm^{-1} after monodentate ligand formation (linear species) and shifts below 2000 cm^{-1} when bi-dentate ligands (bridged species) formed with transition-metal compounds. The so- assigned 'linear' and 'bridged' CO species to adsorb on metal surfaces are depicted in the structures (u-z, Fig. 3).

This paper presents the results of Fourier transform infrared (FTIR) spectroscopy investigation of the nature of adsorbed ethene, ethyne and carbon monoxide on silica- , alumina- and magnesia-supported Pt-catalysts at room temperature (22 ± 2°C) under different conditions and treatments.

EXPERIMENTAL

Apparatus

The apparatus which was employed for *in situ* I.R. experiments consisted of a conventional vacuum system containing a reaction vessel similar to that described previously[9-11] and storage bulbs for the feed stocks of hydrogen, hydrocarbons and carbon monoxide, which maintained at a pressure of ~0.01 Pascal (Pa) by means of a mercury diffusion pump backed with an oil rotary pump. The *in situ* I.R. cell

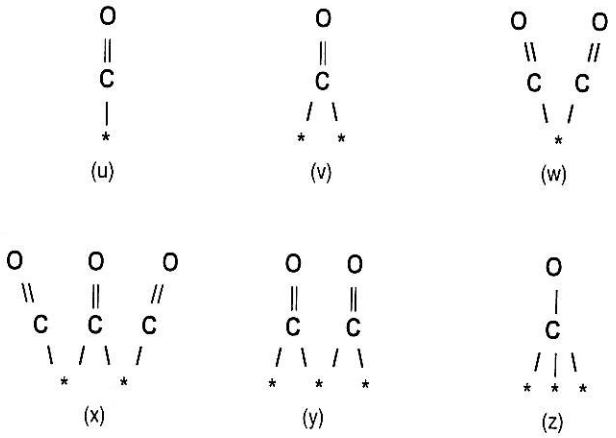


Fig. 3. The adsorption forms of carbon monoxide.

used is shown diagramtically in figure 4. It contained a catalyst wafer specimen holder, a Nichrome-wire furnace surrounding the outer body of the quartz cell which was capable of heating the wafer sample to 800°C. The temperature in the cell was monitored by an electronic thermometer (Electronics Ltd.- 1602 Cr/Al) coupled to a chromel-alumel thermocouple located in a thermowell close to the sample. Two KBr windows (25 x 4 mm x Barns), sealed in stainless steel rings with Araldite adhesive, were fitted to the two ends of the I.R. cell by stainless steel threaded jackets and sleeves surrounded by a water coolant system to prevent thermal shock to the KBr windows. The cell could be pumped to ~0.01 Pa using the vacuum system. The catalyst powders (~ 0.05g) were pressed in to wafer discs in air (~7 tonnes pressure). The wafers were placed in the I.R. cell and about 500-1000 scans were recorded. This was usually followed by I.R. measurements of the sample after brief evacuation (~ 15 minutes), flushing with He (25 ml min^{-1}), or heating to an elevated temperature.

When direct adsorption of ethene, ethyne or carbon monoxide was required, a diffuse reflectance collector (type DRIFT-Spectra-Tech Inc.) was used. The design of the collector employs 4 flat and 2 spherical reflectors, plus an alignment mirror (Fig. 5). The sample cup (13 mm, i.d.) could be removed (for emptying and filling the catalyst) from the top of the collector, by sliding the ellipsoids out of the way. The collector was connected to a vacuum system for evacuation and handling the

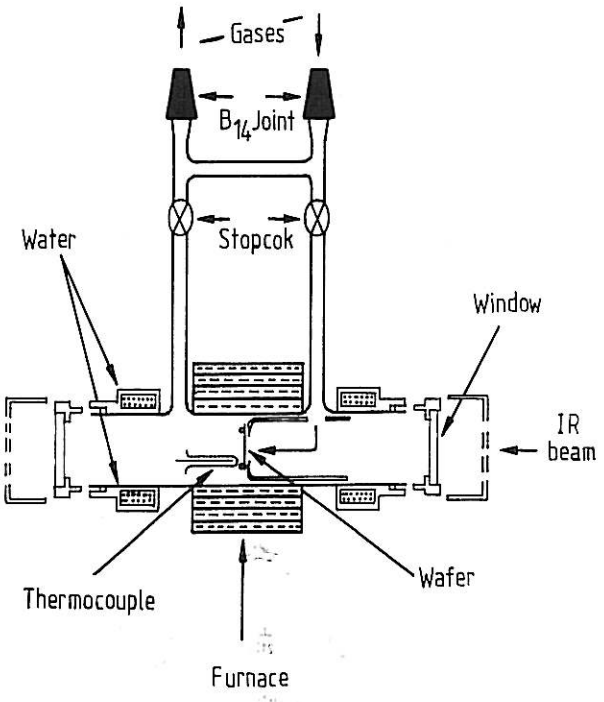


Fig. 4. The *in-situ* I.R. cell.

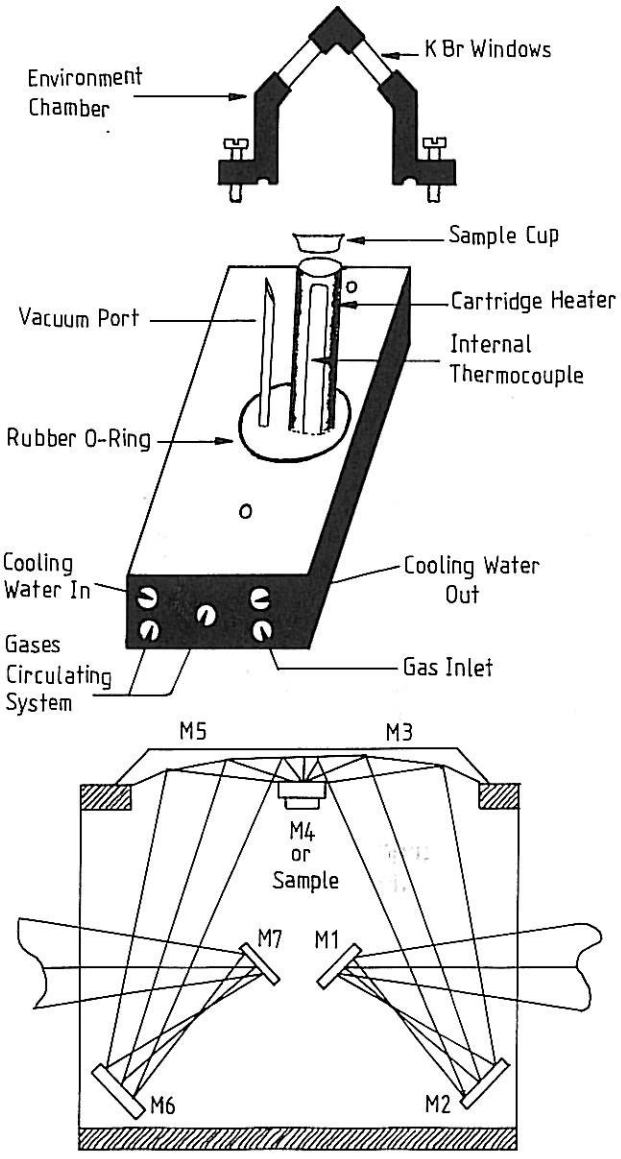


Fig. 5. The diffuse reflectance I. R. cell (DRIFTS).

adsorbate gases. The catalyst samples were heated to the required temperature by an internal cartridge heater.

Catalysts

The catalysts employed in this study are standard reference catalysts, Europt-1, is a 6% (w/w) Pt/SiO_2 catalyst with a total surface area of $185 m^2g^{-1}$ and a pore volume of 0.72 cm^3g^{-1}, prepared by Johnson Matthey Chemicals plc[12]. Europt-3, is a 0.3% (w/w) Pt/Al_2O_3-0.82% Cl catalyst (coded KETJEN-CK 303) with a surface area of 184 m^2g^{-1} and a pore volume of 0.49 cm^3g^{-1}[13]. Another three platinum catalysts supported on silica (Cab-O-Sil), γ-alumina (Degusa, Ltd.) and molybdenum trioxide (Koch-Light, Ltd.) all of 99.9% purity. These catalysts were prepared by impregnation of the aqueous solution of the metal chloride (H_2PtCl_6) containing the required weight of the metal to an aqueous suspension of the support. The excess water was evaporated using a rotary evaporator and the material dried in an air oven at 150°C. These catalysts were characterised as 0.8% (w/w) Pt/SiO_2, 0.8% (w/w) Pt/Al_2O_3 and 0.5% (w/w) Pt/MoO_3 and will be referred to as the impregnated catalysts.

Materials

Hydrogen (H_2) gas (B.O.C., Commercial grade) was used in the catalyst reduction and hydrogenation reactions (deactivation) without further purification. Ethene (C_2H_4) and ethyne (C_2H_2) were degassed at liquid nitrogen temperature (-196 °C) for ~ 15 minutes followed by bulb-to-bulb distillation using liquid nitrogen and methylene chloride + solid CO_2 mixture. Helium (He) and carbon monoxide (CO) (Air products Ltd.) were used as supplied.

Procedures

Two regimes were used for I.R. measurements. In the first, the catalyst samples which had been subjected to C_2H_4, C_2H_2 or CO adsorptions or ((1:3) C_2H_2/H_2) deactivation were examined using a Niolet 5-DXC instrument with the *in situ* cell (Fig. 4) to identify the surface species formed during adsorption or surface interactions and also to examine the effects of various treatments on these species, such as heating or flushing with carrier gases such as He. In the second, direct observation of the adsorption of these molecules by the I.R. system was performed using the diffuse reflectance cell (DRIFTS) (Fig. 5). The procedure used in the 'DRIFTS' experiments was as follows: a background spectrum was acquired using KBr as a diffuse reflector in the Nicolet 5-DXC spectrophotometer at 4 cm^{-1} resolution. A catalyst sample was loaded in the cup of the collector and was reduced in flowing H_2 (30ml min^{-1}) at 250 ± 5 °C for 1h, evacuated briefly (~10 min) at this temperature and then cooled to room temperature (22 ± 2°C). The catalyst was then pulsed with the required adsorbate and after recording the I.R. spectra, the catalyst was subjected to various treatments, such as, evacuation, flushing with He, or heating at elevated temperatures.

RESULTS AND DISCUSSION

I.R. of Adsorbed C_2H_4 and C_2H_2

In the DRIFTS experiments, the spectra following the adsorption of C_2H_4 and C_2H_2 on Europt-1 at room temerature are shown in figure 6. The spectrum of the adsorbed species after subtracting the background and gas phase spectra showed a medium band at *ca.* 1297 cm^{-1} and a weak band at *ca.* 954 cm^{-1} in addition to a weak band at *ca.* 3074 cm^{-1}. These bands, which have also been observed by Beebe *et al.*[14] for C_2H_4 and C_2H_2 on Pd/Al_2O_3 at 1333 cm^{-1} for ($\delta_s(CH_3)$), 1088 cm^{-1} for (ν(C-C)) and 2867 cm^{-1} for $\nu s(CH_3)$, have been assigned to the surface ethylidyne species (structure j, Fig. 1; structure t, Fig. 2).

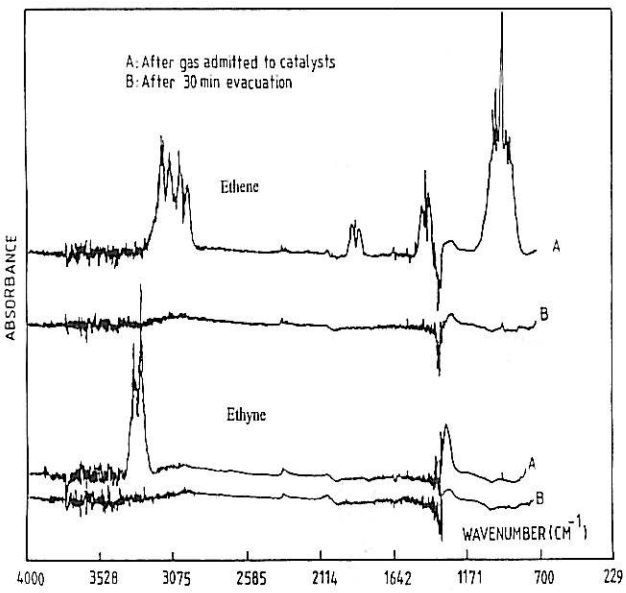


Fig. 6. The I. R. spectra of ethene and ethyne adsorption on Europt-1.

In contrast, when the catalyst samples of Europt-1 and the impregnated 0.8% Pt/SiO_2 had been deactivated by a series of C_2H_2/H_2 and then examined by FTIR, their *in situ* I.R. spectra (Fig. 7) displayed small bands in the region 2974-2884 cm^{-1} and intense bands at 2081cm^{-1}, 1975 cm^{-1}, 1840 cm^{-1}, 1705 cm^{-1}, 1693 cm^{-1} and 1374 cm^{-1}. The bands at 2081 cm^{-1} and 1705 cm^{-1} disappeared as the catalysts were heated to 115°C and flushed with helium for 10 minutes. Based on the literature data [5-8,15-17], the bands at 2974-2884 cm^{-1} and 1374 cm^{-1} were assigned to the CH_3 group and are indicative of the presence of surface alkyl species. While the band at 1693 cm^{-1} has been attributed to C=C stretching and is characteristic of a surface species such as PtCH=CHPt (structure a, Fig. 1; structure m, Fig. 2). The bands at 2081 cm^{-1}, 1975 cm^{-1} and 1840 cm^{-1} are likely to be due to the adsorption of the hydrocarbon molecules on the support material [5].

When ethyne was adsorbed (till saturation) on the various catalysts, gas chromatographic analysis of the gas phase showed that with Europt-1, ethane and ethene were produced. However, with the other catalysts ethene was never observed. From the yields of ethane formed, the average composition of the adsorbed hydrocarbon species at the saturation point was calculated to be $C_2H_{1.6}$ (Europt-1) and $C_2H_{1.8}$ (Europt-3). These observations suggest that a range of adsorbed species is present on these catalysts as a result of an extensive dissociation of the C-H bonds.

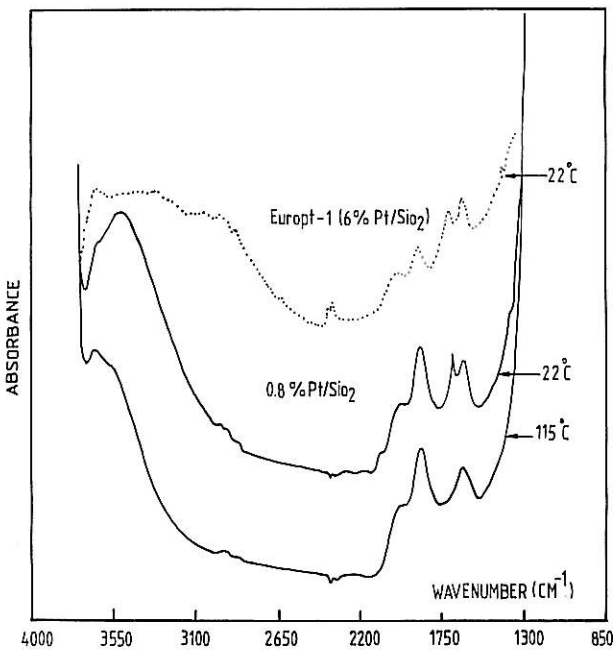


Fig. 7. The I. R. spectra of Pt-catalysts deactivated with C_2H_2/H_2 reactions.

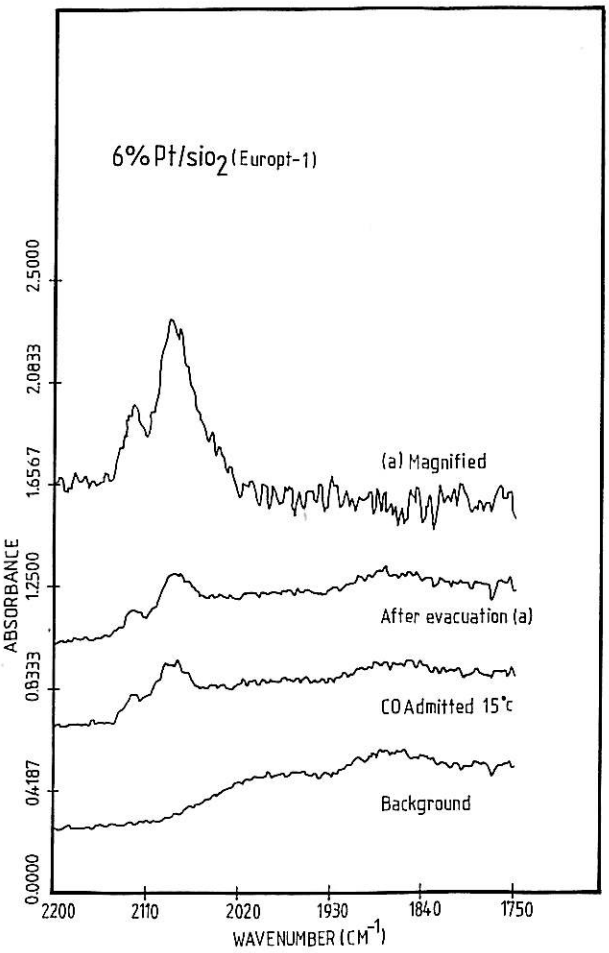


Fig. 8. The I. R. spectra of carbon monoxide adsorbed on Europt-1.

This in turn can lead to two possible processes which may occur independently on the catalyst surface; (i) an extensive dissociation of the adsorbed species to yield multiple bonded species of the form (structures g, i, j, Fig. 1). Figure 6. represents an I.R. evidence for the detection of, ,structure j, following C_2H_4 and C_2H_2 adsorption and hydrogenation on Europt-1 and the impregnated 0.8% Pt/SiO_2 and was reported to exist on Pt (111) surface[16,18]. Consequently, the amount of hydrogen released, together with any hydrogen already present following the reduction process may react with these species to produce C_2H_6 and C_2H_4; (ii) the dissociated species may react with an adsorbed C_2H_4 or C_2H_2 molecule leading to the deposition of polymeric species on the catalyst surface. Such hydrocarbon species have been observed by Avery and Sheppard *et al.*[6,7] on silica-supported Pd- and Pt-catalysts and in this work as shown in the I.R. spectra of adsorbed C_2H_2 on C_2H_2/H_2 deactivated, Europt-1 and the impregnated 0.8% Pt/SiO_2 catalysts (Fig. 7), bands (2974-2884 cm^{-1}, 1374 cm^{-1}).

I.R. of Adsorbed CO

The DRIFTS spectra of the adsorption of CO on the different catalysts are shown in figure 8 ,(Europt-1), figure 9, (0.8% Pt/SiO_2, 0.5% Pt/MoO_3) and figure 10, ((Europt-3) and 0.8% Pt/Al_2O_3). The spectra of adsorbed CO on Europt-1 showed a band at 2086 cm^{-1} and a companion shoulder at 2122 cm^{-1}, while, on the 0.8% Pt/SiO_2 and 0.5% Pt/MoO_3 catalysts, CO adsorption, produced a single sharp band at 2086 cm^{-1}. On Europt-3 and 0.8% Pt/Al_2O_3 catalysts, CO adsorption gave rise to bands at 2124 cm^{-1}, 2086 cm^{-1} and 2070 cm^{-1}. These bands disappeared completely by evacuation of the Europt-3 catalyst, while only thermal treatment (up to 250 ± 5 °C) was required to remove the adsorbed CO from the 0.8% Pt/Al_2O_3 catalyst (except for those species corresponding to the 2124 cm^{-1} band, which shifted towards the lower frequency region at *ca.* 2115 cm^{-1}). Based on the

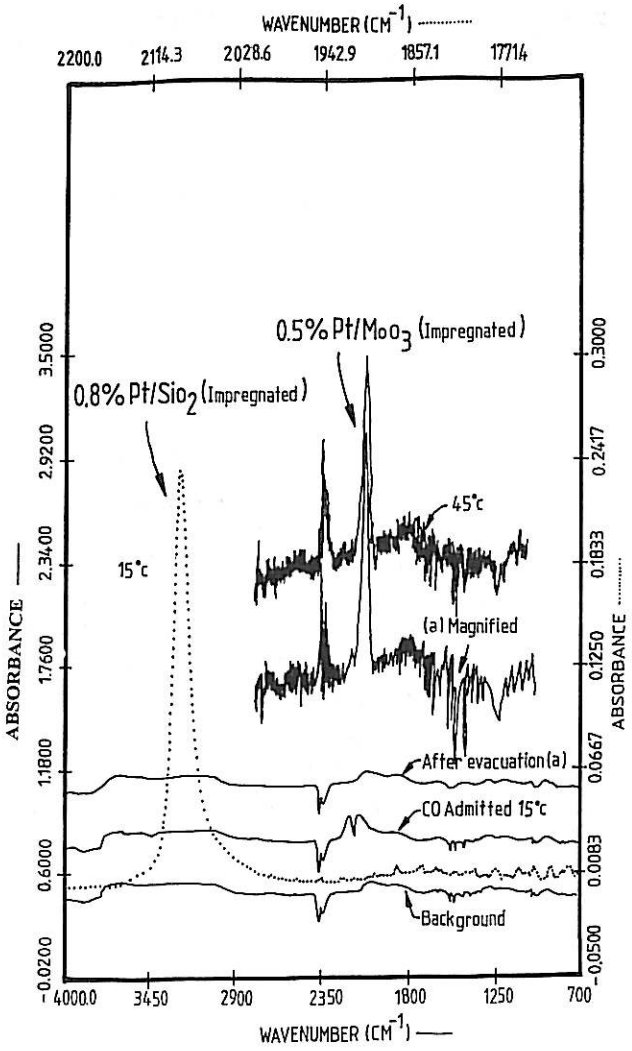


Fig. 9. The I. R. spectra of carbon monoxide adsorbed on Pt-catalysts.

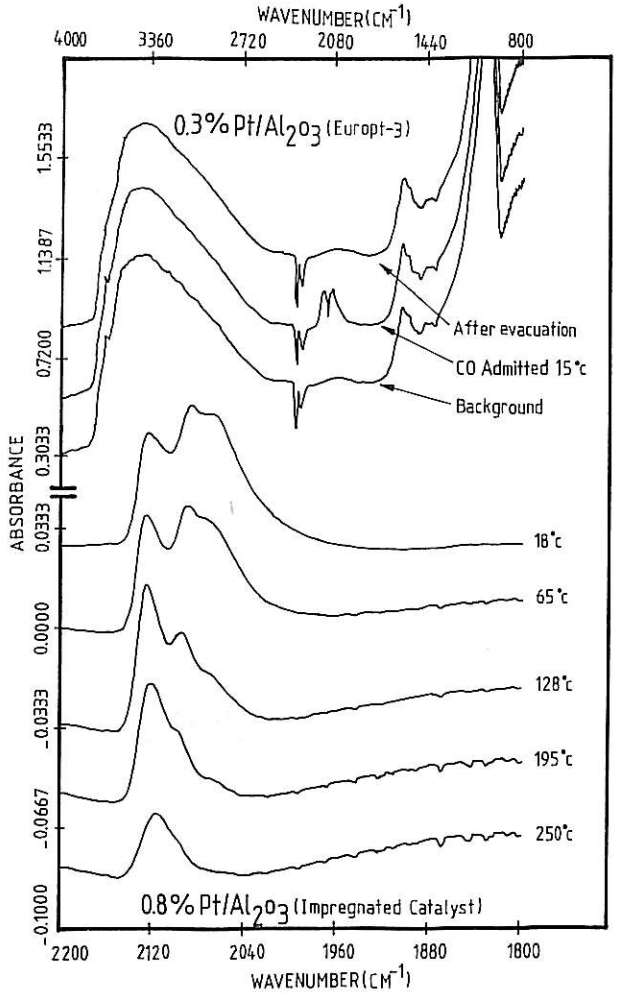


Fig. 10. The I. R. spectra of carbon monoxide adsorbed on Pt-catalysts.

literature data[2,14-20] and the DRIFT -I.R. bands observed on all the catalysts used in this work, the bands at 2086 cm^{-1}, 2122 cm^{-1} and 2124 cm^{-1} are characteristics of the linear form of adsorbed CO (structure u, Fig. 3) and such species have been assigned to adsorp on terrace sites[19].

The catalyst samples of Europt-1, Europt-3 and 0.8% Pt/SiO_2 which were first subjected to CO adsorption (untill it showed a saturation plateau) were subsequently examined by the IR spectroscopy using the *in situ* cell. As it can be seen from the spectra (Fig. 11), these catalysts contained moites which are characteristics of chemisorbed hydrocarbon species as indicated by the bands at 1685 cm^{-1} (C=C), 1632 cm^{-1} (C-C) and 1440 cm^{-1} (CH_3 group). The band at 1685 cm^{-1} appeared as the catalyst (Europt-1) was heated at elevated temperatures followed by evacuation. Interestingly, these species were likely to be evolved by the reaction of CO with the H_2 which may be retained on the catalyst metal and/or on the support after the reduction process.

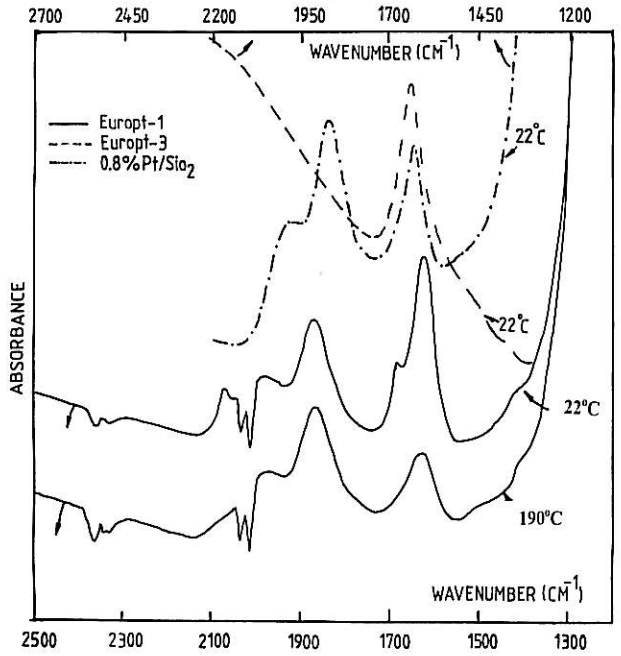


Fig. 11. The I. R. spectra of Pt-catalysts deactivated with CO adsorptions.

A band at 1886 cm^{-1} has also appeared in the spectra of Europt-1 and the impregnated 0.8% Pt/SiO_2 (Fig. 11) which is representative of the adsorbed bridged form of carbon monoxide. This observation is likely to suggest that upon the exposure of these catalysts to air (oxidation), the linearly adsorbed CO detected in the DRIFT-I.R. experiments plausibly converted to the bridged form (structure v, Fig 3). Such bridged species have been detected on oxidized platinum Group metals[19,20].

CONCLUSIONS

In conclusion, an I.R. evidence has been obtained for the formation of an ethylidyne (C-CH_3) species upon the exposure of freshly reduced Europt-1(6.0% Pt/SiO_2) catalyst to ethene or ethyne, while bands characteristics of hydrocarbon polymeric species were detected on ethyne/hydrogen deactivated catalysts. On freshly reduced catalysts, carbon monoxide was found to adsorb in the linear form. Exposure of the catalysts to air tends to convert the linear form of carbon monoxide to bridged form.

ACKNOWLEDGEMENTS

The author wishes to thank his colleagues at Tajoura Research Centre, the staff members of Chemistry Department and Chemical Engineering Department of Al-Fateh University, Tripoli -Libya, for their continuous encouragement and support.

REFERENCES

[1] See, Bond, G. C. and Wells, P. B., 1963. The mechanism of the hydrogenation of unsaturated hydrocarbons on transition metal catalysts. *Adv. Catalysis*, **15**, 91-226.

[2] Sheppard, N. and Nguyen, T. T., 1978. I. R. Spectroscopic studies of CO adsorption on metal catalysts. In: R. J. Clarke and R. E. Hester (eds.). *Advances in Infra-red and Raman Specroscopy*, **4**, 67-210. Wiley, New York.

[3] See, Somorjai, G. A., 1990. Modern concepts in surface science and heterogeneous catalysis. *J. Phys. Chem.*, **94**, 1013-1023.

[4] Webb, G., 1978. Catalytic hydrogenation. In: C.H. Bamford and C. F. H. Tipper (eds.). *Comprehensive Chemical Kinetics*, **30**, 1-253. Elsevier, Amsterdam.

[5] Randhava, S.S. and Rehmat, A., 1970, Infra-red spectra of acetylene on γ-alumina and γ-alumina-supported platinum. *Trans. Faraday Soc.*, **66**, 235-241.

[6] Avery, N. R., 1970. Infra-red of olefins adsorbed on silica supported palladaim. *J. Catal.*, **19**, 15-31.

[7] Prentice, J. D., Lesiunas, A. and Sheppard, N., 1976. Infra-red spectroscopic evidence of π-complex formation from ethylene chemisorbed on palladium and platinum. *J. Chem. Soc. Chem. Comm.*, **1976**, 76-77.

[8] Erkelens, J. and Wosten, W. J., 1978. Infra-red of chemisorbed molecules. *J. Catal.*, **54**, 143-154.

[9] Arafa, E. A., 1989. A ^{14}C-Radiotracer study of the hydrogenation of ethyne on 0.3%Pt/Al_2O_3 (Europt-3). *Petroleum Res. J.*, **10**, 31-37.

[10] Arafa, E. A., 1999. ^{35}S-Radiotracer studies of sulphur poisoning of platinum supported catalysts. *Petroleum Res. J.*, **11**, 51-59.

[11] Arafa, E. A., 2000. The effect of hydrogen, some hydrocarbons, carbon monoxide and sulphur treatments on the structure of platinum supported catalysts. *Petroleum Res. J.*, **12**, 47-56.

[12] Bond, G. C. and Wells, P. B., 1985. Characterization of the standard platinum/silica catalyst (Europt-1). *Appl. Catal.* **18**, 221-259.

[13] Musso, J. C. and Parera, J. M., 1987. Adsorption of Spillover of hydrogen on Al_2O_3 and Pt/Al_2O_3. *Appl. Catal.* **30**, 81-90.

[14] Beebe, T. P., Albert, M. R. and Yates, J. T., 1985. Infra-red spectroscopic observation and characterization of surface ethylidyne on supported palladium on alumina. *J. Catal.*, **96**, 1-11.

[15] Smith, D. L. and Merrill, R. P., 1970. Ethylene adsorption on Pt (111). *J. Chem. Phys.* **52**, 5861-5872.

[16] Ibach, H., Hopster, H. and Sexton, B., 1977. Analysis of surface reactions by spectroscopy of surface vibrations. *Appl. Surf. Sci.*, **1**, 1-24.

[17] Dickinson, J. G., Katz, L. and Ward, R., 1961. Compounds with the hexagonal titanate structure *J. Am. Chem. Soc.*, **83**, 3026-3029.

[18] Kesmodel, L. L., Dubois, L. H. and Somorjai, G. A., 1979. LEED analysis of acethylene and ethylene chmisorption on the Pt(111) surface. *J. Chem. Phys.*, **70**, 2180-2188.

[19] Tanaka, K. and White, J. M., 1983. Infra-red studies of CO adsorption on reduced and oxidized Pt/TiO2. *J. Catal.*, **79**, 81-94.

[20] Fujimoto, K., Kameyama, M. and Kunugi, T., 1980. Hydrogenation of adsorbed carbon monoxide on supported platinum group metals. *J. Catal.*, **61**, 7-14.

Petroleum Res. J. Vol. 15 (2003): P. 73–80, 4 Figs.

Evaluation Study for a Number of Libyan Crude Oils and its Products by Using Chemical Composition (^{13}C n.m.r. Spectroscopy Technique) and Some Physical properties

M.A. Abdulaziz* and Abeer Abdul Kader*

دراسة لتقييم مواصفات عدد من خامات النفط الليبي ومنتجاته كيميائياً باستخدام جهاز الرنين النووي المغناطيسي (^{13}C n.m.r.) وكذلك بعض المواصفات الفيزيائية

محمد علي عبد العزيز و عبير عبد القادر الشيخي

باستخدام كل من جهازي الرنين النووي المغناطيسي (^{13}C n.m.r.) ونقطة الغليان الحقيقية (T.B.P.)، تمت دراسة مجموعة من خامات النفط الليبي (آمنة، السرير، حمادة، الظهرة، الزقوط، سيرتكا، راسكو، البريقة) لمعرفة وتقييم مواصفاتها، حيث تم تقطير كل خام إلى خمسة قطفات عند درجات حرارة وضغوط مختلفة بواسطة جهاز نقطة الغليان الحقيقية (ASTM-D 2892-95) وتم تحديد الخواص الفيزيائية لكل قطفة حسب المواصفات القياسية وباستخدام الجهاز الرنين النووي المغنطيسي تم تحديد، نوعياً وكمياً، نسبة المواد العطرية والبرافينية في كل قطفة. وكذلك تم رياضياً حساب عدة علاقات مهمة وهي النسبة المئوية لتوزيع الكربون لكل من المواد البرافينية المستقيمة ومتوسط طول السلاسل البرافينية المستقيمة في جميع قطفات النفوط التي تم دراستها.

من خلال النتائج تم الحصول على معلومات قيمة تبين مواصفات وطبيعة كل نفط خام ومشتقاته والتي ستساعد في تسويق هذه الخامات ومنتجاتها وكذلك إيجاد بدائل متشابه للخامات المستخدمة في الصناعات النفطية وأيضاً معرفة الظروف التشغيلية للمصافي للحصول على المنتجات المستهدفة بالكميات المطلوبة.

Abstract: *In this investigation a number of Libyan crude oils (Amna, Hamada, Sarier, Aldhara, Zaggut, Sirtica, Rasco, Al Brega) were studied by using ^{13} C n.m.r. and true boiling point instrument to evaluate and characterize each crude oil and its products.*

Each crude oil was distilled for five fractions at different temperatures and pressures by using true boiling point instrument (T.B.P.).

As a consequence, a number of physical properties were determined for each crude oil and its products, according to the ASTM standard method, and by applying ^{13} C n.m.r technique, qualitative and quantitative results were obtained as a percentage of aromatic and aliphatic for each fraction. Then by using a number of mathematical calculations, the straight chain aliphatic, Cn straight chain aliphatic and the average chain length are calculated.

It is clear that this valuable information, obtained in this investigation, can be utilized for crude oil marketing, and the development of similar alternatives of crude for petrochemical industries and refineries processes.

* Ras Lanuf Oil and Gas Processing Co. Inc.

INTRODUCTION

Crude oil is a mixture of a huge number of aromatic hydrocarbons and aliphatic hydrocarbons. This mixture contains hydrocarbon with sulphur, oxygen and nitrogen atoms. A method of classifying crude oils is necessary to provide a guide to the quality, and hence value, of the oil. The specific gravity of the crude oil provides a rough measure of the amount of the lighter fractions present. The lower the specific gravity (or the higher of the API gravity, which is an inverse scale) the greater is the yield of the light fractions by simple distillation and hence the higher the price of the crude oil[1]. The quantitative identification of each compound in crude oils is neither practically feasible nor desirable.

Instead of this an overview of the chemical composition of the crude oil can be obtained as average structural parameters using the existing analytical techniques. High-resolution ^{13}C n.m.r. of liquid solution can make an important contribution for coal and oil derived products[2, 3].

However, in the last thirty years the whole field of chemical analysis has developed a base for extremely rapid analysis. Qualitative and quantitative analysis, to single components in very complex natural products, such as petroleum fractions, which were considered impossible, are nowadays carried out as a matter of routine in plant laboratories. Two main factors account for this change; on one hand, the discovery of new separation techniques, for instance chromatographic methods and in particular gas-liquid chromatography and on the other hand, the development in instrumentation which has made possible the production of fast, reliable and relatively cheap instruments, such as n.m.r., infra-red, uv-visible and mass spectroscopy. But in spite of all the advances, knowledge of the constituents of some petroleum fractions is still very fragmentary, particularly in the region of residual oils and asphalt materials. Further-more, in the case of fractions for which the total analysis is practicable, the very wealth of information possible is difficult to interpret for the purposes of plant design and operation. In such cases use is made of simpler, though still accurate, methods of characterization. One group of such methods uses functions based on a set of physical constants, to describe the factors or indices of the predominant chemical character for the petroleum fraction.

The second group, comprising the methods of structural group analysis, describes the character of the fraction in terms of elements consisting of an imaginary average molecule having the chemical and physical properties of the sum of the individual fraction's component, which is based on their concentration.

Hence, the use of ^{13}C n.m.r. Spectroscopy offers distinct advantages over other methods, as the spectra, which can be recorded in relatively short time, provide detailed compositional characteristics of the crude that are unobtainable by other methods[4].

In this work quantitative and qualitative ^{13}C n.m.r. Technique is applied for a number of Libyan crude oils and their products to study their compositional structure. The TBP was used to distil five fractions for each crude oil. Then a number of physical tests was carried out to correlate them with ^{13}C n.m.r. results. The carbon percentages of (straight chain aliphatic, average chain length, aromatic) were calculated for all crude oil fractions. This paper represents the first step of a research programme in the RASCO laboratory to survey, characterize and evaluate all Libyan crude oil and its products. The obtained results provided plenty of compositional information to be utilised for crude oil characterisation and evaluation. This led to the establishment of analytical technique using n.m.r. Instrument for product quality control tests, crude oil alternative for refineries, petrochemical industry requirements and marketing policy.

EXPERIMENTAL

(1) - True Boiling Point: Three litres of crude oil were distilled in the Fischer autodest 800 (ASTM D-2892) apparatus into five fractions to the eight crude oils as shown in Table 1.

(2) - NMR Spectroscopy: ^{13}C spectra were taken on a Bruker AC/100 MHz super-conducting spectrometer. ^{13}C Fourier transform spectroscopy was performed at 25 MHz. The experimental conditions were: memory capacity used for data

Table 1. True boiling point.

Fraction no.	Temperature range °C (AET)	Pressure
F_1	up to 93	Atmospheric
F_2	93-204	Atmospheric
F_3	204-260	Vacuum pressure of 100 tore
F_4	260-343	Vacuum pressure of 10 tore
F_5	343-400	Vacuum pressure of 2 tore

acquisition 64 k, sweep width 6024 Hz, flip angle 90^0 , pulse width 5.7 μs, delay time 15s , acquisition time 5.4s, broad-band proton gated de-coupling, sampling temperature and the sample diameter was 5mm. The ^{13}C n.m.r. spectrum for each of the five fractions of crude oils was carried out in D-chloroform in the presence of $Cr(acac)_3$ as relaxation agent. The experiments were carried out in the inverse gated mode to eliminate the nuclear Over Hauser enhancement. The spectrum was divided into two parts, the aliphatic (0-70 ppm) and the aromatic regions (110-160 ppm)[5,6].

The calculations were carried out by measuring the integral for both regions and the straight chain aliphatic were assigned according to Grant and Lindeman [11].

Cα-Cβ-Cγ-Cn-Cγ-Cβ-Cα: This formula showing the position of the different carbons in the straight chain aliphatic as assigned in the following Table 2.

Table 2. Straight chain aliphatic carbons assignment.

Type	Chemical shift (ppm)	Assignment
Cα	14.2	a-Carbon in straight chain
Cβ	22.9	b-Carbon in straight chain
Cγ	32.2	g-Carbon in straight chain
Cn	29.7	n-Carbon is further removed carbon in straight chain

(3)- Physical Property Tests: All analyses were carried out according to ASTM standard methods.

RESULTS

Physical Properties

As shown in Table 3, some physical properties of the eight crude oils indicate that, all crude oils studied are classified as paraffin crude oils, having API gravity ranging from 35.48 (Zaggut crude) up to 41.84 (Brega crude), the pour point ranging from -3 ^{0}C (Brega and Hamada crude oils) up to +24 ^{0}C (Sarier crude) and total sulphur contents are generally low.

The API results in Table 3 show that Brega crude oil has the highest value of API (41.84). This indicates that, Brega crude oil should have the highest yield of light and intermediate distillate. But this is not the case by the TBP distillation result as shown in Table 4. The total yield of the light and intermediate products in Brega crude oil for the five fractions is (68.49 %) which is less than Sirtica crude oil (73.92%) which has API gravity of 39.88. The specific gravity valus of 0.8163 and 0.8266 in Brega and Sirtica crude oils respectively also indicate that Brega crude oil should produce higher yield of light and intermediate distillate

Table 3. Physical properties of the different types of crude oil.

Physical properties	Amna	Sarier	Hamada	Aldhara	Zaggut	Sirtica	Rasco	Brega
Sp. Gr.@15.6 ^{0}C	0.8384	0.8417	0.8290	0.8433	0.8474	0.8266	0.8328	0.8163
Density @15 ^{0}C	0.8380	0.8413	0.8286	0.8429	0.8470	0.8262	0.8324	0.8159
API Gravity @15.6^{0}C	37.20	36.61	39.19	36.29	35.48	39.88	38.40	41.84
R.V.P @ 37.8 ^{0}C	0.305	0.388	0.297	0.535	0.411	0.562	0.503	0.469
Pour point (^{0}C)	+ 21	+ 24	3	+ 6	+ 6	3	+ 18	3
Sulphur cont.(wt%)	0.204	0.170	0.080	0.406	0.420	0.399	0.128	0.167
Salt cont. (mg/l)	16.1	14.3	3.5	7.4	8.3	18.2	11	8.3
Viscosity @ 50 ^{0}C (CSt.)	*	*	*	4.74	4.89	2.88	5.11	2.50

Table 4. The yield (wt. %) for the five fractions to the eight crude oils

Crude Name	F_1	F_2	F_3	F_4	F_5	Total
Amna	4.47	16.51	7.59	15.49	10.47	54.53
Sarier	4.89	16.50	7.75	14.13	10.48	53.75
Hamada	6.00	24.30	9.60	16.90	12.90	69.70
Aldahra	6.45	19.00	9.11	16.77	11.13	62.46
Zaggut	6.00	17.80	10.00	16.20	11.50	61.50
Sirtica	9.45	28.55	9.46	18.16	8.30	73.92
Rasco	6.32	18.31	7.97	16.32	10.26	59.18
Brega	8.56	24.30	11.96	15.85	7.82	68.49

in comparison to the seven crude oils, but this is not the case. On the other hand, the pour point in Brega and Sirtica crude oils has the same value (-3 ^{0}C) which indicates that the physical properties do not give a clear view about the nature and chemical compositions of crude oils. Therefore, further information is still needed about the chemical composition for more understanding of the behaviour of crude regarding its physical properties, products yield and specification.

^{13}C n.m.r. Analysis

The ^{13}C n.m.r. analyses were carried out, carbon distributions for the different types of hydrocarbons were calculated, and some qualitative analyses were also carried out for the five fractions of all crude oils studied.

The aromatic, straight chain aliphatic, Cn and average chain length carbons were calculated and the results are shown in figures 1,2,3,4, respectively and Table 5.

Table 5.Integrated and calculated carbon distribution % for the eight crude's fractions to:
(A)- Aromatic Carbon distribution %.
(B)- Aliphatic (straight, branched and cyclo-alkanes) carbon distribution %.
(C)- Straight chain aliphatic carbon distribution %.
(D)- Cn (further remote carbon) for straight chain aliphatic carbon distribution %.
(E)- Average chain length for straight chain aliphatic carbon distribution %.

Fraction number	(A) - Comparison of aromatic carbons % in the fractions for the eight crudes							
	Amna	Sarier	Hamada	Aldahra	Zaggut	Sirtica	Rasco	Brega
1	3.0	2.4	2.8	1.2	1.8	1.73	1.53	2.36
2	8.2	5.57	7.6	8.5	8.8	4.39	4.09	12.9
3	9.69	10.68	15.4	10.8	15.6	7.38	12.59	15.7
4	13.0	11.96	19.2	15.3	16.7	8.29	16.0	16.5
5	13.3	16.27	21.2	18.7	17.4	13.57	17.55	17.13
Fraction number	(B) - Comparison of aliphatic carbons % in the fractions for the eight crudes							
	Amna	Sarier	Hamada	Aldhara	Zaggut	Sirtica	Rasco	Brega
1	97.0	97.6	97.2	98.8	98.2	98.27	98.47	97.64
2	91.2	94.43	92.4	91.5	91.2	95.61	95.91	87.10
3	90.31	89.32	84.6	89.2	84.4	92.62	87.41	84.30
4	87.0	88.04	80.8	84.7	83.3	91.71	84.0	83.5
5	86.7	83.73	78.8	81.3	82.6	86.43	82.45	82.87
Fraction number	(C) - Comparison of straight chain aliphatic carbons % in the fractions for the eight crudes							
	Amna	Sarier	Hamada	Aldhara	Zaggut	Sirtica	Rasco	Brega
1	44.32	26.38	44.8	24.6	21.4	12.19	16.24	24.39
2	48.53	28.06	48.3	21.1	18.2	19.12	23.47	21.91
3	57.5	33.88	49.6	22.1	25.4	25.13	24.99	30.02
4	62.21	42.27	47.1	26.7	29.6	29.78	31.88	30.16
5	70.28	49.34	48	31.5	31.8	32.66	42.66	33.15
Fraction number	(D) - Comparison of Cn carbons % in the fractions for the eight crudes							
	Amna	Sarier	Hamada	Aldhara	Zaggut	Sirtica	Rasco	Brega
1	3	1.80	3.4	0.4	0.4	0.37	2.08	0.44
2	14	4.40	9.9	4.8	3.3	2.71	3.64	3.97
3	19.8	14.34	15.6	8.8	10	7.61	5.55	12.08
4	31.2	23.38	23.7	14.7	16.6	15.93	16.72	17.14
5	45.23	31.88	27.5	20.9	20.7	21.21	28.45	21.78
Fraction number	(E) - Comparison of average chain length carbons % in the fractions for the eight crudes							
	Amna	Sarier	Hamada	Aldhara	Zaggut	Sirtica	Rasco	Brega
1	5.35	4.5	5.5	4.35	4.3	4.53	5.01	4.04
2	7.47	6.65	6.3	7.4	6.5	6.19	6.3	6.38
3	9.12	10.37	8.8	9.8	10	8.59	7.71	10.04
4	12.08	13.44	12.2	13.35	12.87	12.97	11.92	13.89
5	17.44	27.6	14.3	17.5	16.31	16.54	17.74	17.49

From the ^{13}C n.m.r results and correlation with the physical properties results obtained, it is clear that an overview of each crude oil and its products for characterisation and evaluations can be made.

The aromatic carbon percent results (Fig. 1) show that the sum of aromatic content within the five fractions for each crude oil is highest in Brega crude oil (64.59) and lowest in Sirtica crude oil (35.36). The other crude oils studied are ranging in between which, are [Hamada (64), Zaggut (60.3), Aldhara (54.5), Rasco (51.76) and Amna (47.19) and Sarier (46.88). Secondly, the distribution of the aromatic content within the fractions for each crude oil indicates the properties of light and heavy products for every crude oil. For example, the results show, that apart from F_1 in Amna crude oil, which has 3% aromatic carbon and 2.36 % aromatic carbon for F_1 in Brega crude oil, the aromatic carbon % in the remaining fractions is higher in Brega crude oil in comparison to Amna crude oil. Thus, Brege crude oil has higher aromatic content. But the coated results of conradson carbon results[9] are showing that the values are 1.9 wt% and 1.5 wt% for Amna and Brega crude oil respectively. If the aromatic content only is considered, these results are in contradiction with the aromatic carbon %. But the aromatic types and nitrogen content for these crude oils should be considered. Then, the nature for both crude oils and its product quality can be characterised.

In addition, the Cn % value results (Fig. 3) for the five fractions of Amna and Brega crude oils are clearly showing that Amna crude oil fractions have higher value than Brega crude oil. This indicates that Amna crude oil has longer chain length paraffin distribution and higher average chain length (Fig. 4). The straight chain carbon % results (Fig. 2) are showing that Amna crude oil fractions contain higher values in comparison to Brega crude oil fractions.

This clearly demonstrates how its physical properties behavior can characterize each product and yield %, *etc.*

Accordingly, Amna is classified as a paraffin crude oil with a total sulphur content 0.2 wt% and has low yield of light fraction, which is similar to Sarier crude oil. Amna light naphtha has low iso-alkane and cyclo-alkane compared to Sirtica and Brega crude oils.

Therefore, Amna light naphtha has modest octane number, if compared with Sirtica's and Brega's crude oil light naphtha. Hence Amna light naphtha is not a preferred cat-reformer feedstock, but is an excellent feed stock for olefins production. A comparison and evaluation of all eight crude oils and their products are reported in detail [10].

Furthermore, Sirtica crude oil is an intermediate crude oil, having a gravity of 39.88 ^{0}API, total sulphur content of about 0.4 wt. % and pour point of -3 ^{0}C. This crude has the highest value of light and intermediate distillate, which is 73.92% yield, compared to the other seven crude oils. Sirtica crude oil also has the lowest aromatic carbon percent (Fig. 1) in comparison to the other seven crude oils. The highest aromatic carbon percentages were shown by Hamada and Brega crude oils. However, the aromatic carbon percentage distributions within the five fractions for the eight crude oils to characterise their products were shown clearly in (Fig. 1). Sirtica crude oil results in (Fig. 2) for the straight chain

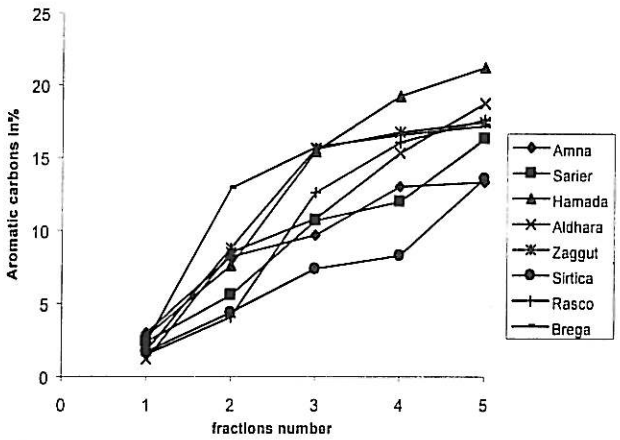


Fig. 1. Comparison of aromatic carbons in the fractions for the eight crude oils.

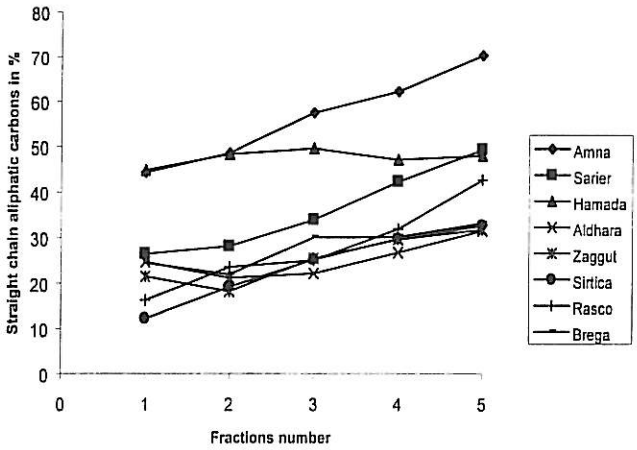


Fig. 2. Comparison of straight chain aliphatic carbons in the fractions for the eight crude oils.

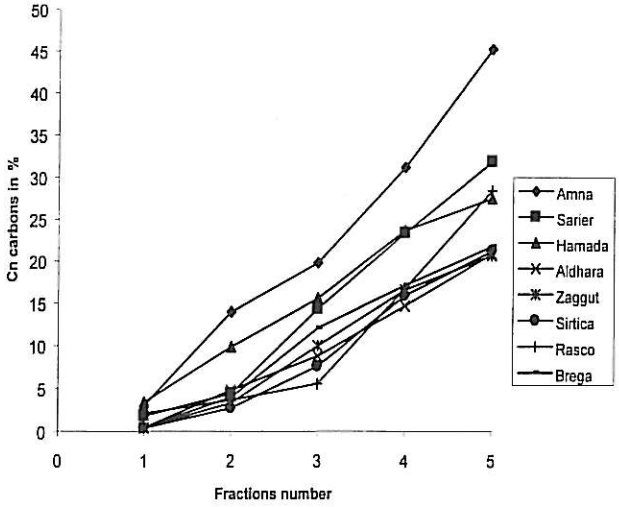


Fig. 3. Comparison of Cn carbons in the fractions for the eight crude oils.

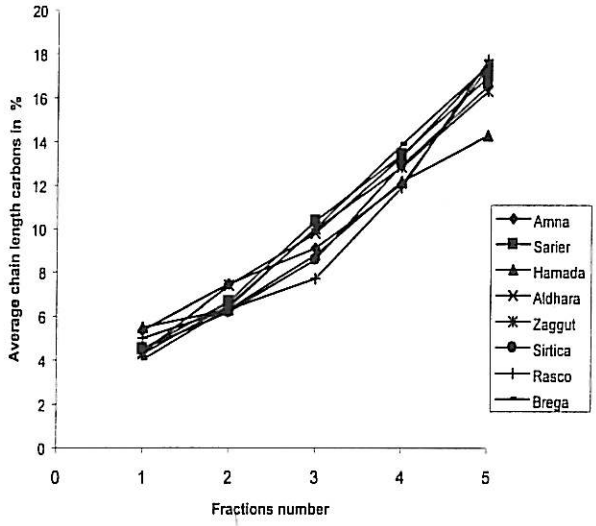


Fig. 4 Comparison of average chain length in the fractions for the eight crude oils.

aliphatic carbon percentages are the lowest for all five fractions in comparison to other crude oils fractions, which makes it high in iso-aliphatic and naphthenic carbons percentages, especially F_2 So, heavy naphtha have a high octane number, which is not good for olefin production, but is an excellent feed stock for aromatic production.

The great content of straight chain aliphatic in the light fraction (F_1 and F_2) in Aldhara and Zaggut (Esidera crude oil) makes it a good alternative for Rasco crude oil to produce the olefins. It also enables the Rasco refinery to produce a wider range of jet kerosene with a suitable freezing point and high quality gas oil to withstand low temperatures. Sulphur content in crude oil and its distribution within the fractions should be considered for the specification. However, Rasco crude oil has less sulphur content (0.167 wt%) than Aldhara and Zaggut (Esidera crude oil) which, consist o.535 and 0.411 wt% respectively.

Finally, all tabulated results and figures obtained from ^{13}C n.m.r. Provide an enormous amount of information to characterize and evaluate all eight crude oils and their products.

CONCLUSION

1- The quantitative ^{13}C n.m.r. for the five fractions of the eight crude oils gives a good view about the carbon distribution of aliphatic and aromatic compounds within each crude oil.
2- The n-paraffin carbon are the highest in Amna, Hamada and Sarier crude oil respectively.
3- Amna crude oil is an unsuitable feed stock for gas oil production. The percentage of n-paraffin carbons indicates that the obtained gas oil will have bad cold properties.
4- Rasco crude oil (Sarrier and Mesla feed for Ras Lanuf oil refinery) can be classified as moderate parafinic oil within the seven studied crude oils.
5- Aldhara and Zaggut (Esidera crude oil) are the best alternative for Rasco crude oil among all crude oil studied.
6- The obtained results in this study indicate that the n.m.r. technique is a good and quick analytical tool for structure characterisation of crude oils. The obtained information can be used to:
   - Predict some important properties of the distilled products.
   - Choose the refining processes and conditions of crude oils.

REFERENCES

[1] Hobson, G.D., *Modern Petroleum Technology*, part 1.

[2] Bartle K.D and Jones, D.W., 1978. *Analytical Methods for Coal and Coal products* Academic Press, New York.

[3] Dreeskamp, H., Potempa, T., and Müller, A., 1989. Aspects of quantitative ^{13}C n.m.r- spectroscopy of high boiling oil residues and coal tar pitches, *Fuel*, **68**, 972-976.

[4] Alhakimi,G., Abeer,A. Abdulaziz, A. and Gebrils, S.,1999. Structure characterization of seven Libyan crude oils by ^{13}C n.m.r., The Sixth Mediterranean Petroleum Conference and Exhibition, November 23-25, 1999, Tripoli -Libya.

[5] Sarowha, S. and Singh, I., 1984. Recent trends in the analysis of petroleum residues by NMR spectroscopy, *Journal of Scientific and Industrial Research*, **43**, 570-575.

[6] Misbah-ML-Hasan, M. Farhat Ali and M. Arab, 1989, Structural characterization of Saudi Arabian extra light and light crudes by ^{1}H and ^{13}C n.m.r. spectroscopy, *Fuel*, **68**, 801-803.

[7] Clutter, D.R., Peterakis,L., Stenger,R.L., and Jensen,R.K.,1972. Nuclear magnetic resonance spectrometry of petroleum fractions carbon-13 and proton n.m.r. characterization in terms of average molecule parameters, *Anal. Chem.*, **44**, No. 8, 1395-1404.

[8] James N. shoolery and William L. Budde, 1976. Natural abundance carbon-13-n.m.r. spectrometry for crude oil and petroleum product analyses. *Anal. Chem.*, **48**, No.11, 1458-1461.

[9] National Oil Corporation (NOC) 1994. *International Marketing, Evaluation of Libyan Crude Oils.*

[10] Abdulaziz,M and Abeer,A.,2000. *Crude Oil Characterisation and Its Products Evaluations by Using ^{13}C n.m.r. Technique and Some Physical Properties*. Technical Report I, Ras Lanuf Gas and Oil Processing Co., Libya.